The Design and Study of Lanthanide-Chelating Macromolecular Diagnostic and Delivery Agents

Joshua M. Bryson

Dissertation submitted to the faculty of the Virginia Polytechnic Institute and State University in partial fulfillment of the requirements for the degree of

Doctor of Philosophy
In
Chemistry

Theresa M. Reineke
Kevin J. Edgar
Timothy E. Long
Louis A. Madsen
Judy S. Riffle
Rick M. Davis

8/7/2009
Blacksburg, VA

Keywords: MRI, Contrast Agent, Luminescence, Drug Delivery

Copyright 2009, Joshua M. Bryson

The Design and Study of Lanthanide-Chelating Macromolecular Diagnostic and Delivery Agents

Joshua M. Bryson

ABSTRACT

Macromolecular magnetic resonance imaging (MRI) contrast agents have unique localization and contrast enhancement properties. We have designed and studied a monodisperse paramagnetic β-cyclodextrin click cluster (**Gd10**) decorated with Gd-containing arms and unique contrast enhancing polymers. To synthesize **Gd10**, a novel alkyne-functionalized diethylenetriaminetetraacetic acid chelate was created and coupled to a per-azido-β-cyclodextrin core and chelated with Gd(III) to yield the precursor macromolecule. Luminescence measurements were carried out using an analogous structure Eu(III)-containing structure and indicated that each lanthanide has an average of 1.8 water exchange sites. **Gd10** yields a high relaxivity profile (6.2 mM^{-1} s^{-1} per Gd^{3+} at 9.4 T). **Gd10** shows toxicity higher than clinically used contrast agents such as Magnevist™ *in vitro* in cardiomyoblast cells. No acute toxicity was observed in the rats (n = 9) and contrast enhanced image analysis indicates renal processes may be involved in clearance.

The contrast enhancing polymers we developed are new macromolecular beacons that allow the delivery of nucleic acids to be visualized at different biological scales. They contain repeated oligoethyleneamines, for binding and compacting nucleic acids into nanoparticles, and Gd(III)/Eu(III) chelates. The chelated lanthanides allow the visualization of the delivery vehicle via microscopy and via magnetic resonance imaging (MRI). We demonstrate that these new delivery beacons effectively bind plasmid DNA

(pDNA) and protect their cargo nucleic acids from nuclease damage. The lanthanide-chelate materials have been found to efficiently deliver pDNA into cultured cells and do not exhibit toxicity. Micrographs of cultured cells exposed to the nanoparticle complexes formed with fluorescein-labeled pDNA and the europium-chelated polymers reveal effective intracellular imaging of the delivery process. MRI of bulk cells exposed to the complexes formulated with pDNA and the gadolinium-chelated structures show bright image contrast, allowing visualization of effective intracellular delivery on the tissue-scale. Because of their versatility as imaging probes, these delivery beacons posses remarkable potential for tracking and understanding nucleic acid transfer *in vitro* and have promise for *in vivo* imaging applications. In later studies the Ln-chelating polymers were co-polymerized with dimethylgalacterate which definitively increases luciferase gene expression (up 50x enhancement) and cellular uptake (up to 2x enhancement).

ACKNOWLEDGEMENTS

First, I would like to thanks my advisor, Prof. Theresa Reineke, for her guidance and invaluable advice throughout my graduate career. She has pushed me through some extremely stressful and unhappy points in my scientific career and helped me to mature into a competent scientist. Thank you, Dr. Reineke, for pushing me to be my very best, for your guidance over these past 5 years, and for giving me excellent presentation and travel opportunities. My committee members both here at Virginia Tech and at The University of Cincinnati also deserve acknowledgement for their advice and constructive criticism, which has certainly helped me to grow as a scientist. Thanks to Dr. Timothy Long, Dr. Kevin Edgar, Dr. Judy Riffle, Dr. Lou Madsen, Dr. James Mack, and Dr. Pat Limbach, for serving as committee members. Also, thank you Dr. Rick Davis for filling in for my Ph.D. defense. Thanks to the great collaborators I have developed relationships with, whose expertise and contribution have made my research higher impact: Dr. Wen-Jang Chu, Dr. Jing-Huei Lee, Dr. Jing Li, and again, Dr. Lou Madsen. A sincere thank you is also warranted for all of the staff members at both Cincinnati and Virginia Tech that have made my life easier, especially Melba Edwards, Tammy Jo Hiner, Mary Jane, John Zurick, John Baker, Cassandra Mcgee, Tom Bell, and Betty. I would like to express great thanks to Techulon Inc. and Chevron-Phillips for funding portions of my conference travel.

I would like to acknowledge coworkers who have had a special impact on my life in graduate school. First, I would like to thank Dr. Chris Gulgas who took me under his wing when I was a young graduate student and helped me learn the ropes of synthetic chemistry. He was an excellent mentor and continues to be in his current professor position. Another important colleague who always brightened my day and showed me how to be a good scientist is Dr. Yemin Liu. Next, thank you to senior students who gave excellent advice and provided great

friendships: Chen-Chang Lee, Lisa Prevette, Sathya Srinivasachari, Vijay Taori, and Yumin Chen. A very special appreciation is warranted to biochemists who have helped me tell the whole story in my research. Thanks to Katye Fichter and Patrick (Big Perm) McLendon for all of your excellent academic contributions and pioneering work in lanthanide microscopy. A special shout out is needed for the people continuing the lanthanide project. Good work Anton and Sneha, chelate chemistry is difficult and frustrating, so hang in there! I would also like to thank the younger students who have provided good friendship and interesting discussion. Thanks to Karina, Gio, Lian, Hao, and Dan. Keep up the good work of our group. You all show great promise! Also a special thanks to all of the people from Dr. Long's group that made our arrival here at VT happier and more comfortable. Thanks to Sean Ramirez, Becca Brown, Matt Cashion, Emily Anderson, Andy Duncan, Matt Hunley, Steve June, Mana Tamami, and especially to my friend John Layman.

My family has been tremendously supportive over these last five years and they will always have my gratitude. Thanks Mom and Dad. I couldn't imagine having better parents or better friends than you. You have always been there to support me and for that I can't thank you enough. Also, great thanks to my brother Zach for your dear friendship and you advocacy. Niki and George Keyser, my mother and father in law, have been great supporters of me, which is support I will never forget. Jon Keyser, my inherited brother, has been of great support to me as he faces his own "teeth cutting" in graduate school, and I hope to be there for him over the next four years of his doctorate.

Finally, and most importantly, I wish to thank my dear wife Rebecca. She has been as involved in this whole process and felt it the entire way. She has supported me through the

stressful and depressing times of the graduate school experience and been my biggest cheerleader for the success I have found. I could not have asked for a better partner for this endeavor, or for that matter, life in general.

Table of Contents

List of Figures

List of Tables

List of Schemes

Chapter 1: Introduction

1.1 Dissertation Overview

Macromolecules are constantly changing the face of modern medicine due to their controllable architectures, prolonged blood-circulation times, unique tissue distribution, higher tissue retention, and selective uptake into tumors via the enhanced permeability and retention (EPR) effect. Because of these unique properties, macromolecular architectures are well suited towards several important diagnostic and therapeutic applications such as: small molecule delivery, protein and nucleic acid delivery, medical imaging agents (carrying lanthanide metals in high density), and for combinations of these applications. This dissertation hopes to demonstrate to the reader how two series of macromolecules are reshaping medical imaging and monitored drug delivery. An extensive background review of relevant literature is carried out in chapter 2.

Heptakis{6-*N*-[(Gd(III)-diethylenetriamine-tetraaceticacid)butyl]-6-(1,2,3-triazole)} cyclomaltoheptaose (**Gd10**) is a molecule designed to feature a β-cyclodextrin core coupled with seven Gd-chelating arms. Albeit with less than desirable yields (~7%), the 13 step synthesis arrives at an easily functionalized, highly effective MRI contrast agent. Chapter 3 of this dissertation will cover the synthesis, characterization, and preliminary MRI studies of this agent. We have thoroughly studied this system *in vitro* in human cardiomyoblast cells and *in vivo* in Sprague-Dawley rats. This agent displays very nice contrast and washout profiles. These studies are discussed in chapter 4 of this dissertation. Finally, **Gd10** has been studied to observe its behavior when conjugated to hydrophobic tails via its hydrophobic cup, which is discussed in chapter 5.

Other systems developed and studied in this dissertation are the Ln-containing oligoamine copolymers. The first generation of these polymers can complex with pDNA and form nanoparticles with positive surface potentials. These polymers show low toxicity and deliver pDNA into cells with high effectiveness. Because they can chelate and carry lanthanides, the polymers offer access to several imaging modalities such as MRI, florescence microscopy, and possible radio labeling. We have demonstrated that these polymers show promising diagnostic potential due to these imaging capabilities, which is discussed in chapter six. The first generation polymers suffer from low transgene expression, so to address this problem we designed a second generation that maintain the same parent structure of the first generation, but incorporate carbohydrates which have been shown previously in our group to promote better transgene expression. The second generation and their biological studies are presented in chapter 7. Finally, the 8th chapter summarizes the body of work encompassed in this dissertation, and chapter 9 discusses future potential work in these systems. Relevant NMR spectra and copyright permissions are included in appendices A and B.

Chapter 2: Lanthanide-Containing Macromolecules as Diagnostic and Delivery Agents

2.1 Macromolecular Contrast Agents

Nuclear magnetic resonance imaging (MRI) is a high resolution non-invasive tomographic imaging technique that relies on the fundamentals of magnetic resonance. Being the most reliable way to obtain soft tissue imaging at sub-millimeter resolution,[1] more than 60 million diagnostic MRI scans are carried out every year. Since MRI does not rely on ionizing radiation, but provides high quality soft tissue images, it a very important tool to both the scientific and medical communities. Indeed, several Nobel prizes,[2] of various disciplines, have been awarded that address both MRI fundamentals and their application towards imaging. The prize was first given to Block and Purcell in 1952, then in 1991 to Ernst, later in 2002 to Wüthrich, and finally to Lauterbur and Mansfield in 2003.

Magnetic resonance imaging relies on probing nuclear spins in the body, specifically hydrogen nuclei spins from water molecules. Signal intensity in MRI is a function of local values of both longitudinal relaxation rates ($R_1 = 1/T_1$) and transverse relaxation rates ($R_2 = 1/T_2$).[3,4] The work in this dissertation largely focuses on T_1 relaxation and how to increase signal intensity by shortening this rate. In lipophilic tissues T_1 relaxation times are quite short and, for this reason, the magnitude of the signal in these tissues is much greater than the signal from hydrophilic tissues and vasculature. Because it is desirable to obtain high resolution images of

hydrophilic tissue and fine vasculature, it is often necessary to administer an agent that may shorten the relaxation times in these regions. One way to shorten relaxation times is to put the water protons in the presence of paramagnetic substances. Paramagnetic compounds act as small magnets by emitting radiofrequencies similar to the tumbling rate of their environment. If this tumbling rate is similar to the Larmor frequencies of proximal water protons, they will absorb these emitted photons and quickly relax to Boltzmann population equilibrium, therefore decreasing their bulk longitudinal relaxation times.

Unlike radiotracer imaging where brightness is dictated by concentration of radio nuclei, MRI relies on water proton relaxation, which is catalyzed by a contrast agent that is present in small concentrations relative to the protons it is influencing.[3] There are several parameters that dictate contrast agent effectiveness in enhancing the relaxivity of bulk water, such as rotational motion (τ_r), proton distance from the paramagnetic ion (r), time of proton localization in the proximity of the paramagnetic ion (τ_m), electron relaxation time in the paramagnetic ion (τ_e), and the number of water molecules directly bound to paramagnetic center (q). Highly paramagnetic metals like Mn(II) and Gd(III), which are ideal as contrast agents, are typically toxic, which requires they be tightly chelated in a thermodynamically and kinetically stable chelate. Adding a chelate around the ionic center complicates the relationships between the parameters that dictate contrast agent efficiency by creating an "inner sphere" water space, which consists of directly bound water molecules, and an "outer sphere" which consists of molecules in close spatial proximity to the chelate, but not directly bound (Figure 2 - 1). The parameters described above and how they relate to relaxation enhancement are well modeled for Gd(III) chelates by equations developed by Solomon, Bloembergen, and Morgan.[5]

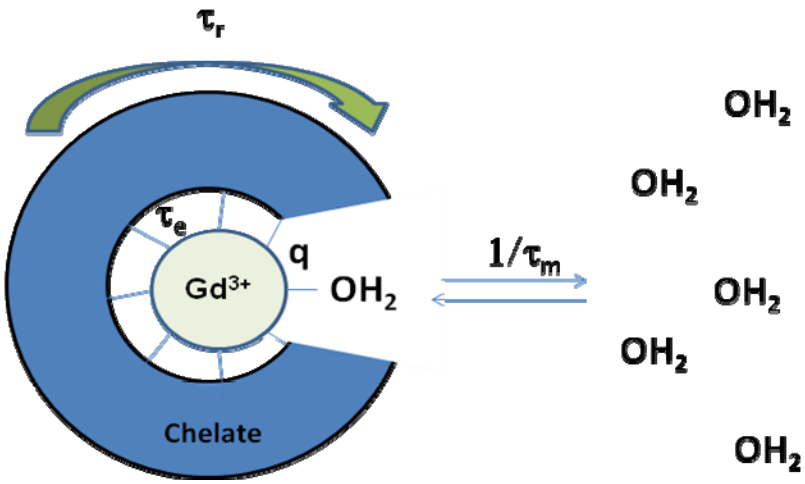

Figure 2-1. Schematic model showing different contrast agent parameters that apply to relaxivity. The dark blue "cage" surrounding the Gd(III) center represents the chelate. The two parameters commonly altered to improve contrast agents are tumbling motion of the complex, which is represented by τ_r, and water coordination residence lifetime, which is represented with τ_m.

Several common and clinically used Gd-chelating agents are shown below. When considering the design of a molecule that will chelate Gd(III), several of the parameters mentioned above are controllable and some are not. The parameters that are dictated by Gd(III) and therefore are not controllable are τ_e and to a lesser degree r, which is simply the preferred Gd-OH_2 bond length. Parameters that can be controlled to some degree are rotational motion (τ_r), which should be as close to the Larmor frequency as possible for the radiofrequencies they emit to cause Boltzmann equilibria. The parameter q should be as high as possible without compromising chelate stability and τ_m, the residence lifetime of the water molecule in the inner sphere, also should match the Larmor frequency and depends on the coordination environment around the Gd(III) ion.[5] Small molecule contrast agents have rotational times on the order of picoseconds, which is quite fast compared to clinically relevant Larmor frequencies. Clinically used small molecule contrast agents also suffer from long water residence times, except for some novel chelates developed by the Raymond group, which are well covered in a recent review.[6]

One way to easily improve contrast agent efficiancy is to increase τ_r so its rotational frequency rate become closer to clinical Larmor frequencies. This can be accomplished by integrating Gd-chelates into macromolecular systems.

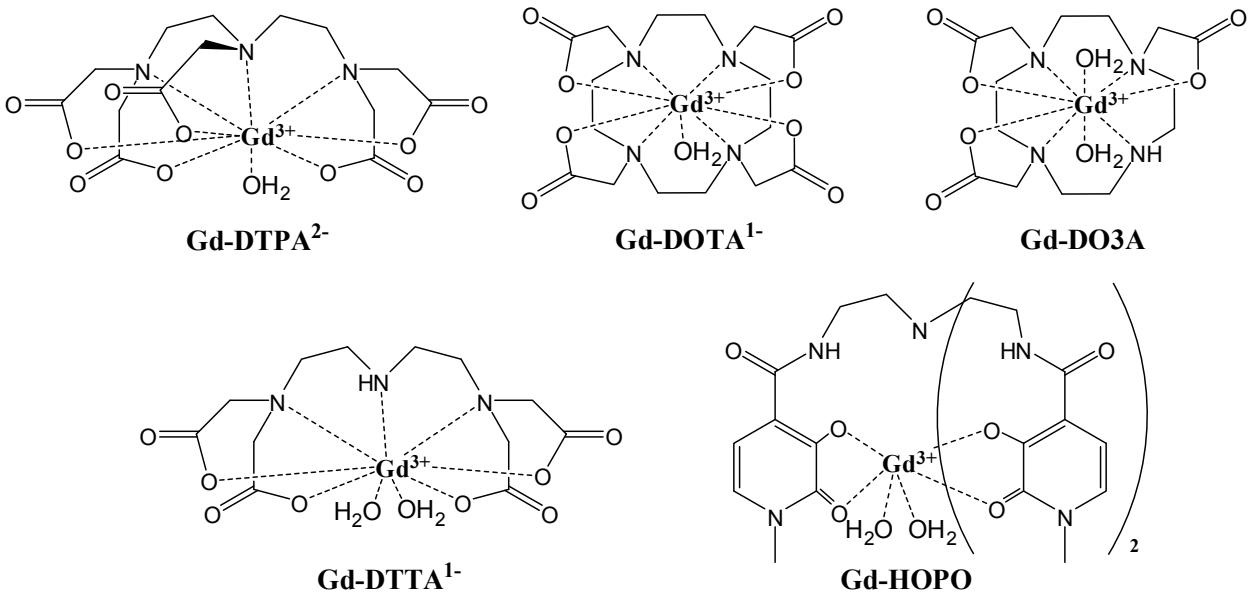

Figure 2-2. Shown are some common chelating agents. Gd-DTPA and Gd-DOTA are the only clinically approved agents currently approved for use in humans.

2.1.1 Polymer Based Systems

The first application of macromolecules towards contrast agents was work carried out by Sieving *et al.* in 1990,[7] by coupling typical Gd(III) – chelates such as DTPA and DOTA (Figure 2-2) covalently to various poly-L-lysines (PLL, Figure 2-3), which then could be coupled to blood pool proteins such as serum albumin. When measured at 10 MHz, the PLL conjugates showed 2 - 3 fold improvement over monomeric analogs like Gd-DTPA and Gd-DOTA. Concurrently, Spanoghe *et al.* functionalized poly-L-lysine chains from a wide array of molecular weights (3,300 – 105,000 Da) and studied the relaxation enhancement as a function of molecular weight.[8] They also found relaxation (2.4 T) enhancement upon conjugation, however no relationship between relaxivity enhancement and molecular weight was observed. This

observation indicates that only limited gains in rotation correlation times were obtained upon conjugation. These gains are largely limited by the free internal motions occurring in the bonds between the chelate and the polymer backbone. Another intrinsic issue with this system is the inability to make a homogeneous agent. Though the degree of chelating agent added can be controlled, labeling of the PLL backbone is not regio-controlled and therefore leads to non-homogenous materials, likely limiting their clinical applicability. Despite these drawbacks, researchers are still pursuing PLL and other homopolymer peptides such as poly-l-glutamic acids,[9] as MRI contrast agent scaffolds. More recent work using poly-lysine polymers coupled with contrast agents, has resulted in the creation of some very elegant systems such as: biodegradable polymeric agents,[10] bimodal imaging agents,[11] and pH-responsive MRI probes.[12]

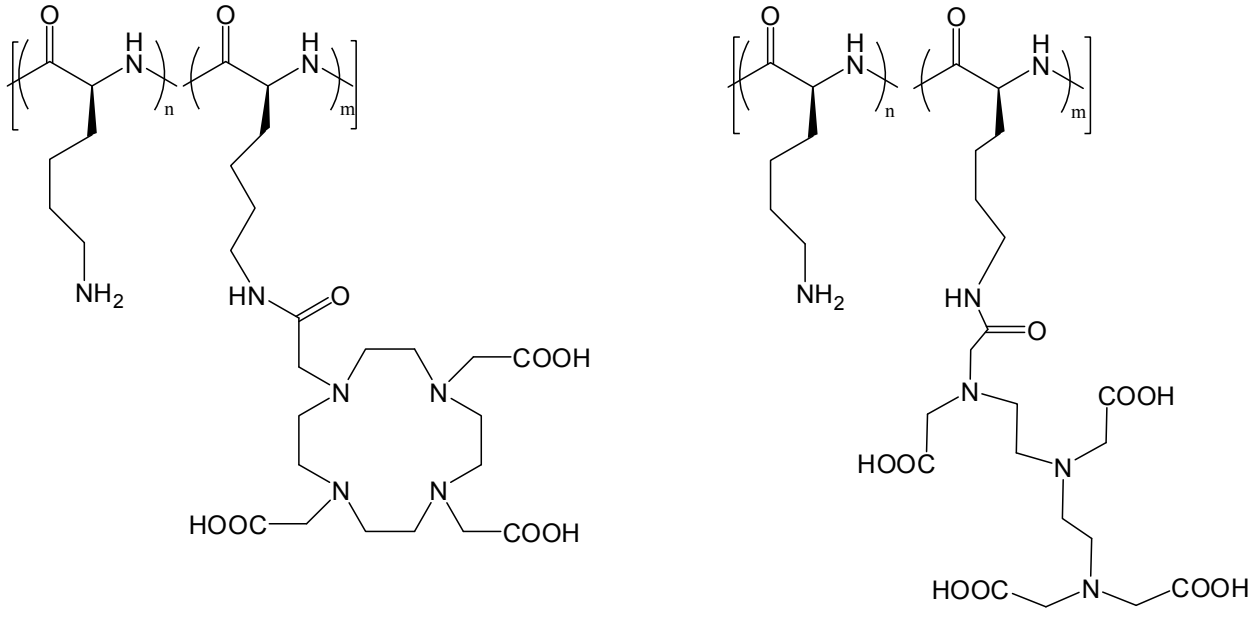

Figure 2-3. Shown are the structures of PLL/PLL-DOTA and PLL/PLL-DOTA random copolymers.

In line with PLL modification with Gd(III) chelates, conjugation to polysaccharides was also part of the early work towards polymeric contrast agents. Armitage *et al.* modified dextrans of

varying molecular weights (9,400 – 487,000 Da) with DTPA type ligands with high conjugation (40 – 50 %) as shown in Figure 2-4.[13] They arrived at similar conclusions to those observed in the PLL conjugation work. Gd-DTPA conjugated dextran polymers showed modest gains (a factor of 1.5 – 2.3) compared to monomeric Gd-DTPA, however, relaxivity decreased as a function of MW increase. Although the authors offer no explanation for this effect, it is likely due to close Gd-Gd distances or perhaps rotation of the DTPA-polymer conjugate is slowed below that of the Larmor frequency with which they were using (100 MHz). This problem was studied with more meticulous polymer and substitution characterization by Rebizak *et al.* in 1998.[14] They found that at lower fields (10 – 20 MHz) relaxivity in these systems would increase as the substitution degree increased, but only to a point, which likely indicates Gd-Gd distances were playing a limiting role.[15] This also confirmed that the rotation rate of this polymer-DTPA complex was slower than 100 MHz. Dextran-DTPA and Dextrin-DOTA conjugates were evaluated in rabbits by Siauve *et al.* and found to be non-toxic and to have good properties as blood pool imaging agents.[16] Other *in vivo* work indicates similar observations for other types of modified polysaccharides.[17] Relaxivity gains shown by dextran conjugation warrant further research, but unfortunately these conjugates suffer from similar drawbacks to the PLL conjugates.

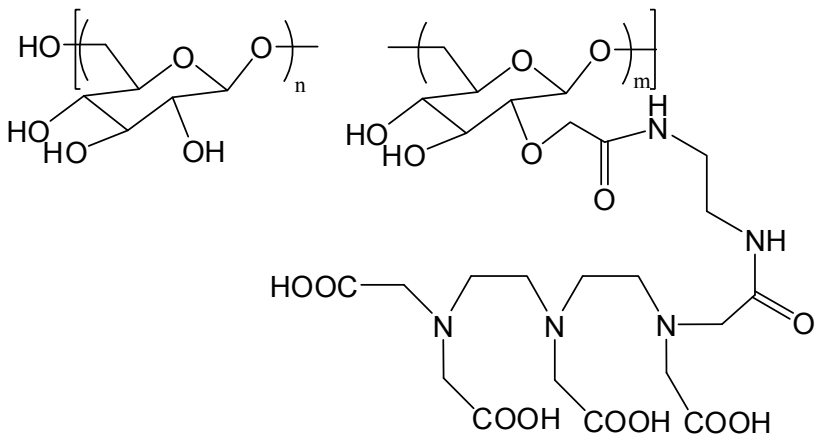

Figure 2-4. Dextran polymer randomly functionalized with DTPAsynthesized by Rebizek et al.

Another logical choice for Gd(III)-chelate conjugation is polyethylene glycol (PEG) due to its hydrophilicity, biocompatibility, and anti-aggregation properties. Researchers have accomplished this using PEG in the backbone in DTPA-PEG copolymers,[18,19] as shown in Figure 2-5, and by having PEG branch away from the parent chain.[20] Ladd et al. found that relaxivity could be increased as a function of molecular weight, however these systems show lower relaxivity than PLL and dextran systems of similar molecular weights. This can be attributed to the more flexible, and hence, more floppy backbone associated with PEG. This work also draws correlations between monomer selection, viscosity by polymer shape, chelator stability, and how they relate to relaxivity. This polymer series showed excellent biocompatibility and increased blood pool/tumor retention times when the MW > 20,000 Da. Work by Ye and coworkers[21] demonstrated that PEG-DTPA copolymers make suitable hepatic targeting agents, because of the renal bypass due to the larger size of these copolymers. Because the chelate in these polymers is copolymerized into the backbone, these materials are easier to characterize than post-modified systems (PLL and dextran).

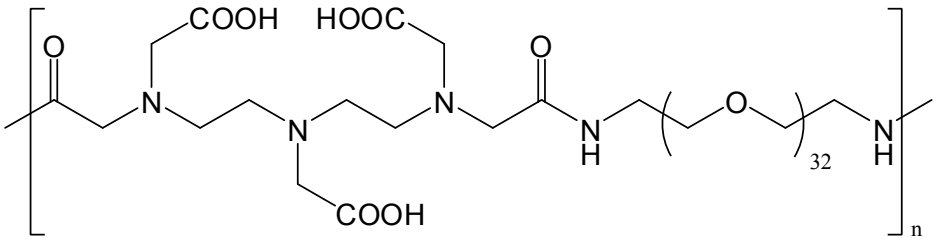

Figure 2-5. PEG-DTPA copolymers created by Ladd and coworkers, shown without the chelated Gd(III) for clarity.

Several other promising DTPA-bis-amide copolymers have been developed (Figure 2-6). The first polymers of this class were developed by Wei and coworkers and consist of DTPA bis amides spaced by various numbers of methylene units (n = 4, 5, 10, 12) aliphatic alkyl chains.[22] The hydrophobic comonomer in this series of polymers led to some interesting conclusions. First, as the length of the hydrophobic block increased, the relaxivity increased and, for higher number of methylene-containing commoners, very high relaxivities were observed, which the authors attribute to amphiphilic self-assembly between the hydrophilic and hydrophobic portions of these polymers. Duarte *et al.* extended the work by using more rigid linkages and found that increasing the rigidity in the hydrophobic comonomer improved overall relaxivity due to the decrease in internal polymer movements.[23] To further develop DTPA step growth polymers, the Lu group at The University of Utah has developed blood pool imaging polymers that can be degraded and cleared via degradation of their disulfide bonds.[8,24] Other interesting work carried out by Benjamin *et al.* involves copolymerization of DTPA with amine functionalized monosaccharides, where he showed polymers showed no enhancement compared with small molecule repeat unit models, at 400 MHz.[25]

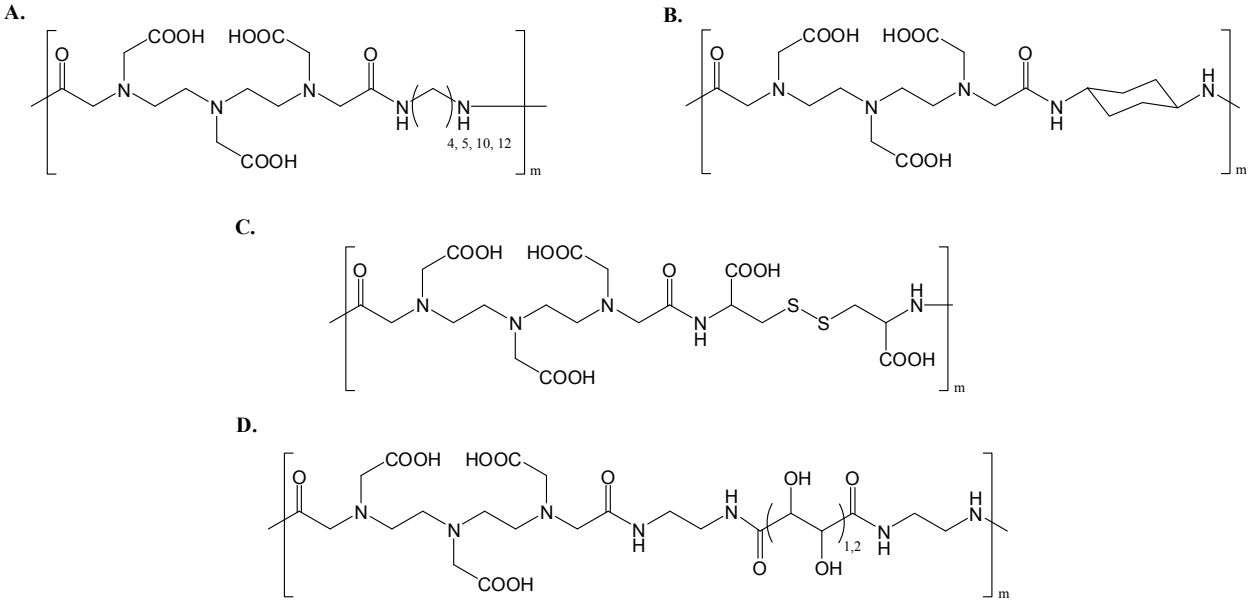

Figure 2-6. Shown are structures of step growth DTPA-bis-amide polymers developed by various groups. A) Wei and corkers, B) Duarte et al., C) Mohs et al. D) Benjamin et al.

Work has also been devoted to developing macromolecular T_1 contrast agent systems based on chain growth type polymerizations. One of the more elegant examples of this is demonstrated in a paper published by Kiessling and coworkers,[26] in which they coupled hydroxypyridonate (HOPO) – based Gd(III) chelates to bicyclic alkenes and polymerized them via ring opening metathesis polymerization (ROMP) as shown in Figure 2-7. They chose ROMP due to the high functional group tolerance and controllability associated with this type of polymerization. They were able to obtain modest relaxivity enhancement compared to the free chelate, however the degree of polymerization was severely limited (DP = 8 - 30) by steric issues between the ROMP catalyst and the chelate monomer. Other groups have developed MRI contrast agent polymers based on free radical polymerization strategies. Semmler and coworkers functionalized DTPA-type ligands with acrylamide type monomers and polymerized with various comonomers using AIBN as an intiator.[27] This work showed a pronounced correlation

between molecular weight up to 45 kDa and relaxivity (60 MHz). These polymers were non-toxic, however long term tissue retention was observed in rats, which can lead to chronic toxicity, *in vitro*. Despite the problems associated with tissue retention, these polymers gave very high resolution images of fine vasculature. The Sherry group has also done some very interesting work with radical polymerized contrast agents.[28] The polymers they developed are designed to allow contrast via a Paramagnetic Chemical Exchange Saturation Transfer (ParaCEST) type mechanism. This is accomplished by polymerizing methacrylate – DOTA - type chelates and probing their ability to suppress bulk water signal. These agents show great potential as the first polymer systems to exploit the ParaCEST platform.

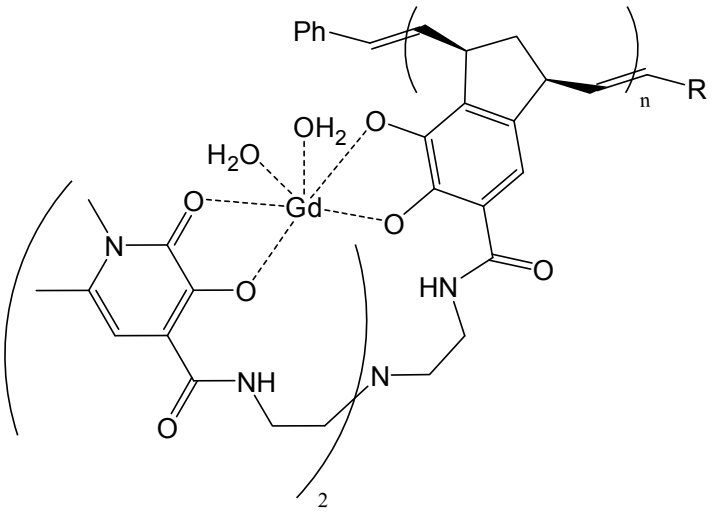

Figure 2-7. ROMP polymers based on HOPO ligand developed by Allen et al.

Polymers are the most direct way to attain macromolecular benefits and contrast agent systems. They suffer from inherent problems, such as polydispersity and high internal motion; however, future work can be carried out to address these issues using more controlled polymerizations and better polymer design. This is still a highly successful approach to

macromolecular contrast and warrants future work, especially in the areas of targeted imaging and drug delivery.

2.1.2 Dendrimers

Dendrimers have made huge contributions to the field of macromolecular contrast agents. Dendrimers can suffer from the same drawbacks as polymeric systems, such as polydispersity and internal flexibility to a lesser extent, but also provide a scaffold with a large molecular volume that can be functionalized with a high number and density of chelates per single molecule. The first reported dendrimer-contrast agent system and the best studied are based on polyamidoamine (PAMAM) dendrimers conjugated to Gd-chelates.[29] This first study directly compared PAMAM generation 2 and 6 (G2 and G6) dendrimers that had been functionalized with isothiolcyanobenzyl-DTPA chelating units (Figure 8-1). The G6 dendrimer had 170 Gd sites per molecule and a very high relaxivity of 34 mM^{-1} s^{-1}, which was higher then G2 r_1= 21.3 mM^{-1} s^{-1} at 25 MHz. The authors later showed this was related only to rotational correlation time gains.[30] The authors also showed that pharmokinetics were quite different between the two dendrimers. The G2 dendrimer behaved similarly to small molecular weight contrast agents in that it was quickly cleared from the blood pool, with little tissue retention, however, G6 had a long blood pool enhancement time of 200 min, which is quite long compared to Magnevist™ (Gd-DTPA) at 24 min. Later reports showed that the clearance route of these dendrimers had a generational dependence.[31,32] Interestingly, G2-G4 show exclusively renal clearance, G5 and G6 show renal and hepatic excretion, and G7- G10 show no renal clearance. Prolonged retention is ideal for vasculature imaging; however this ultimately limits clinical use. Unfortunately, the only candidates that are plausible for clinical use, based on clearance times and mechanisms are G2 based systems. The authors also examined hyperbranched diaminobutane (DAB) dendrimers

and found that G2 and G3 were the only acceptable systems. Later, *in vivo* studies have found interesting specific applications for PAMAM dendrimer-based contrast agents. Brechbiel and coworkers have successfully shown that G8 and higher PAMAM dendrimers can be used as reliable markers for tumor permeability and how it is affected by external radiation.[33] Star and coworkers showed that these dendritic contrast agents could be used as early markers to diagnose acute renal failure.[34] Konda *et al.* showed that PAMAM could be co-functionalized with DO3A and folate ligands to promote selective uptake and imaging of ovarian tumor xenografts.[35] Beautiful work carried out by Merbach and coworkers showed that PAMAM dendrimers can be functionalized in such a way as to make their relaxivity tunable based on the pH environment they are in, thus making the *in vivo* pH probes.[36]

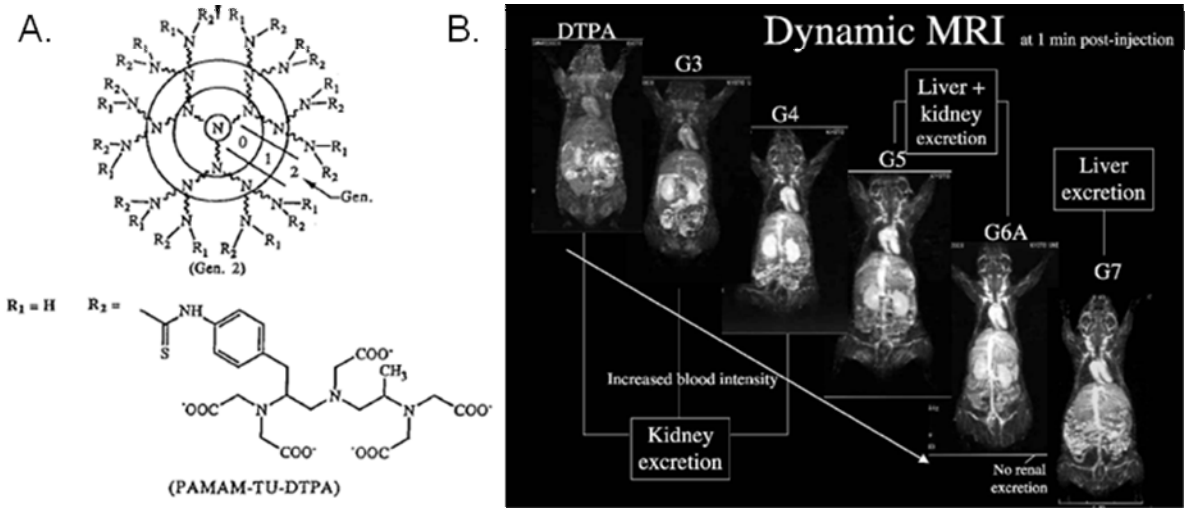

Figure 2-8. A) Diagram describing generations of PAMAM dendrimer and showing chelate connectivity with primary amines.[30] B) *In vivo* rat images showing dendrimer generation effect on contrast agent localization. Figure was used with permission from the American Chemical Society.

Though without the prominence of PAMAM contrast agent based dendrimers, other functionalized dendrimers have been studied extensively as contrast agents. One of the more

notable dendrimers is Gadomer-17™ (17 refers to its molecular weight of ~17kDa), developed by Schering-Plough.[37] Gadomer-17™ consists of DOTA-functionalized PLL arms extending from a 1, 3, 5 – benzenetricarboxylate core, as shown in Figure 2-9. The r_1 of this agent is 11.9 mM^{-1} s^{-1} at 40 MHz, which is better than low molecular weight contrast agents, but likely could be enhanced with more rigidity in the dendrimer. Several interesting *in vivo* studies have been carried out with Gadomer-17™. Brasch and coworkers showed that carcinomas have high uptake of Gadomer-17™ compared with Magnevist™, however neither contrast agent was successful at differentiating malignant tissue from benign tissue.[38] In follow up work, Kim *et al.* showed that tumor permeability could be measured with perfusion experiments using this dendrimer.[39] Gadomer-17™ was also successful in selectively enhancing lymph node contrast for detecting lymph node metathesis[40] and has been demonstrated as a suitable agent for visualizing pulmonary embolisms in pigs.[41] Recent work has shown Gadomer-17™ to be useful for imaging blockage in microvasculature.[42]

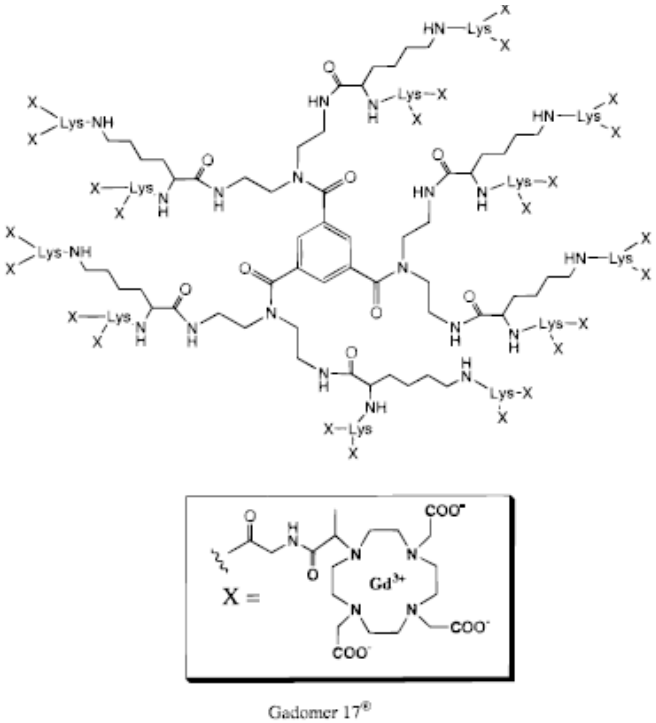

Figure 2-9. Chemical structure of Gadomer-17© adapted from Lauffer *et al.*[4] Figure adapted with permission from the American Chemical Society.

Newer dendritic systems based on PLL dendrimers have been created by Brasch and coworkers and are currently being studied in the clinic.[43] These macromolecules consist of a PEG chain with DTPA conjugated PLL dendrimers branching from each terminus. These two components allow the authors to tune the molecular weight and shape by varying either the PEG linker molecular weight or the dendrimer generation. Of the systems evaluated, the highest relaxivity reported (r_1= 10.1 mM^{-1} s^{-1}) was from the highest generation system, which consisted of PEG with M_n=3400 Da with G5 L-lysine dendrimers on its termini. The authors found that they could control blood lifetimes by varying PEG length, though increasing PEG length did not improve relaxivity. More extensive *in vivo* work indicated that Gd-DOTA analogues of these dendrimers selectively accumulated in breast cancer tissue and could be used to visualize these tumors.[44]

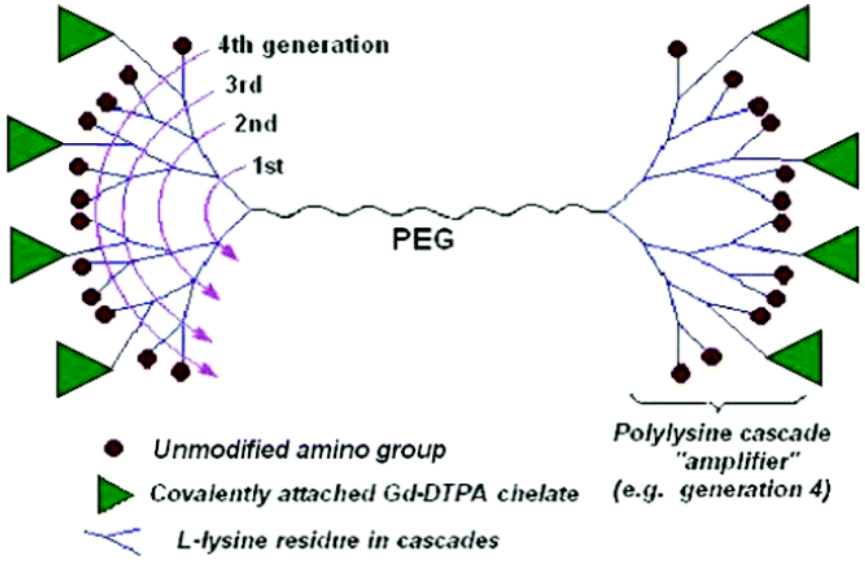

Figure 2-10. Schematic representation of PLL "bowtie" dendrimers adapted from Brasch *et al*.[43] Figure used with permission from the American Chemical Society.

All of the dendrimers mentioned thus far have their perimeter decorated with Gd-chelates of the DTPA or the DOTA type. Another approach towards dendronized contrast agents is to put the Gd-Chelate at the barycenter of the molecule, which improves relaxivity by drastically slowing its tumbling time, but eliminates the multimeric nature gained in other systems. One such agent explored in the literature is P760-Gd,[45] which is a dendritic molecule with a Gd-DOTA-based core that has PEG arms diverging out (Figure 2-11). The dendritic atmosphere surrounding the chelate imparts a slower rotational rate of 500 MHz (t_r = 2 ns) which is approaching MRI fields. This slowing of rotational correlation times led to r_1 = 23 mM^{-1} s^{-1} at 40 MHz, a very high relaxivity. Another example of barycenter-based contrast agents are the low generation dendrimers created by Pierre *et al.* using Gd-HOPO ligands.[46] A hydrophilic dendrimer environment is ideal for Gd-HOPO which has fast water exchange and q = 2, but suffers from fast tumbling and low water solubility, which are both corrected with dendrimer

formation. The relaxivity of these systems at 40 MHz was 18 mM^{-1} s^{-1} which was marginal compared with P760-Gd. This is because even though Gd-HOPO is dendronized, it still rotates at about 4.2 GHz (t_r = 238 ps), an order of magnitude faster than P760-Gd. Improving contrast agents by putting them at dendrimer barycenters is a newer and less explored approach towards improving contrast agents. This approach leads to well characterized, high relaxivity agents and therefore the outlook for these types of dendrimers is very good.

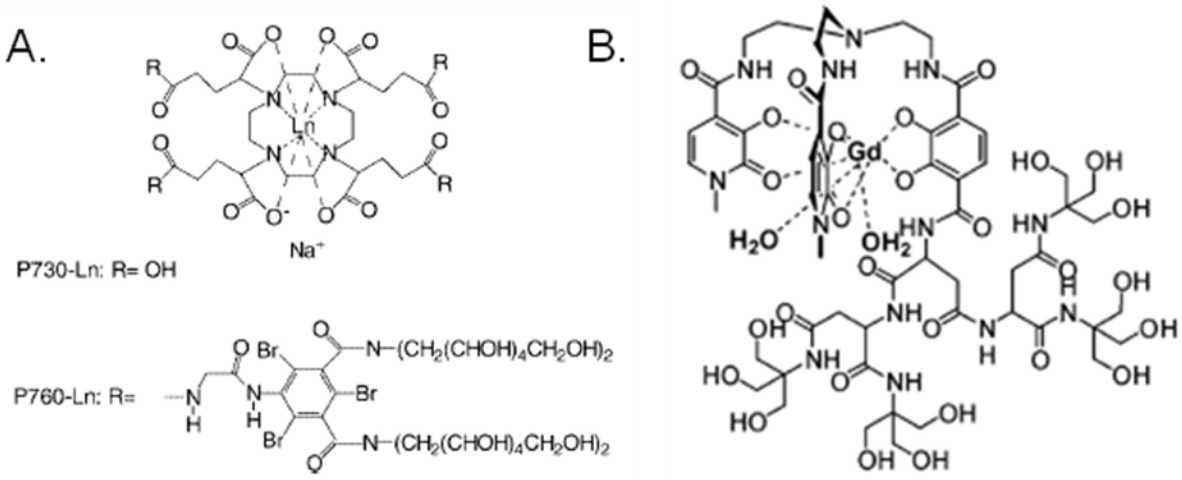

Figure 2-11. A) P-760 dendrimer by Muller *et al.*,[45] and B) HOPO dendrimer from Pierre *et al.*[46] Structures reproduced with permission.

2.1.3 Click-cluster and Metallocluster Based Systems

Glyco-based click-clusters have attracted the attention of several research groups due to their ability to mimic biological surfaces, their complex stereochemistry, and their unique binding/inclusion properties. Because of these features, there is an interest towards coupling glycoclusters with contrast agents. Tanaka *et al.* did an extensive study of the effect of DTPA-oligoamine stereo chemistry effect on relaxivity.[47] Unfortunately, the only MRI quantification they carried out was to do pixel intensity analysis of spin-echo images for each contrast agent

synthesized. This type of analysis gives qualitative data at best and offers no basis for comparison between the agents synthesized. Click-clusters based on cyclodextrin cores have also been of great interest to the contrast agent community. Song *et al.* synthesized β-cyclodextrins decorated with DOTA chelates, which they proposed to be useful as intracellular contrast agents.[48] Our group has also worked in this area and has generally found that methods carried out by Song *et al.* lead ultimately to impure final clusters, making them unacceptable for clinical applications.[49,50] The glycoclusters created by Reineke and coworkers utilize diethylenetriaminetetraacetic acid (DTTA) chelate groups, which enable the synthesis of pure glycoclusters with higher relaxivity than other analogues in their class.

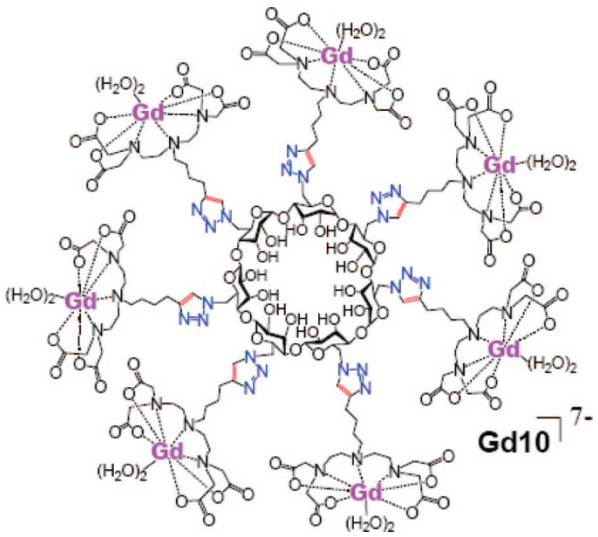

Figure 2-12. Click-clusters developed by Reineke and coworkers.[49] Figure used with permission from author and the American Chemical Society.

Like Click-clusters, metallocluster-based contrast agents have also shown great potential as contrast agents. Metalloclusters are multimeric Gd-chelate-clusters self-assembled using some other paramagnetic ion such as Fe(II) or Mn(II), via highly stable chelates such as bipyridine (bpy) and terpyridine (trpy). The enhancement in contrast due to their rigidity is

complimented by the enhancement imparted by the central assembly ion. This route towards easily assembled clusters was first proposed by Jacques *et al.* as MRI sensors for endogenous Fe(II).[51] Others have designed and tested similar cluster types based on bpy-DTTA type chelates,[52] trpy-DOTA and trpy-DTPA.[53] They found these "metallostars" to have extremely high relaxivity for their relatively lower molecular weight. In the bpy-DTTA case, which is exceptionally high, their increased relaxivity is attributed to the chelate having q = 2, high rigidity, a paramagnetic Fe(II) center, and slower rotational time due to self assembly. Pierre *et al.* applied similar thinking when designing their Fe(III)-templated self assembled contrast agents using multimeric HOPO ligand systems assembled with Fe(III) ions.[54] These systems, like the metallostars, have super nuclear relaxation dispersion profiles and rapidly assemble in the presence of the required Gd(III) and Fe ions.

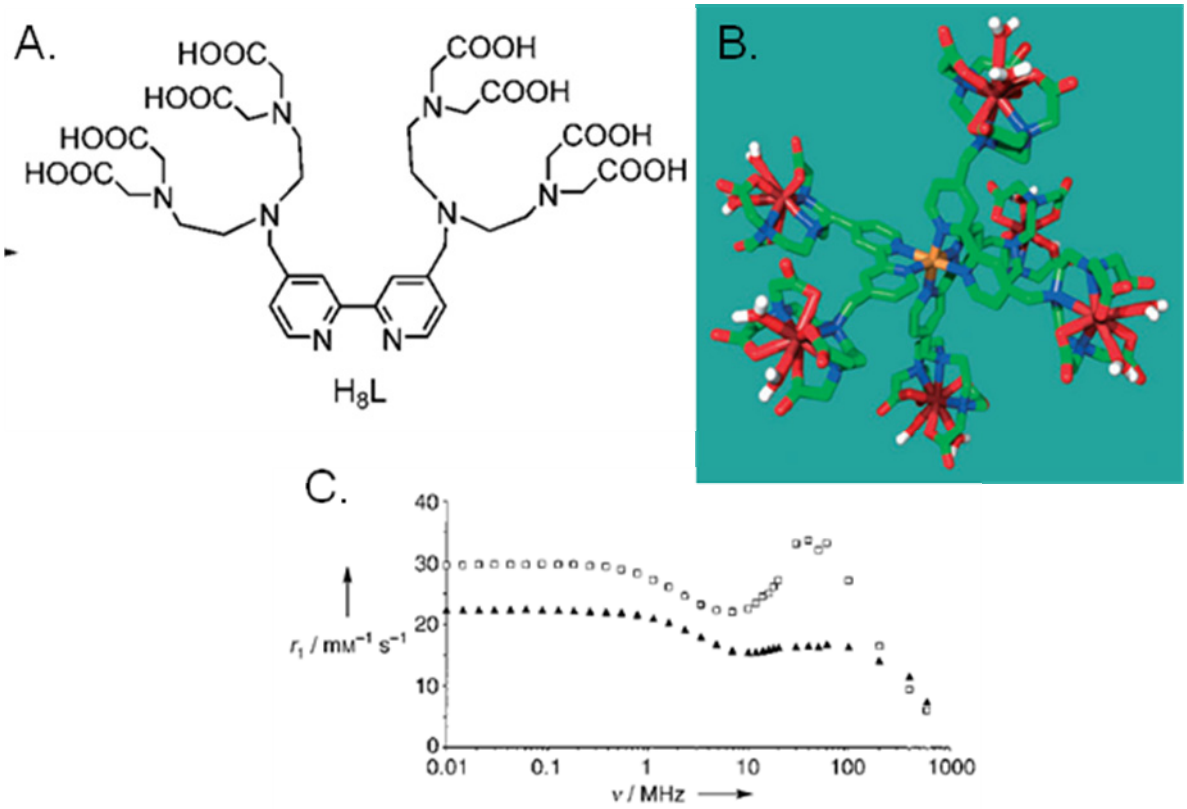

Figure 2-13. Metallostars developed by Merbach and Coworkers: A) bpy-DTTA ligand, B) a framework molecular model after ligand assembly with Fe(II) and Gd(III) ,and C) their NMRD profiles for Gd-DTTA-bpy without Fe(II) (black triangles) and with Fe(II) (white circles). Figure was used with permission.

2.1.4 Contrast agents non-covalently coupled to blood pool proteins

Another exciting approach toward reaping the benefits that macromolecules impart on contrast agents is using non-covalently labeled proteins related to specific physiological systems or regions, such as albumin, fibrin, and collagen.[55-57] The first highly successful demonstration of this was by Lauffer and coworkers in designing the now clinically approved blood pool imaging agent MS-325,[58] which selectively binds to serum albumin and gives stunning blood pool images as shown below in Figure 2-14. Furthermore, improved relaxivity was observed due to albumin binding, which slowed tumbling rates from gigahertz to megahertz (i.e. closer to MRI

Larmor frequencies).[59] The creators of MS-325 have translated the successful aspects of its design to other proteins of interest such as fibrin and collagen 1,[56, 57] both of which are prevalent markers of cardiovascular disease. A comprehensive review of all work carried out for MS-325 and analogs can be found in a recent review published by its creators.[60]

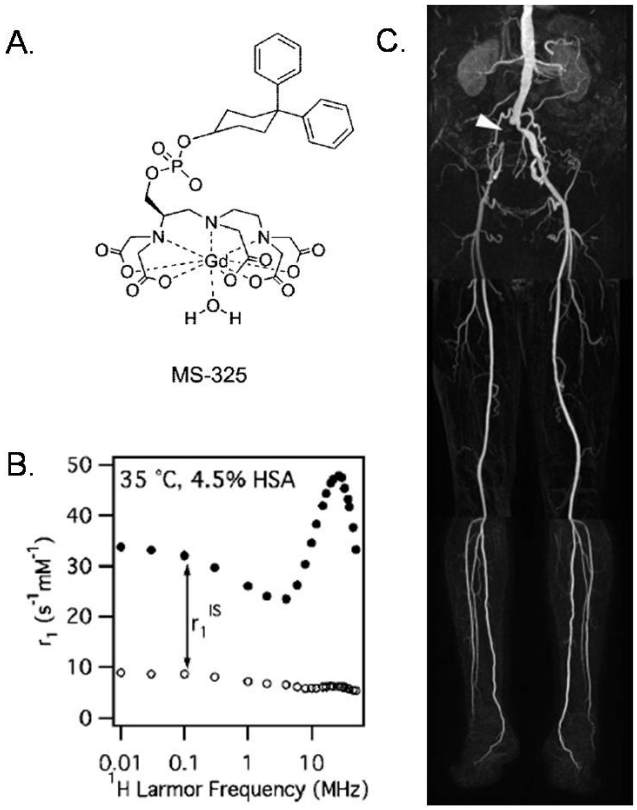

Figure 2-14. A) Serum protein binding contrast agent MS-325 developed by Lauffer and coworkers. B) NMRD profile of MS-325 (black circles) and MS-325 with water binding site blocked (white circles) both in serum, and C) blood pool image attained with MS-325 in a human subject.

2.1.5 Conclusions Regarding Macromolecular Contrast Agents

A significant body of work has contributed to our understanding of macromolecular contrast agents. Better understanding of biological distribution, relaxivity enhancements, and clearance mechanisms has allowed the scientific community to design exquisite macromolecular

contrast agents for imaging applications that simply were not possible before this technology existed. Future technology in this area likely will happen at the Gd-chelate level, by making chelates that are stable with higher q values, faster water exchange, and that are easy to conjugate or incorporate in to macromolecular systems. Currently, MRI is moving to higher fields and it will be necessary for contrast agents to follow suit. Other exciting developments will continue with multifunctional contrast agents that can both deliver drugs and provide imaging contrast. Macromolecular multimeric contrast agents are currently providing the best relaxivity enhancement possible coupled with potential use in various applications. Their prominence will likely extend well into the future of MRI contrast agents.

2.2 Probing Biological Systems with Luminescent Lanthanides

2.2.1 Introduction

To further extend the usefulness of Ln-chelates, it's desirable not only to visualize them at the tissue level using MRI, but also to visualize them at the microscopic level via fluorescence microscopy. With most lanthanides, due to luminescence associated with f-orbital excitation and emission, we have this ability. The lanthanides are a marvelous row of elements because the chemistry for all of them is largely the same in the 3+ oxidation state.[61] They preferentially form octadentate or nonadentate complexes and prefer bonds with oxygen. Because the f-orbitals are high energy and tucked closer to the nucleus then d-electrons, there is little covalent character in the bonds between the Ln(III) center and the chelating ligand, giving a purely ionic characteristic to the bonds that form these complexes.

Electrons in F-orbitals within Ln(III) complexes can undergo electronic transitions, which are considered forbidden because a change in electron spin must occur.[62] According to IUPAC rules, the energy release is technically a phosphorescence type mechanism and not fluorescence, though these rule are largely written for molecular orbital transitions.[63] Many experts in this field,[62-65] refer simply to phosphorescence behavior as luminescence in which this review will be consistent. As mentioned earlier, f-orbital electrons and chelate electrons are not shared, and therefore, their transitions are not affected by the chelate environment they are in. Luminescent lanthanides have some huge benefits over organic fluorophores in that they are not susceptible to O_2 quenching or photo-degradation. They also have large Stoke's shifts, long luminescence decay times, and narrow emission bands as shown below in Figure 2-15.[64] Because of these properties, lanthanides have received increased prominence in beacon and sensor development in biological systems.

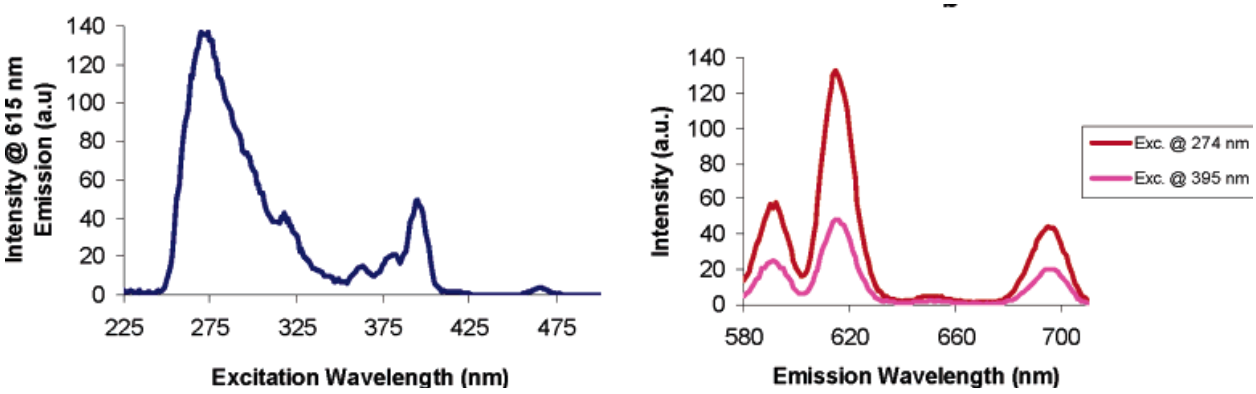

Figure 2-15. Typical excitation and emission profiles for Eu-chelates adapted with permission from the American Chemical Society.[64]

2.2.2 Imaging Luminescent Lanthanides in Biological Systems

Certainly the most prominent uses in biological systems for luminescent lanthanides are as labels in fluorescent microscopy techniques. One of the first accounts of this was by Marriott

and co-workers where they used Eu(III)-chelates and showed that after many minutes of excitation with UV light, no photo-bleaching occurred.[66] They also showed that auto fluorescence background could be gated out with time delay microscopy techniques, which utilize the long luminescence lifetimes of the Eu(III) chelates. Other techniques such as time-resolved long-lived luminescence imaging have shown lanthanides to have great utility as efficient image markers.[67] In this technique, they also rely on the long emission lifetimes of lanthanides to remove auto fluorescence. Recent work by Maury and coworkers has shown that luminescent lanthanides can be imaged via non-linear microscopy techniques such as two-photon microscopy,[68] further broadening their appeal to the microscopy community. Our group works extensively with luminescent lanthanides and has shown that lanthanides make excellent fluorophore markers for gene delivery using de-convoluted fluorescence microscopy coupled with modified filter cubes.[69] Further studies are currently being carried out to monitor these fluorophores with 2-photon imaging techniques.

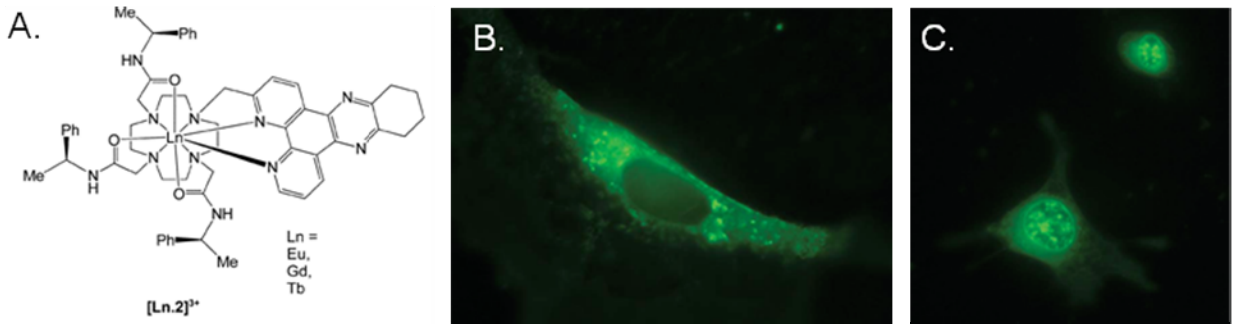

Figure 2-16 A) Tb-based agent developed by Parker and coworkers, and images after 4h and 24h. Lysosomal staining is predominant after 4h followed by nuclear staining after 24h. Figure adapted from with permission from *Organic and Bimolecular Chemistry*.[70]

Many groups have worked on making probes that contain lanthanides and can be used for cellular imaging. David Parker's group in the UK has done extensive work in making Ln-chelates for specific imaging applications such as genetic nuclear stains with high quantum efficiency (see Figure 2-16),[70] specific protein imaging,[71] and genetic material labeling capabilities.[72,73] This group has developed a comprehensive line of contrast agents which label various parts of cells *in vitro* (Figure 2-17). Interesting work in lanthanide probe development is being pursued by Charbonniere and coworkers, who are doing tissue imaging with lanthanides to image the blood brain barrier.[74] Much in line with work from David Parker, Jeane-Claude Bunzli is developing several complexes which have high quantum efficiency, and enable tracking of cell uptake by microscopy, and that respond to ion concentrations in cells.[75,76] Microscopy probes are not the only useful applications for luminescent lanthanides; they have also proven to be useful in other bio-assay applications. Yuan et al. showed that Ln-chelates make suitable labels in time-resolved DNA hybridization assays.[77] This body of work has all been carried out in the last ten years and shows the huge potential for lanthanides in molecular imaging for multiple parts of cells (Figure 2-17).

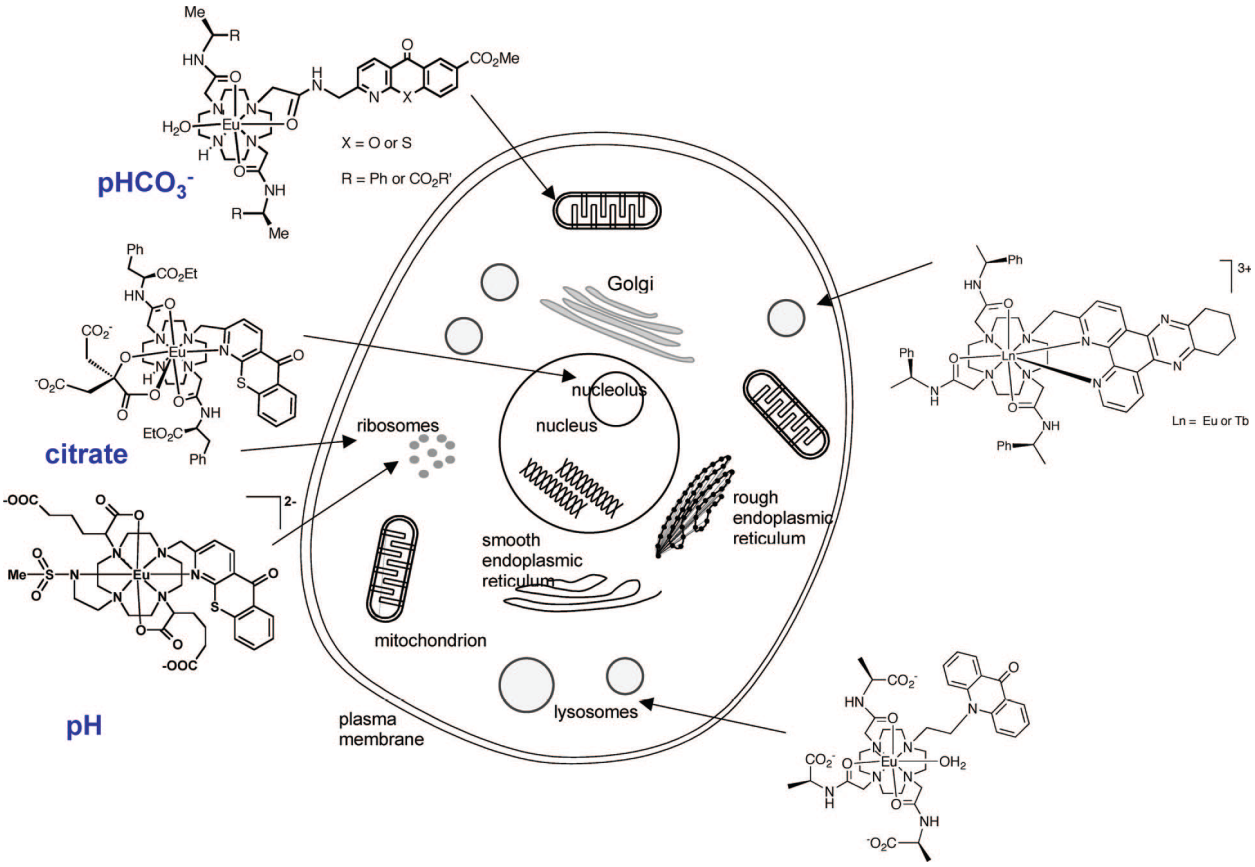

Figure 2-17. Various Ln-based agents have been created for cell labeling and their predominant locations, as shown in this figure adapted from Parker *et* al, with permission.[77] Blue labels represent what each agent is capable of sensing.

2.2.3 Conclusions and Outlook for Luminescent Lanthanides

Judging from the wealth of literature published on this subject over the last several years, it would be reasonable to suggest lanthanides will continue to grow in popularity for bioimaging applications. This dissertation will demonstrate the great utility lanthanides serve in bioimaging and, in our hands, the first successful attempt at direct polymer labeling and monitoring. The future outlook for this exciting class of imaging agents continues to improve as new imaging methodologies are developed and refined, such as non-linear microscopy and resonance transfer imaging techniques.

2.3 Monitoring Nucleic Acid Delivery *in vivo* and *in vitro*

2.3.1 Introduction

With the completion of the human genome project in 2003, modern medicine has learned much about genetic diseases, the molecular biology of disease pathways, and therapeutics based on nucleic acids.[78,79] Newer approaches to cure and treat disease are available to the scientific and medical communities, based on genetic approaches. There are hurdles however, that must be crossed for these new approaches to be viable. For instance, getting genetic materials to the required tissue, inside cells in that tissue, and into the nuclei in those cells, represents a real challenge due to the complex trafficking and sophisticated resistance humans have developed to prevent such events from occurring. Because of this, some sort of carrier is generally required for the polynucleotide material. Researchers have solved this with a variety of delivery approaches from viruses to molecular carriers, however no satisfactory clinical solution exists to date.

Macromolecules have a natural propensity towards drug delivery applications, especially for biological polymers like nucleic acids.[80-87] They escape many of the disadvantages associated with viral delivery, but their cellular trafficking and pharmakinetics are not as clear. Typically, synthetic polymers can be designed to associate with charged biomacromolecules via hydrogen bonding and electrostatic interactions. Ideally this process could be monitored via MRI and optical imaging, similar to the contrast agents and luminescent agents mentioned earlier, which would help to discern therapeutic pathways, and lead to the design of better delivery agents. Very comprehensive reviews have been published on the multitude of systems developed for macromolecular nucleic acid delivery,[88] but much more research needs to be

accomplished to determine the pharmokinetics, distribution and excretion mechanisms of these systems.

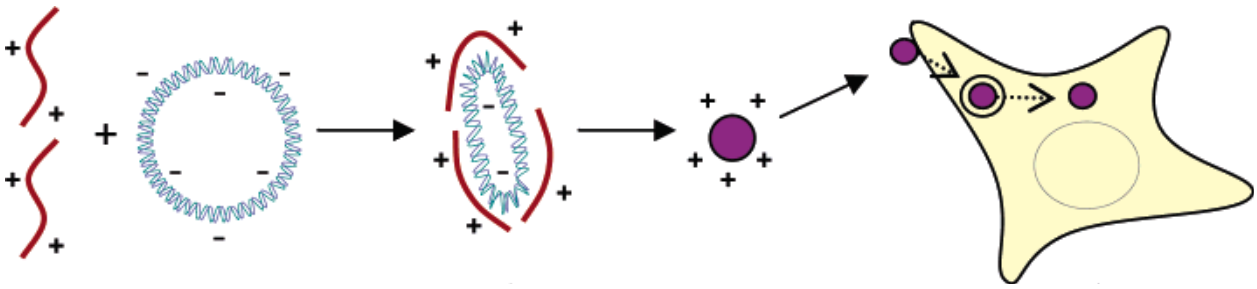

Figure 2-18. Macromolecule delivery of nucleic acids adapted with permission from *J. Am . Chem Soc.*, showing the several phases of macromolecular gene delivery. Red cationic polymer complexes with blue pDNA and compacts it into positively charged nanoparticle, that can be taken up by the cell.[83]

2.3.2 Monitoring Nucleic Acid Delivery

Imaging techniques have given some valuable information about viral nucleic acid delivery. Researchers have used a variety of strategies to image nucleic acid delivery both directly with conjugated beacons, and indirectly with reporter genes. Using radioimaging, researchers have directly labeled viruses with ^{111}In and ^{99M}Tc.[89,90] Delivery of siRNA using cationic proteins has been imaged *in vivo* using PET and SPECT.[91] Beautiful work carried out by David Corey and coworkers involved the delivery of naked ^{125}I labeled peptide nucleic acids (PNA), which were monitored and quantified by PET.[92]

An interesting approach to observe gene expression *in vivo* via MRI, was designed by Meade and coworkers.[93] Using a Gd-DOTA type ligand the chelate was modified so it would contain a covalently-linked galactose which blocks water coordination and exchange, essentially rendering the contrast agent ineffective. The galactose can be enzymatically cleaved in the

presence of β-galactosidase, which frees up the water binding/exchange sites on the contrast agent, and essentially "turns on" the agent.[94] To effectively demonstrate this *in vivo, Xenopus laevis* embryos were transfected with a β-galactosidase gene and subsequently injected with contrast agent. Compared with untransfected controls, the embryos with the enzyme showed distinct contrast in the transfected tissues (Figure 2-19)

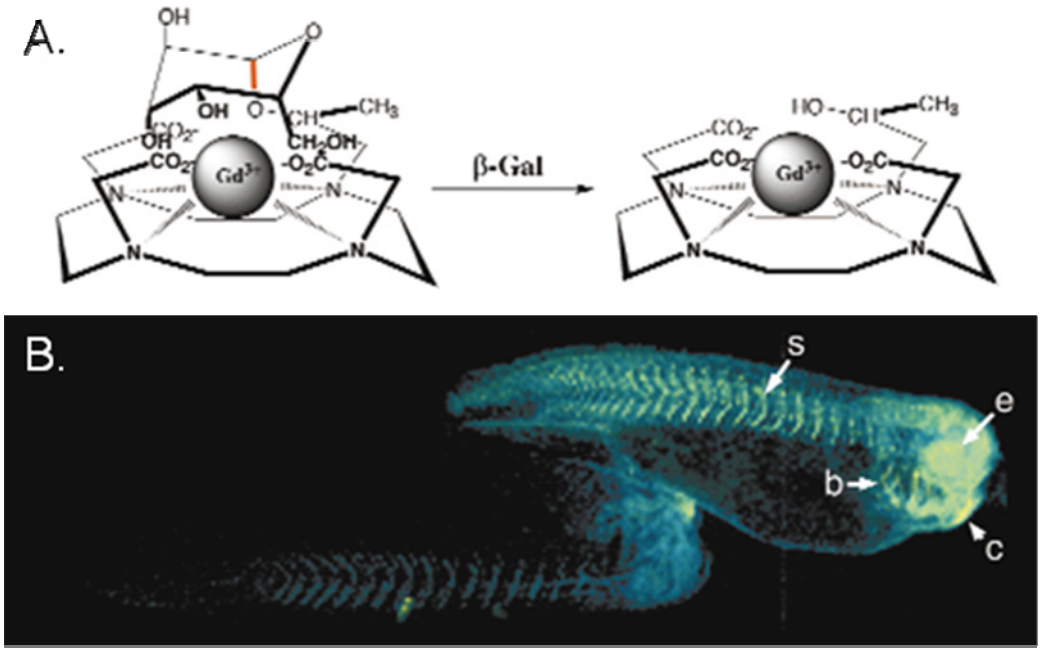

Figure 2-19. MRI agent that can be "turned on" by β-galactosidase reporter gene, developed by Fraser, Meade, and coworkers and reproduced with permission from *Nature Biotech*. A) The structure of the beta-galactosidase responsive contrast agent, and B) Pseudo-colored MR image of two *Xenopus laevis* embryos, both containing responsive contrast agent. The embryo on the right contains the reporter gene; the embryo on the left does not.[93]

Surprisingly, only very preliminary work has been carried out in imaging polyplex-type delivery systems *in vitro* and *in vivo*. Some of the first attempts to image polyplexes by MRI were carried out by Kayyem *et al.* where they took contrast agent labeled PLL and complexed it with a reporter gene.[95] This system was good for imaging, but had no transfection efficiency.

Recent work from Mark Davis' group at Caltech used ^{64}Cu-labelled siRNA complexes coupled with PET and CT imaging to study *in vivo* distribution and retention of his polyplexes, complimented with the delivery of a luciferase, as a means of bimodal imaging (Figure 2-20). This study allowed them to develop a very simple and clear model of nanoparticle uptake into tumors based on the enhanced permeability and retention (EPR) effect.[96]

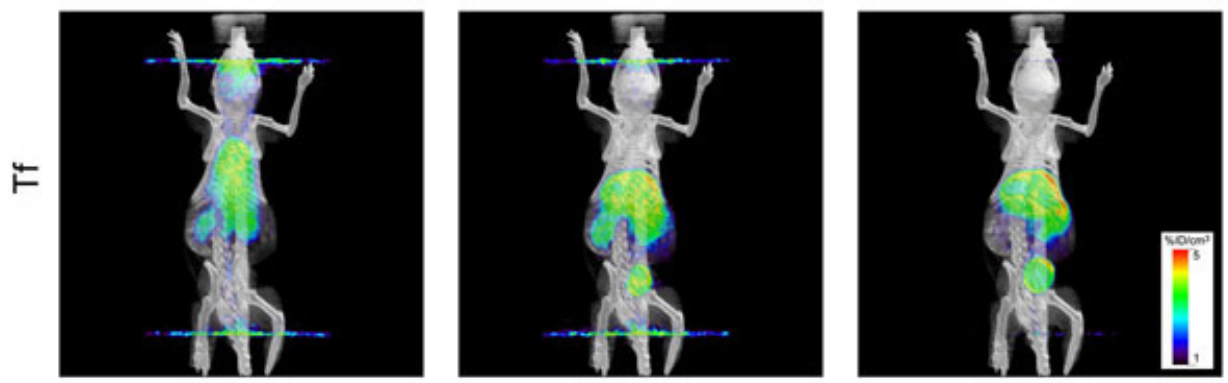

Figure 2-20. MicroPET images taken after injection with ^{64}Cu-labelled siRNA-polymer transferrin targeted nanoparticles. Time points for images are 1, 10, and 60 min. Figure adapted with permission from Davis et al. *Proc. Nat. Acad. Sci. U.S.A.*[96]

2.3.3 Conclusions Regarding Monitored Delivery

More work must be done to decipher the fundamentals of nanoparticle delivery of nucleic acids. Much of the current work being carried out in the Reineke group is related to this effort, especially work that appears in this dissertation. We have developed (*vide infra)* systems that deliver nucleic acids and allow this delivery to be imaged at both the microscopic and tissue scale levels, both *in vivo* and *in vitro*. Being able to answer fundamental questions related to uptake, location, excretion, and DNA release, will ultimately lead to better delivery systems and methodologies.

2.4 References:

1. Caravan, P. *Chem. Soc. Rev.* **2006**, *35*, 512 - 523.

2. Nobelprize.org

3. Macomber, R. S. *A complete Introduction to Modern NMR Spectroscopy*, **1998**, Wiley, New York.

4. Caravan, P.; Ellison, J. J.; McMurry, T. J.; Lauffer, R. B. *Chem. Rev.* **1999**, *99*, 2293 – 2352.

5. Aime, S.; Botta, M.; Fasano, M.; Terreno, E. *Chem. Soc. Rev.* **1998**, *27*, 19 – 29.

6. Datta, A.; Raymond, K. N.; *Acc. Chem. Res.* **2009,** *ASAP,* DOI: 10.1021/ar800250h.

7. Seiving, P. F.; Watson, A. D.; Rocklage, S. M.; Bioconjugate Chem. **1990**, *1*, 65 - 71.

8. Spanoghe, M.; Lanens, D.; Dommisse, R.; Van der Linden, A.; Alderweireldt; *Magn. Res. Imag.* **1992**, *10*, 913 - 917.

9. Ye, F.; Ke, T.; Jeong, E.-K., Wang, X.; Yongen, S.; Jonhnson, M.; Lu, Z.-R. *Mol. Pharm.* **2006**, *3,* 507 – 515.

10. Wen, X.; Jackson, E. F.; Price, R. E.; Kim, E. E.; Wu, Q.; Wallace, S.; Charnsangavej, C.; Gelovani, J. G.; Li, C. *Bioconjugate Chem.* **2004**, *15*, 1408-1415.

11. Huber, M. M.; Staubli, A. B.; Kustedjo, K.; Gray, M. H. B.; Shih, J.; Fraser, S. E.; Jacobs, R. E.; Meade, T. J. *Bioconjugate Chem.* **1998**, *9*, 242 - 249.

12. Aime, S.; Botta, M.; Crich, S. G.; Giovenzana, G.; Palminsano, G.; Sisti, M. *Chem. Comm.* **1999**, *1999*, 1577 – 1578.

13. Armitage, F. E.; Richardson, D. E.; Li, K. C. P. *Bioconjugate Chem.* **1990,** *1*, 365 – 374.

14. Rebizak, R.; Schaefer, M.; Dellacherie, É. *Bioconjugate Chem.* **1997**, *8*, 605 – 610.

15. Rebizak, R.; Schaefer, M.; Dellacherie, É. *Eur. J. Pharm. Sciences* **1998**, 243 – 248.

16. Siauve, N.; Clément, O.; Cuénod, A.; Benderbous, S.; Frija, G. *Magn. Res. Imag.* **1996**, *14*, 381 – 390.

17. Helbich, T. H.; Gossman, A.; Mareski, P. A.; Radüchel, B.; Roberts, T. P. L.; Shames, D. M.; Mühler, M.; Turetschek; Brasch, R. C. *J. Magn. Res. Imaging* **2000**, *11*, 694 – 701.

18. Desser, T. S.; Rubin, D. L.; Muller, H. H.; Qing, F.; Khodor, S.; Zanazzi, G.; Young, S. W.; Ladds, D. L.; Wellons, J. A.; Kellar, K. E.; Toner, J. L.; Snow, R. A. *J. Magn. Res. Imag.* **1994**, *4*, 467 – 472.

19. Ladd, D. L.; Hollister, R.; Peng, X.; Wei, D.; Wu, G.; Delecki, D.; Snow, R. A.; Toner, J. L.; Kellar, K.; Eck, J.; Desai, V. C.; Raymond, G.; Kinter, L. B.; Desser, T. S.; Rubin, D. L. *Bioconjugate Chem.* **1999**, *10*, 361 – 370.

20. Mohs, A. M.; Wang, X.; Goodrich, K. C.; Zong, Y.; Parker, D. L.; Lu, Z.-R. *Bioconjugate Chem.* **2004**, *15*, 1424 – 1430.

21. Yan, G., -P.; Zhuo, R., -X.; Xu, M., -Y., Zhang, X.; Li, L., -Y.; Liu, M. –L.; Ye, C. –H *Polym. Int.* **2002**, *51*, 892 – 898.

22. Kellar, K. E.; Henrichs, P. M.; Hollister, R.; Koenig, S. H.; Eck, J.; Wei, D. *Mag. Res. Med.* **1997**, *38*, 712 – 716.

23. Duarte, M. G.; Gil, M. H.; Peters, J. A.; Colet, J. M.; Elst, L. V.; Muller, R. N.; Geraldes, C. F. G. C. *Bioconjugate Chem.* **2001**, *12*, 170 -177.

24. Zong, Y.; Guo, J.; Ke, T.; Mohs, A. M.; Parker, D. L.; Lu, Z, -R *J. Cont. Rel.* **2006**, *112*, 350 – 356.

25. Benjamin, M.; Reineke, T. M. *Master's Thesis* **2006**, University of Cincinnati.

26. Allen, M. J.; Raines, R. T.; Kiessling, L. J. *J. Am. Chem. Soc.* **2006**, *128*, 6534 – 6535.

27. Kiessling, F.; Heilmann, T.; Lammers, T.; Ulbrich, K.; Subr, V.; Peschke, P.; Waengler, B.; Mier, W.; Schrenk, H, -H.; Bock, M.; Schad, L.; Semmler, W. *Bioconjugate Chem.* **2006**, *17*, 42 – 51.

28. Wu, Y.; Zhou, Y.; Ouari, O.; Woods, M.; Zhao, P.; Soesbe, T. C.; Keifer, G. E.; Sherry, A. D. *J. Am. Chem. Soc.* **2008**, *130*, 13854 – 13855.

29. Wiener, E. C.; Brechbiel, M. W.; Brothers, H.; Magin, R. L.; Gansow, O. A.; Tomalia, D. A.; Lauterbur, P. C. *Mag. Reson. Med.* **1994**, *31*, 1 – 8.

30. Wiener, E. C.; Auteri, F. P.; Chen, J. W.; Brechbiel, M. W.; Gansow, O. A.; Scheider, D. S.; Belford, R. L.; Clarkson, R. B.; Lauterbur, P. C. *J. Am. Chem. Soc.* **1996**, *118*, 7774 – 7782.

31. Kobayashi, H.; Kawamoto, S.; Jo, S. –K.; Bryant, H. L.; Brechbiel, M. W.; Star, R. A. *Bioconjugate Chem.* **2003**, *14*, 388 – 394.

32. Kobayashi, H.; Brechbiel, M. W. *Mol. Imaging* **2003**, *2*, 1 – 10.

33. Kobayashi, H.; Reijnders, K.; English, S.; Yordanov, A. T.; Milenic, D. E.; Sowers, A. L.; Citrin, D.; Krishna, M. C.; Waldmann, T. A.; Mitchell, J. B.; Brechbiel, M. W. *Clinical Canc. Res.* **2004**, *10*, 7712 – 7720.

34. Dear, J. W.; Kobayashi, H.; Brechbiel, M. W.; Star, R. A. *Nephron. Clin. Pract.* **2006**, *103*, c45 – c49.

35. Konda, S. D.; Aref, M.; Wang, S.; Brechbiel, M.; Wiener, E. C. *Magn. Res. Mat. Med. Biol.* **2001**, *12*, 104 – 113.

36. Laus, S.; Sour, A.; Ruloff, R.; Toth, E.; Merbach, A. E. *Chem. Eur. J.* **2005**, *11*, 3064 – 3076.

37. Raduchel, B.; Schmitt-Willich, H.; Platzek, J.; Ebert, W.; Frenzel, T.; Misselwitz, B.; Weinmann, H. –J. *Book of abstracts: 216th ACS national meeting,* **1998**, *PMSE-278.*

38. Daldrup-Link, H. E.; Shames, D. M.; Wendland, M.; Muhler, A.; Gossman, A.; Rosenau, W.; Brasch, R. C. *Acad. Radiol.* **2000**, *7*, 934 – 944.

39. Kim, Y. H.; Choi, B. I.; Cho, W. H.; Lim, S.; Moon, W. K.; Han, J. K.; Weinmann, H. – J.; Chang, K. –H *Invest. Rad.* **2003**, *38*, 539 – 549.

40. Misselwitz, B.; Schmidt-Willich, H.; Michaelis, M.; Oellinger, J. J. *Invest. Rad.* **2002**, *37*, 146 -151.

41. Fink, C.; Ley, S.; Puderbach, M.; Plathow, C.; Bock, M.; Kauczor, H. –U *Eur. Radiol.* **2004**, *14*, 1291 – 1296.

42. Krombach, G. A.; Higgins, C. B.; Chujo, M.; Saeed, M.; *Radiology* **2005**, *236*, 510 -518.

43. Fu, Y.; Raatschen, H. –J.; Nitecki, D. E.; Wendland, M. F.; Novikov, V.; Fournier, L. S.; Cyran, C.; Rogut, V.; Shames, D. M.; Brasch, R. C. *Biomacromolecules* **2007**, *8*, 1519 – 1529.

44. Cyran, C. C.; Fu, Y.; Raatschen, H. –J.; Rogut, V.; Chaopathomkul, B.; Shames, D. M.; Wendland, M. F.; Yeh, B. M.; Brasch, R. C. *J. Magn. Res. Imaging* **2008**, *27*, 581 – 589.

45. Elst, L. V.; Port, M.; Raynal, I.; Simonot, C.; Muller, R. N. *Eur. J. Inorg. Chem.* **2003**, 2495 – 2501.

46. Pierre, V. C.; Botta, M.; Raymond, K. N. *J. Am. Chem. Soc.* **2004**, *127*, 504 – 505.

47. Tanaka, H.; Ando, Y.; Wada, M.; Takahashi, T. *Org. Biomol. Chem.* **2005**, *3*, 3311 – 3328.

48. Song, Y.; Kohlmeir, E. K.; Meade, T. J. *J. Am. Chem. Soc.* **2008**, *130*, 6662 -6663.

49. Bryson, J. M.; Chu, W. –J.; Lee, J. –H.; Reineke, T. M. *Bioconjugate Chem.* **2008**, *19*, 1505 – 1509.

50. Srinivasachari, S.; Fichter, K. M.; Reineke, T. M. *J. Am. Chem. Soc.* **2008**, *130*, 4618 – 4627.

51. Jacques, V.; Desreux, J. F. *Topics Curr. Chem.* **2002**, *221*, 125 – 160.

52. Livramento, J. B.; Toth, E.; Sour, A.; Borel, A.; Merbach, A. E.; Ruloff, R.; *Angew. Chem. Int. Ed.* **2005**, *44*, 1480 – 1484.

53. Costa, J.; Ruloff, R.; Burai, L.; Helm, L.; Merbach, A. E. *J. Am. Chem. Soc.* **2005**, *127*, 5147 – 5157.

54. Pierre, V. C.; Botta, M.; Aime, S.; Raymond, K. N. **2006**, *128*, 9272 – 9273.

55. Caravan, P.; Das, B.; Dumas, S.; Epstein, F. H.; Helm, P. A.; Jacques, V.; Koerner, S.; Kolodziej, A.; Shen, L.; Sun, W. C.; Zhang, Z. *Angew. Chem., Int. Ed.* **2007**, *46*, 8171–8173.

56. Nair, S.; Kolodziej, A. F.; Bhole, G.; Greenfield, M. T.; McMurry, T. J.; Caravan, P. *Angew. Chem., Int. Ed.* **2008**, *47*, 4918–4921.

57. Zhang, Z.; Greenfield, M. T.; Spiller, M.; McMurry, T. J.; Lauffer, R. B.; Caravan, P. *Angew. Chem., Int. Ed.* **2005**, *44*, 6766–6769.

58. Lauffer, R. B.; Parmelee, D. J.; Dunham, S. U.; Ouellet, H. S.; Dolan, R. P.; Witte, S.; McMurry, T. J.; Walovitch, R. C. *Radiology* **1998**, *207*, 529–538.

59. Caravan, P.; Cloutier, N. J.; Greenfield, M. T.; McDermid, S. A.; Dunham, S. U.; Bulte, J. W.; Amedio, J. C., Jr.; Looby, R. J.; Supkowski, R. M.; Horrocks, W. D., Jr.; McMurry, T. J.; Lauffer, R. B. *J. Am. Chem. Soc.* **2002**, *124*, 3152–3162.

60. Caravan, P.; *Acc. Chem. Res.* **2009**, *ASAP*, DOI 10.1012/ar800220p.

61. Johnson, D. A. *J. CHem. Ed.* **1980**, *57*, 475 - 477.

62. Bunzli, J. –C. G. *Acc. Chem. Res.* **2006**, *39*, 53 – 61.

63. Bunzli, J. –C. G.; Piguet, C. *Chem. Soc. Rev.* **2005**, *34*, 1048 – 1077.

64. Gulgas, C. G.; Reineke, T. M. *Inorg. Chem.* **2005**, *44*, 9829 – 9836.

65. Gulgas, C. G.; Reineke, T. M. *Inorg. Chem.* **2008**, *47*, 1548 – 1559.

66. Marriott, G.; Heidecker, M.; Diamandis, E. P.; Yan-Marriott, Y.; *Biophysical J.* **1994**, *67*, 957 – 965.

67. Hanaoka, K.; Kikuchi, K.; Kobayashi, S.; Nagano, T. *J. Am. Chem. Soc.* **2007**, *129*, 13502 – 13509.

68. D'Aleo, A. *et al. Chem. Phys. Chem.* **2007**, *8*, 2152 – 2132.

69. Bryson, J. M.; Fichter, K. M.; Chu, W. –J.; Lee, J. -H.; Li, J.; Madsen, L. A.; Reineke, J. M. *Proc. Nat. Acad. Sci. U. S. A.* **2009**, in revision.

70. Poole, R. A.; Bobba, G.; Cann, M. J.; Frias, J. –C.; Parker, D.; Peacock, R. D. *Org. Biomol. Chem.* **2005**, *3*, 1013 – 1024.

71. Kielar, F.; Law, G. –L; New, E. J.; Parker, D. *Org. Biomol. Chem.* **2008**, *6*, 2256 – 2258.

72. Poole, R. A.; Montgomery, C. P.; New, E. J.; Congreve, A.; Parker, D.; Botta, M. *Org. Biomol. Chem.* **2007**, *5*, 2055 – 2062.

73. Montgomery, C. P.; Murray, B. S.; New, E. J.; Pal, R.; Parker, D. *Acc. Chem. Res.* **2009**, *ASAP* DOI:10.1021/ar800174z.

74. Claudel-Gillet, S.; Steibel, J.; Weibel, N.; Chauvin, T.; Port, M.; Raynal, I.; Toth, E. Ziessell, R. F.; Charbonniere, L. J. *Eur. J. Inorg. Chem.* **2008**, 2856 – 2862.

75. Deiters, E.; Song, B.; Chauvin, A. –S.; Vandevyver, C. D. B.; Gumy, F.; Bunzli, J. –C. *Chem. Eur. J.* **2009**, *15*, 885 – 900.

76. Song, B.; Vandevyver, C. D. B.; Chauvin, A. –S.; Bunzli, J. C. *Org. Biomol. Chem.* **2008**, *6*, 4125 – 4133.

77. Yaun, J.; Wang, G. *J. of Fluorescence* **2005**, *15*, 559 -568.

78. The international Human Genome Mapping Consortium. *Nature*, **2001**, *409*, 928 - 933.

79. The international Human Genome Mapping Consortium. *Nature*, **2001**, *409*, 934 – 941.

80. Davis, M. E.; Chen, Z.; Shin, D. M.; *Nat. Rev. Drug Discovery* **2008,** *7*, 771 - 782.

81. Jeong, J. H.; Mok, H.; Oh, Y. –K.; Park, T. G. *Bioconjugate Chem.* **2009**, *20*, 5-14.

82. Schaffert, D.; Wagner, E. *Gene Ther.* **2008**, *15,* 1132-1138.

83. Liu, Y.; Reineke, T. M. *J Am Chem Soc* **2005**, *127,* 300-3015.

84. Srinivasachari, S.; Liu, Y.; Zhang, G; Prevette, L.; Reineke, T. M. *J. Am. Chem. Soc. 128,* 8176-8184.

85. Srinivasachari, S.; Fichter, K. M.; Reineke, T. M. *J. Am. Chem. Soc.* **2008**, *130,* 4618-4627.

86. Davis, M. E. *Mol. Pharma.* **2009**, *6*, 659 – 668.

87. Layman, J. M.; Ramirez, S. M.; Green, M. D.; Long, T. E. *Biomacromolecules*, **2009**, *10*, 1244 -1252.

88. Mintzer, M. A.; Simanek, E. E. *Chem. Rev.* **2009**, *109*, 259 – 302.

89. Schellingerhout, D.; Rainov, N. G.; Breakfield, X. O.; Weissleder, R.; *Gene Ther.* **2000**, *2*, 288.

90. Bogdanov, A.; Weissleder, R. *Trends Biotechnol.* **2002**, *20*, S11 - S18.

91. Bogdanov, A. A. *J. Cell. Biochem.* **2008**, *104*, 1113 – 1123.

92. Lee, H. J.; Boabo, R. J.; Braasch, D. A.; Corey, D. R.; Partridge, W. M. *J. Nuc. Med.* **2002**, *7*, 948 – 956.

93. Louie, A. Y.; Huber, M. M.; Ahrens, E. T.; Rothbacher, U.; Moats, R.; Jacobs, R. E.; Fraser, S. E.; Meade, T. J. *Nature Biotech.* **2000**, *18*, 321 - 325.

94. Urbanczyk-Pearson, L. M.; Femia, F. J.; Smith, J.; Parigi, G.; Duimstra, J. A.; Eckermann, A. L.; Luchinat, C.; Meade, T. J. *Inorg. Chem.* **2008**, *47*, 56 – 68.

95. Kayyem, J. F.; Kumar, R. M.; Fraser, S. E.; Meade, T. J. *Chemistry and Biology* **1995**, *2*, 615 – 620.

96. Barlett, D. W.; Su, H.; Hildebrandt, I. J.; Weber, W. A.; Davis, M. E. **2007**, *104*, 15549 – 15554.

Chapter 3: A β-Cyclodextrin "Click Cluster" Decorated with Seven Paramagnetic Chelates Containing Two Water Exchange Sites*

*Chapter adapted from: Bryson, J. M.; Chu, W. –J.; Lee, J. –H.; Reineke, T. M. *Bioconjugate Chem.* **2008**, *19*, 1505 – 1509.

3.1 Abstract

The development of novel macromolecular contrast agents that offer enhanced relaxivity profiles at high magnetic fields have the potential to greatly improve the diagnosis, understanding, and treatment of disease. To this end, we have designed a monodiperse paramagnetic β-cyclodextrin click cluster decorated with seven paramagnetic arms. A novel alkyne-functionalized diethylenetriaminetetraacetic acid (DTTA) chelate (**6**) has been created and coupled to a per-azido-β-cyclodextrin core (**7**) to yield the precursor macromolecule (**8**). After removal of the protecting groups and titrating with Gd^{3+}, the final paramagnetic click cluster, **Gd10**, was obtained. Luminescence measurements were carried out in H_2O and D_2O on an analogous structure, **Eu10**, and indicated that at each lanthanide has an average of 1.8 water exchange sites, which is important for enhancing relaxivity and MRI resolution. This discrete paramagnetic click cluster yields a high relaxivity profile (43.4 mM^{-1} s^{-1} per molecule and 6.2 mM^{-1} s^{-1} per Gd^{3+} at 9.4 T) and enhanced contrast on a human MRI scanner as compared to a commercial agent, Magnevist (3.2 mM^{-1} s^{-1} at 9.4 T). Moreover, the useful inclusion properties exhibited by β-cyclodextrin also make this an excellent host scaffold to functionalize via noncovalent assembly with receptor specific targeting moieties for biomolecular imaging.

3.2 Introduction

Advancements in the design of novel imaging agents have the potential to transform biomedical research. Indeed, the ability to diagnose a disease at the earliest stage of onset and to understand the pathophysiological and treatment mechanisms of disease *in vivo* could revolutionize medicine. With such potential, magnetic resonance imaging (MRI) is a safe yet powerful diagnostic technique for visualizing soft tissue often with the aid of paramagnetic contrast agents (*1-3*). Chelate structures that contain Gd^{3+} improve imaging contrast by increasing the longitudinal relaxation time (T_1) of proximal water protons, which appear brighter in the T1-weighted image (*4*). To further increase resolution, MRI scanners are rapidly being developed with higher magnetic field strengths (*5,6*). Considerable efforts to create innovative agents that exhibit high relaxivities ($\mathbf{r}_1$) and tissue contrast at higher magnetic fields must follow suit (*1-6*).

Although current FDA-approved small molecule Gd^{3+}-chelates provide some contrast enhancement, they do not have optimal relaxivity profiles at high magnetic fields (*5,6*). Likewise, small agents do not provide contrast at very low concentrations, which is essential for biomolecular and targeted imaging (*1-6*). Conversely, macromolecular contrast agents show great promise for enhancing contrast, sensitivity, and diagnostic imaging time as they reveal slow vascular diffusion and clearance rates, and they can house multiple lanthanide chelates (*7-12*). However, a major drawback of existing paramagnetic macromolecules is that they suffer from polydispersity and difficulties in characterization, which could drastically affect clinical approval for diagnostic use (*9-13*).

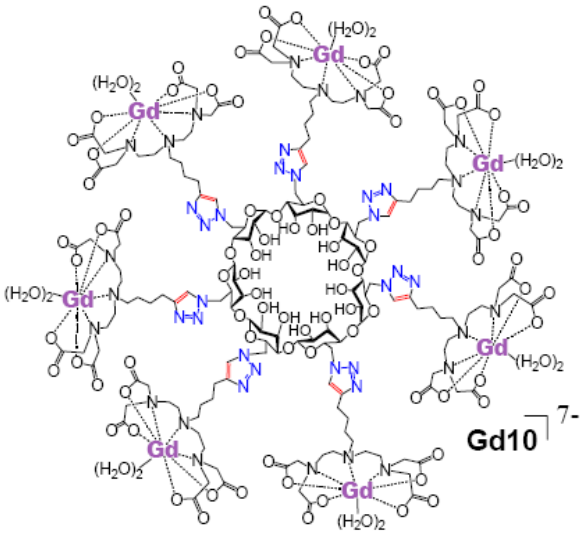

Figure 3-1: The target structure **Gd10**.

To this end, we present our efforts toward designing a novel macromolecular MRI contrast agent that is completely monodisperse, has a multivalent loading of Gd^{3+} chelates that house two water exchange sites, and reveals a high relaxivity profile at high magnetic fields (Figure 1). This architecture has been inspired by the biocompatibility of our polycationic β-cyclodextrin "click clusters", which are highly efficient nucleic acid delivery vehicles previously created by our lab (*13*). The structure has also been motivated by the interesting inclusion properties of the β-cyclodextrin scaffold. The hydrophobic cup can act as a host, endowing this macromolecule with a versatile modification method via non-covalent inclusion of hydrophobic guests that are linked to receptor-specific biomolecules (*14,15*). This potentially allows a multitude of targeted imaging applications for visualizing specific cell and tissue types, biomarkers or receptors, and enhancing diagnosis and treatment monitoring. Indeed, it is no surprise that others have realized the potential of the cyclodextrin scaffold with a related designs (*16*), particularly in a recently published paper developed in parallel to our work (*17*).

3.3 Materials and Methods

3.3.1 Materials

β-cyclodextrin was purchased from Wacker Chemie AG (Munich, Germany) and 6-bromohexyne was acquired from ChemSampCo (Philadelphia, PA). All other chemicals unless specified otherwise were purchased from Alfa Aeser Chemical Co. (Boston, MA) and were used without further purification. Acetylated per-azido-β-cyclodextrin, **7**, was synthesized according to a published procedures (*1*). The mass spectra were obtained on an IonSpec HiResESI mass spectrometer. NMR spectra were collected on a Bruker AV-400MHz spectrometer and relaxivity measurements were carried out on a Bruker AMX-400MHz spectrometer. Determination of the percentage of gadolinium content was determined with a Perkins-Elmer ELAN 6000 Inductively-Coupled Plasma Mass Spectrometer. Luminescence studies were performed using a Varian Cary Eclipse Fluorescence Spectrophotometer. Thin-layer chromatography (TLC) was performed using TLC plastic sheets (silica gel 60 F_{254}) from Merck (Darmstadt, Germany). Dialysis membranes [1000 molecular weight cutoff (MWCO)] were manufactured by Spectrum Laboratories, Inc. (Rancho Dominguez, CA). Magnetic resonance images were acquired with a Varian 4 Tesla MRI/MRS human scanner (170.35MHz)

3.3.2 Synthesis.

N^1,N^3-Bis(phthalimido)-N^2-benzoxycarbonyl-diethylenetriamine (2). 1,7-Bis(phthalimido)-1,4,7-triazaheptane, **1** (9.21g, 25.2 mmol), prepared by a previously published procedure (*2*), was slurried in 80ml of dichloromethane at 0°C under brisk stirring. 4-Dimethylaminopyridine

(1.25g, 10.2 mmol) and diisopropylethylamine (4.85g, 37.5 mmol) were then added to the slurry. Benzylchloroformate (5.12g, 30.0 mmol) was separately dissolved in 30ml of dichloromethane and added dropwise to the slurry over a period of 10 min, after which the reaction mixture became clear. The solution was then allowed to stir an additional 18h, after which the mixture was washed several times with 3 x 75ml acidic water (pH adjusted to 4 with 1M HCl), with saturated bicarbonate (1 x 75ml), and finally with ultrapure water (1 x 75ml). The washed organic fraction was dried over sodium sulfate and evaporated to give the crude product as an off-white solid. The crude solid was slurried in anhydrous diethylether, filtered, and washed again with ether (200mL) to remove the benzylchloroformate starting material. The final product was recovered and dried *in vacuo* yielding **2** a white solid (7.22g, 57.5%). ^{1}H-NMR ($CDCl_3$, 400MHz): δ = 3.62 (t, 4H), 3.91 (dt, 4H), 4.84 (s, 2H), 7.19 (d, 2H), 7.30 (m, 3H), 7.64 - 7.83 (m, 8H). ^{13}C-NMR ($CDCl_3$, 100MHz): δ = 35.7, 45.8, 67.3, 123.3, 127.6, 127.7, 128.3, 131.8, 134.0, 136.2, 156.1, 168.2. ES-MS positive ion mode: calculated *m/z* 520.148, [**2** + H^+]. Found *m/z*: 520.127.

N^2-Benzoxycarbonyl-diethylenetriamine (3). Compound **2** (7.22g, 14.5 mmol), was slurried in 25ml of acetonitrile. Hydrazine hydrate (5.80g, 116 mmol) was added to the mixture and after 10min of stirring, the solution became clear. After stirring the solution for approximately 4h, a precipitate formed, and after 24h, the reaction was complete (as determined via TLC). The white precipitate was filtered from the solution and washed thoroughly with acetonitrile. The initial solution was combined with the washings and dried *in vacuo* yielding the final product, **3**, as a viscous orange oil. (3.20g, 95.1%). ^{1}H-NMR ($CDCl_3$, 400MHz): δ = 1.93 (bs, 4H), 2.91 (s, 4H), 3.38 (s, 4h), 5.13 (s, 2H), 7.37 (m, 5H). ^{13}C-NMR ($CDCl_3$, 100MHz): δ = 38.4, 53.1, 67.3,

127.1, 127.6, 130.0, 136.1, 152.1. ES-MS positive ion mode: calculated *m/z* 238.156, [**3** + H^+]. Found *m/z*: 238.120.

N^2-Benzoxycarbonyl-diethylenetriamine-tetra-*t*-butylacetate (4). Compound **3** (3.20g, 13.5mmol) was dissolved in 22ml of DMF containing $KHCO_3$ (7.02g, 70.1 mmol) under stirring at room temperature. *Tert*-butyl-bromoacetate (13.7g, 70.1 mmol) was added directly to the stirred solution, which caused mild heat evolution. The reaction was allowed to stir for 48h at room temperature and then for an additional 2h at 60°C. The solution was then partitioned between diethyl ether and saturated sodium bicarbonate (50ml of each). After stirring for 5 min, the ether layer was retained and washed with ultrapure water (2 x 50ml), dried over anhydrous sodium sulfate, and evaporated to yield the crude product as a light yellow oil. The crude product was loaded onto a silica column and eluted using a solvent gradient (CH_2Cl_2 to 10% EtOAc : 90% CH_2Cl_2). The fractions containing the final product (second elution band) were combined and dried in vacuo yielding **4** (5.48g, 58.5%). ^{1}H-NMR ($CDCl_3$, 400MHz): δ = 1.46 (s, 36H), 2.88 (m, 4H), 3.40 (s, 8H), 3.47 (m, 4H), 5.12 (s, 2H), 7.36 (m, 5H). ^{13}C-NMR ($CDCl_3$, 100MHz): δ = 28.2, 46.5, 52.7, 56.1, 67.0, 80.9, 127.8, 127.9, 128.5, 137.1, 156.0, 170.6. ES-MS positive ion mode: calculated *m/z* 694.428, [**4** + H^+]. Found *m/z*: 694.448.

Diethylenetriamine-tetra-*t*-butylacetate (5). A 50ml round bottom flask containing a solution of **4** (3.34g, 4.8 mmol) dissolved in 25ml of MeOH, was purged with $Ar_{(g)}$ to remove dissolved $O_{2\,(g)}$. To remove the Cbz groups, catalyst (334 mg of Pd/C) was added to the flask which was again purged with $Ar_{(g)}$. Next, a balloon containing $H_{2\,(g)}$, fitted with a syringe, was used to bubble several liters of $H_{2\,(g)}$ through the solution at room temperature, and the solution was then

allowed to stir overnight. The solution was then filtered through celite to remove the catalyst and dried *in vacuo*, yielding compound **5** (2.43g, 90%) as a yellow oil. ^{1}H-NMR ($CDCl_3$, 400MHz): δ = 1.47 (s, 36H), 2.68 (t, 4H), 2.87 (t, 4H), 3.45 (s, 8H). ^{13}C-NMR ($CDCl_3$, 100MHz): δ = 28.0, 47.9, 54.3, 56.3, 80.8, 170.8. ES-MS positive ion mode: calculated *m/z* 560.390, [**5** + H^+]. Found *m/z*: 560.394.

N^2-(Hex-5-yne)-diethylenetriamine-tetra-*t*-butylacetate (6). Compound **5** (629mg, 1.12 mmol), 6-bromohexyne (322mg, 1.69 mmol), and $KHCO_3$ (113mg, 1.12mmol) were dissolved in 2 ml of DMF. The solution was allowed to stir for 48h at room temperature and then for 2h at 60°C. This solution was then added to a partition of diethyl ether and saturated sodium bicarbonate solution and stirred for 5 min. The ether layer was recovered and washed with ultrapure water (2 x 50ml), dried over anhydrous sodium sulfate, and evaporated *in vacuo* affording the crude product as a light yellow oil. The crude product was purified via silica gel flash chromatography using a solvent gradient (CH_2Cl_2 → 20% EtOAc: 80% CH_2Cl_2 →45% EtOAc: 45% CH_2Cl_2: 10% MeOH). The final compound was eluted out with the final gradient system, and the corresponding fractions were combined and dried *in vacuo* yielding **6** (324mg, 45.2%) as a yellow oil. ^{1}H-NMR ($CDCl_3$, 400MHz): δ = 1.47 (s, 36H), 1.54 (m, 4H), 1.95 (s, 1H), 2.20 (m, 2H), 2.48 (t, 2H), 2.61 (t, 4H), 2.80 (t, 4H), 3.46 (s, 8H) ^{13}C-NMR ($CDCl_3$, 100MHz): δ = 14.1, 18.2, 21.0, 26.2, 28.1, 52.9, 56.2, 60.3, 68.4, 80.8, 170.6. ES-MS positive ion mode: calculated *m/z* 640.454, [**7** + H^+]. Found *m/z*: 640.456.

Heptakis{2,3-di-*O*-acetyl-6-*N*-[(diethylenetriamine-tetra-*t*-butylacetate)butyl]-6-(1,2,3-triazole)} cyclomaltoheptaose (8). Compounds **6** (69.5mg, 1.09 x 10^{-4} mol) and **7** (29.4mg, 1.55 x 10^{-5} mol) were dissolved in 2.6 ml of a 1:1 THF:water solution. Fresh solutions of 1M $CuSO_4 \cdot 5H_2O$ and 1M sodium ascorbate were prepared and used to introduce the catalyst 5% $CuSO_4$ and 10% sodium ascorbate (as molar percent of **6**) to the reaction mixture to promote the click coupling reaction. This mixture was stirred briefly at 60°C to promote dispersion and was then stirred at room temperature until the solution became turquoise-blue (after about 8h), which signified reaction completion. The reaction mixture was then partitioned between water and dichloromethane (10ml of each) and stirred for 2 min. The dichloromethane layer was retained and washed with a 0.1M Na^+ EDTA solution (2 x 10ml) and ultrapure water (2 x 10mL). The organic layer was dried over sodium sulfate and evaporated *in vacuo* yielding **8** (95mg, 96%) as a viscous yellow oil. ^{1}H-NMR ($CDCl_3$, 400MHz): δ = 1.23 (m, 14H), 1.42 (s, 252H), 1.53 (m, 14H), 1.61 (m, 14H), 1.98 (s, 21H), 2.03 (s, 21H), 2.48 (d, 14H), 2.59 (bs, 28H), 2.77 (bs, 28H), 2.95 (m, 14H), 3.41 (s, 56H), 4.44 (m, 7H), 4.70 (d, 7H), 4.91 (m, 7H), 5.31 (m, 7H), 5.59 (s, 7H), 7.53 (s, 7H). ^{13}C-NMR ($CDCl_3$, 100MHz): δ = 20.8, 25.6, 25.7, 27.4, 27.9, 28.2, 29.7, 50.9, 52.2, 53.1, 54.8, 67.9, 70.9, 80.7, 96.2, 100.0, 123.5, 148.3, 168.2, 170.6. ES-MS positive ion mode M_{obs}: Calculated *m/z* 1595.43, [**8** + $4H^+$]. Found *m/z*: 1595.27. Calculated *m/z*: 1276.54, [**(8)** + $5H^+$]. Found *m/z*: 1276.40. Calculated *m/z* 1063.95, [**(8)** + $6H^+$]. Found *m/z*: 1063.88. Calculated *m/z* 912.107, [**(8)** +$7H^+$]. Found *m/z*: 912.028. Deconvolution of spectrum: Found *m/z*: 6377.38. Calculated *m/z* 6377.70, [**8** + H^+].

Heptakis{6-*N*-[(diethylenetriamine-tetraaceticacid)butyl]-6-(1,2,3-triazole)} cyclomaltoheptaose (9). Compound **8** (85mg, 1.33 x 10^{-5} mol) was dissolved in 2ml of MeOH,

the solution was adjusted to a pH = 8 with NaOMe, and the mixture was allowed to stir overnight. The pH was brought back to neutral using Amberlyst® strong cation exchange resin, the resin was filtered from the mixture, and the solvent was removed to yield the deacetylated product. This product was then redissolved in 2ml of dichloromethane and cooled to 0°C. Triethyl silane (TES) was added (100µl), followed by 1ml of trifluoroacetic acid (TFA). The solution was warmed to room temperature and stirred for 3h, after which the TFA/TES mixture was removed *in vacuo* leaving a viscous oil. Anhydrous ether was added to the oil and allowed to sonicate for 5 min, yielding a fine white precipitate. The white powder was recovered and dissolved in 2ml of water, brought to pH = 7 with $NaHCO_3$ and dialyzed extensively against ultrapure water in a 1000 MWCO membrane. The purified solution was lyophilized to dryness yielding **9** (41mg, 73%) as a fluffy white solid. It should be noted that this product (**9**) is very hygroscopic and rapidly uptakes water from the air if not stored in a dessicator. ^{1}H-NMR (D_2O, 400MHz): δ = 1.80 (bs, 14H), 1.86 (bs, 14H), 1.92 (bs, 14H), 2.07 (bs, 14H), 2.39 (s, 14H), 2.30 (bs, 28H), 3.32 (bs, 28H), 3.44 (m, 7H), 3.58 (m, 7H), 3.84 (m, 7H), 3.93 (m, 7H), 3.99 (m, 7H), 4.16 (s, 56H), 7.87 (s, 7H). ^{13}C-NMR (D_2O, 100MHz): δ = 20.5, 24.8, 27.4, 48.1, 52.1, 52.8, 57.3, 58.0, 70.1, 70.6, 71.4, 76.8, 95.5, 125.1, 135.4, 170.8, 172.8. ES-MS positive ion mode deconvoluted mass $[9 + H^+]^{1+}$: Calculated *m/z* 4216.79, Found *m/z*: 4217.97. FT-IR: (KBr pellets, cm^{-1}) 3430.7, 2910.2, 1681.75, 1600.2, 1404.6, 1204.6, 1136.8, 1049.0.

Heptakis{6-*N*-[(Gd(III)-diethylenetriamine-tetraaceticacid)butyl]-6-(1,2,3-triazole)} cyclomaltoheptaose (Gd10). Compound **9** (25.2mg, 5.98 x 10^{-6}mol) was dissolved in 5ml of ultrapure water and the solution was adjusted to pH=7 with sodium bicarbonate. Gadolinium chloride hexahydrate (15.6mg, 4.18 x 10^{-5}mol) was dissolved in 1ml of ultrapure water and

added to the solution of **9** in 3 separate aliquots. After the addition of each aliquot, the pH was adjusted back to a pH between 8 - 9 using a 0.1 M potassium carbonate solution. The solution was allowed to stir for 30min to allow for Gd chelation to occur, dialyzed against ultrapure water for 18h, and lyophilized to yield **Gd10** as a fluffy white solid (27.3mg, 78%). ICP-MS: %Gd(III): theoretical for $\{C_{168}H_{238}Gd_7K_7N_{42}O_{84} + (H_2O)_{14}\}$ = 18.9%; Found 18.8%. The ES-MS for **Gd10** is displayed below in Figure S2. ES-MS negative ion mode: calculated *m/z* 755.863 [**(Gd10)**]$^{7-}$. Found *m/z*: 755.421. Calculated *m/z:* 882.070 [**(Gd10)** + H^+] $^{6-}$. Found *m/z*: 882.239. Calculated *m/z:* 1058.61 [**(Gd10)** + $2H^+$]$^{5-}$. Found *m/z*: 1058. 84. Calculated *m/z:* 1323.51 [**(Gd10)** + $3H^+$] $^{4-}$. Found *m/z*: 1323.59. FT-IR: (KBr pellets, cm^{-1}) 3422.5, 2935.9, 1750.0, 1609.9, 1402.7, 1248.9, 1048.0.

Heptakis{6-*N*-[(Eu(III)-diethylenetriamine-tetraaceticacid)butyl]-6-(1,2,3-triazole)} cyclomaltoheptaose (Eu10). Compound **9** (2.10mg, 4.98 x 10^{-7} mol) was dissolved in 0.5ml of ultrapure water and the solution was adjusted to pH=7 with sodium bicarbonate. A freshly prepared 1mM solution $EuCl_3 \cdot 6H_2O$ (498µl, 4.98 x 10^{-7} mol) was added to the solution of compound **9** in a similar manner to **Gd10**. The pH was then adjusted back to 7 - 8 using a 0.1M potassium carbonate solution. The solution was dialyzed against water and lyophilized to give **Eu10** (1.7mg, 65%) as a fluffy white solid. ICP-MS: %Eu(III): Theoretical for $\{C_{168}H_{238}Eu_7K_7N_{42}O_{84} + (H_2O)_{14}\}$ = 18.4%; Found = 22.0%. ES-MS negative ion mode: calculated *m/z* 750.717 [**(Eu10)**]$^{7-}$. Found *m/z*: 750.352. Calculated *m/z:* 875.838 [**(Eu10)** + H^+] $^{6-}$. Found *m/z*: 875.732. Calculated *m/z:* 1051.21 [**(Eu10)** + $2H^+$]$^{5-}$. Found *m/z*: 1051.42. Calculated *m/z:* 1314.26 [**(Eu10)** + $3H^+$] $^{4-}$. Found *m/z*: 1314.33. FT-IR: (KBr pellets, cm^{-1}) 3421.1, 2936.1, 1750.0, 1610.1, 1401.8, 1248.8, 1047.9.

3.3.3 ICP-MS for Ln Quantification

$GdCl_3$ and $EuCl_3$ 1,000ppm lanthanide standard solutions in 1% HNO_3 (Aldrich, St. Lois, MO) were used to prepare a stock solution containing 1.00 ppm of both Eu^{3+} and Gd^{3+}, which was used to prepare 500, 250, 100, 50, 10, and 5 ppb solutions. These solutions were analyzed for four Gd^{3+} isotopes (156, 157, 158, 160), and 2 Eu^{3+} isotopes (151, 153). This data was used to generate a calibration curves for both Gd(III) and Eu(III). Solutions of **Gd10** and **Eu10** (100 ppb) were prepared, analyzed, and the lanthanide content was determined for each sample according to the calibration curve. The Gd^{3+} content in **Gd10** was found to be 18.8 ppb and the Eu^{3+} content for **Eu10** was found to be 22.0 ppb.

3.3.4 Determination of water coordination number (*q*)

Determination of the luminescence lifetime (τ) of **Eu10** was performed in both H_2O and D_2O (5.0×10^{-5} M) with a delay time of 0.05 ms, a gate time of 0.2 ms, $\lambda_{ex} = 395$, and $\lambda_{em} = 614$ nm. Excitation and emission slits were set to 10 nm. Calculations of *q,* were carried out in Graphpad prism v10.0 using the equation of $q = 1.11 [k_{H2O} - k_{D2O} - 0.31]$, where k is the rate of luminescence decay.

3.3.5 Relaxivity Measurements

Stock solutions of Magnevist™ and **Gd10** (2.95mM = $[Gd^{3+}]$) were prepared in H_2O and diluted to make 1.48 mM and 0.738 mM solutions. The longitudinal relaxation time (T_1) for the six solutions and water were measured using an inversion recovery pulse sequence (180° – d_t – 90° – acquire) carried out on a Bruker AMX-400 MHz spectrometer at 310K. Arrayed data

($n(d_t) = 14$) was processed using NUTS software and fit to a three-parameter model. Relaxivity was acquired from a linear least squares fit of the slope of the line obtained from plotting $1/T_1$ vs. [Gd].

3.3.6 T_1 weighted Images

Solutions of Magnevist™ and **Gd10**, were prepare so $[Gd^{3+}] = 1.11$mM, and put in 25mL vials to be imaged. The images were acquired with gradient echo pulse sequence using a TEM (transverse electromagnetic) volume coil. Acquisition parameters are as follows: TR (repetition time) = 50 msec, TE (echo time) = 5 msec, FOV (field of view) = 200x200 mm and matrix size = 128x128. Contrast was adjusted relative to the controls.

3.4 Discussion

Scheme 3-1: Synthetic Protocol for Alkyne-DTTA arm synthesis.[a]

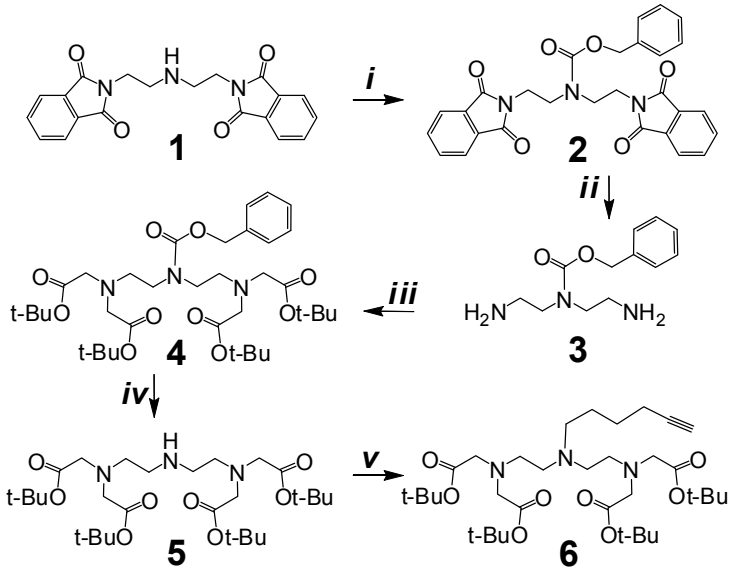

[a] *i*) Benzylchloroformate, DIPEA, DMAP, CH_2Cl_2; *ii*) Hydrazine monohydrate, MeCN; *iii*) t-butyl bromoacetate, DMF, $KHCO_3$; *iv*) H_2, Pd/C 10%, MeOH; *v*) 6-bromo-1-hexyne, $KHCO_3$, DMF.

A convergent synthetic approach was designed to yield our target structure. The synthesis of the novel dendrons, the alkyne functionalized Gd^{3+} chelates, was inspired by the works of Merbach et al. (*18*) Their studies have shown that DTTA-type ligands have high lanthanide binding stability, fast water exchange, and multiple water coordination sites, which yield excellent relaxivity profiles (*18,19*). In addition to the multivalent architecture, the key feature of our structure is the design of the arms, which consist of a chelate structure that has two open water exchange sites on the lanthanide for enhancing relaxivity. Scheme 3-1 was initialized with an amino bis-ethylphthalimide (**1**), which was prepared as previously reported (*20*). Next, the secondary amine was protected with a benzyl carbomate (Cbz) group (**2**) and the primary amines were liberated via hydrazine hydrate in acetronitrile, affording the diamine, **3**. This structure was then reacted with t-butyl bromoacetate, creating the functionalized tertiary amine (**4**), and the

CBz removed via hydrogenation yielding the chelate precursor (**5**). It is worth mentioning that *t*-butyl-bromoacetate was utilized in this synthetic route as the related n-methyl-bromoacetate analogue (potentially milder basic deprotection) allowed an intramolecular cyclization to occur with the free secondary amine upon CBz removal, which could not be carried forth in the reaction scheme. A simple nucleophilic addition of **5** to 6-bromohexyne resulted in the desired protected DTTA-hexyne dendron (**6**). A crucial step in the formation of these *monodisperse* click clusters is the synthesis of the acetylated per-azido-β-cyclodextrin core (**7**) moiety. It is important to note here that the commercially-available per-halogenated β-cyclodextrin analogs have an unacceptable percentage of lesser substituted impurities (up to 10%, as noted by the manufacturer), which ultimately lead to contamination of the final structure with lesser-substituted products. Because of the negative implication of a polydisperse final product, we found it important to synthesize the pure acetylated per-azido-β-cyclodextrin core (**7**) according to previous reports, which lead us to a fully 7-substituted product of higher purity (*vide infra*) (*13, 21, 22*).

Scheme 3-2: Synthesis of the Paramagnetic Click Cluster, Gd10.[b]

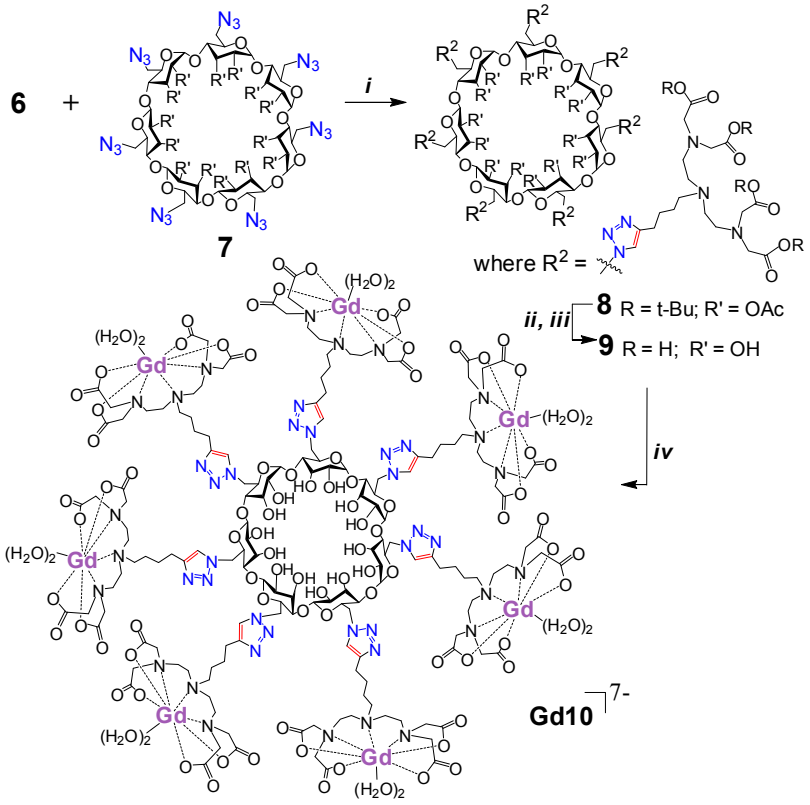

[b] *i*) $CuSO_4 \cdot 5H_2O$, Sodium Ascorbate, THF:H_2O (1:1), 60°C; *ii*) NaOMe, MeOH, 24h; *iii*) TFA, 3h; *iv*) $GdCl_3$, $NaHCO_3$, pH= 6-8.

The key step in the assembly of the target click cluster was carried out via the click reaction, which promotes regio-specific coupling in high yield even in sterically-hindered environments (*23,24*). As shown in Scheme 3-2, the protected DTTA-hexyne dendron (**6**) was coupled to the acetylated per-azido-β-cyclodextrin (**7**). The clean formation of the fully-substituted 1,4-regioisomer (**8**) was evidenced by mass spectra (Figure 3-2) and NMR (see Appendix A). Because both the DTTA carboxylates and the β-cyclodextrin hydroxyls are protected, chelation of copper from the catalyst and retention of this metal in the final product was not found. Next, the acetyl and t-butyl groups on the click cluster were deprotected via conventional methods creating **9**, which was then titrated with $GdCl_3$, yielding the target paramagnetic macromolecule, **Gd10**. This β-cyclodextrin click cluster was purified via

exhaustive dialysis in ultra pure water. Quantification of Gd^{3+} loading and full chelation was revealed via mass spec and ICP-MS analysis, which showed the presence of seven loaded chelates without lower chelation products or excess Gd^{3+}.

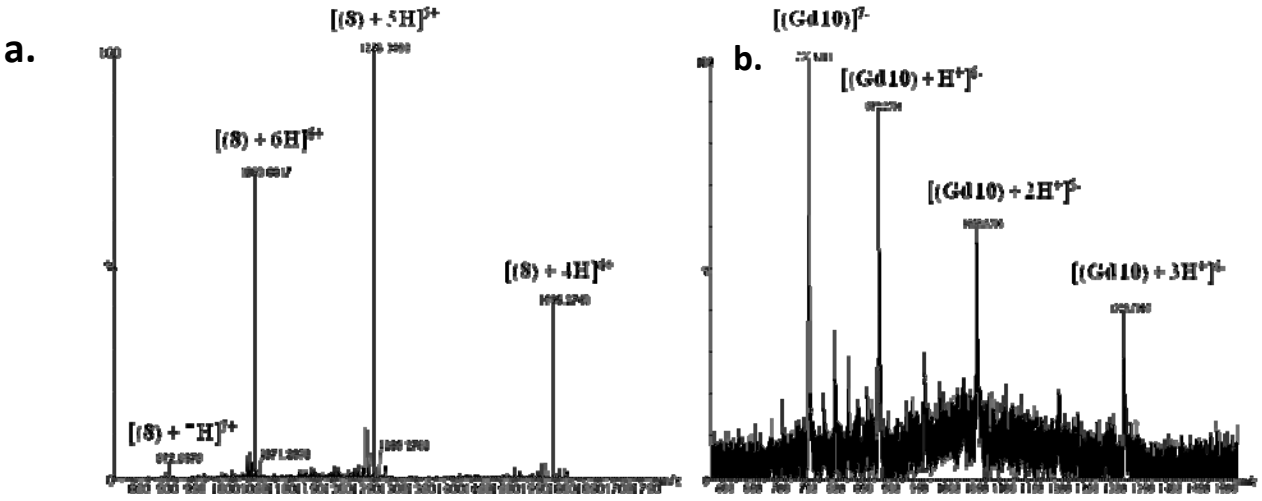

Figure 3-2: ESI-MS of a) **8**, and b) **Gd10**.

Contrast agent efficacy is influenced by the chelation environment and water coordination number (*q*). To gain insight into the average *q* value, **9** was chelated with Eu3+, creating **Eu10**, a luminescent analogue of **Gd10** (figure 3-3). As Eu^{3+} and Gd^{3+} have identical coordination chemistry (*25*), *q* can be determined with **Eu10** from the proportionality between the luminescence decay in H_2O and D_2O via the Horrocks equation [$q = 1.11 (kH_2O - kD_2O - 0.31)$] (*26*). Typically, Gd^{3+} and Eu^{3+} prefer nonadentate coordination and the DTTA-like chelate usually forms a heptadentate complex, therefore a *q* value of 2 is predicted. From this experiment, a *q* value of 1.8 was calculated, which is within reasonable error of the predicted value. It has been shown that hydroxyls on adjacent groups can block water coordinate sites within related lanthanide chelates (*27*). However, this study of the analogous **Eu10** structure suggests that the two open coordination sites on the lanthanide chelates are available for water exchange, which is essential for maximal relaxivity enhancement, particularly at higher fields.

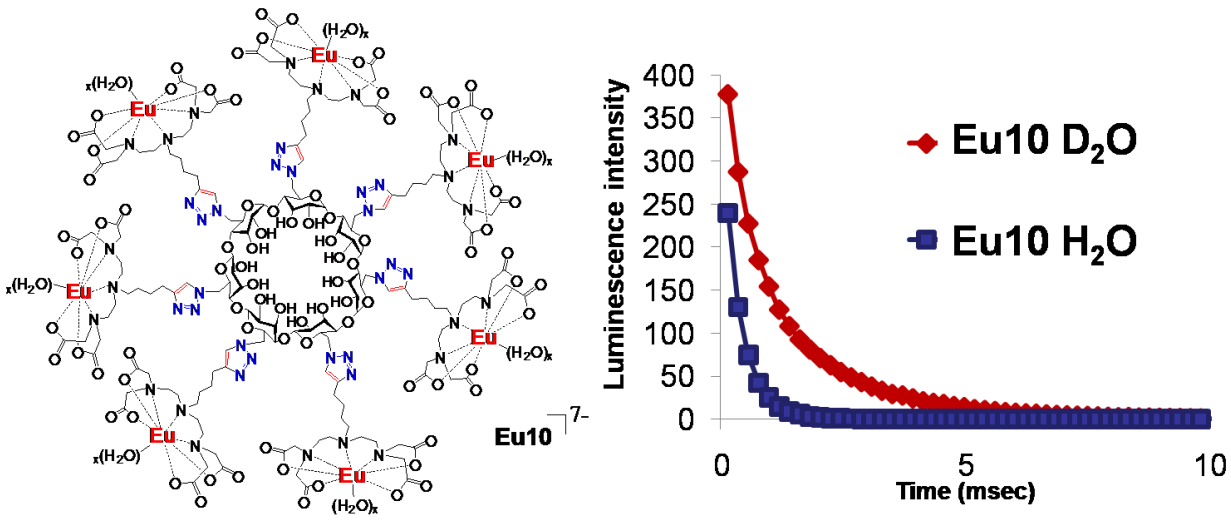

Figure 3-3. The structure of **Eu10** and the luminescence decay of said compound in H_2O and D_2O.

The relaxivity for **Gd10** was determined at a high magnetic field (9.4 T, 400 MHz, 37°C) by measuring the T_1 of several aqueous solutions and plotting $1/T_1$ versus concentration. As a control, the results were compared to Magnevist™ ($Gd\text{-}DTPA^{2-}$), a common clinically-approved contrast agent. As shown in Figure 3-4, at this high magnetic field, Magnevist™ has a relaxivity value of 3.2 mM^{-1} s^{-1}. However, the molecular relaxivity calculated for the entire **Gd10** cluster was found to be 43.4 mM^{-1} s^{-1}, which is an exceptionally high value. When we calculated the relaxivity value on a per Gd^{3+} basis for **Gd10**, it was found to be 6.2 mM^{-1} s^{-1}. This value represents a 94% increase in the relaxation efficiency over Magnevist at 9.4T and is likely related to the higher *q* value and larger molecular size that can increase the rotational correlation time (*10-13*). It should be noted that these values are predicted to be much higher at lower magnetic fields by the Solomon-Bloembergen-Morgan (SBM) equations (*1-4, 21*). To directly visualize the enhanced relaxivity for **Gd10** and potential for increasing resolution, we imaged 25 mL vials filled with Magnevist, **Gd10,** and water together on a Varian 4T human MRI scanner, keeping the gadolinium concentration constant, [Gd^{3+}] = 1.11 mM (Figure 1, inset). With respect

to water, Magnevist™ reveals a higher contrast, however, **Gd10** clearly reveals the brightest signal and highest contrast even at a low macromolecule concentration.

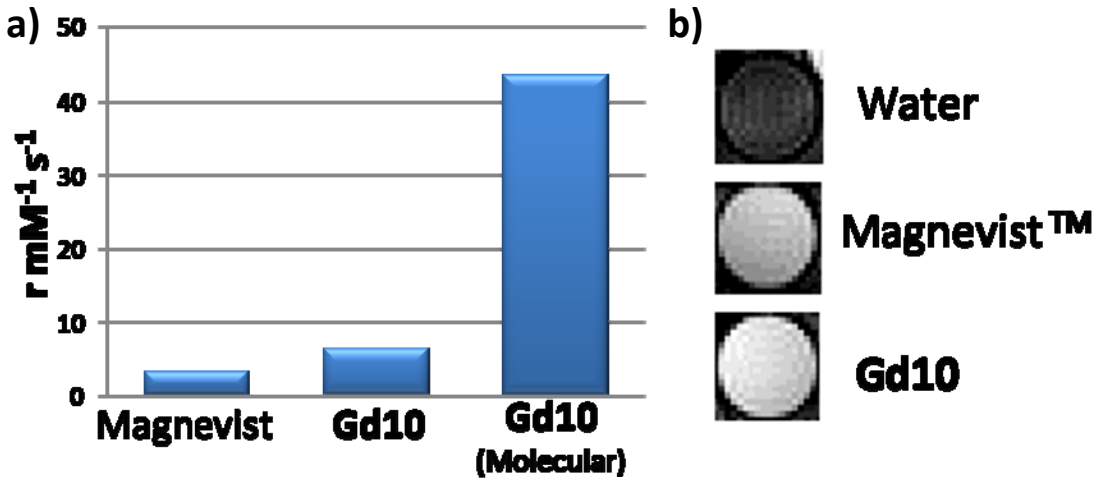

Figure 3-4. Relaxivity of Magnevist™ and Gd10. a) The bars reveal the relaxivities at 9.4 T. b) The inset images show the T_1-weighted MR images of water, Magnevist, and **Gd10** solutions acquired on a 4T MRI scanner.

3.5 Conclusions

In summary, the development of novel macromolecular contrast agents that offer enhanced relaxivity profiles at high magnetic fields have the potential to greatly improve the diagnosis, understanding, and treatment of disease. For this purpose, a novel β-cyclodextrin click cluster has been creatively endowed with seven paramagnetic arms that each contain two water exchange sites. This discrete paramagnetic agent yields an exceptionally high relaxivity profile (43.4 mM^{-1} s^{-1} at 9.4 T) and enhanced contrast on a human MRI scanner. Moreover, the useful inclusion properties exhibited by β-cyclodextrin also make this an excellent host scaffold to functionalize via non-covalent assembly with biological receptor-specific targeting moieties. Investigations are underway to study the limitless potential of this contrast agent for targeted MRI applications.

3.6 Acknowledgement

The author wishes to thank the co-authors that contributed to this work. Thanks Dr. Wen-Chu and Dr. Jing-Huei Lee for MR images. We also thank Kirk Lokits for ICPMS, Andrew Wolf for some synthetic studies, and Dr. Stephan Macha for ESI-MS acquisitions. This work was supported by the National Institutes of Health (1-R21-EB007244-01) and the Alfred P. Sloan Foundation.

3.7 References

1. Lauffer, R. B. *Chem. Rev.* **1987,** *87*, 901-927.
2. Tóth, É., Merbach, A. E., Helm, L. (2001) *Relaxivity of Gd(III) complexes: Theory and Mechanism*, Wiley, Chichester.
3. Caravan, P., Mcmurry, T. J., Lauffer, R. B. *Chem. Rev.* **1999**, *99*, 2293-2352.
4. Caravan, P. *Chem. Soc. Rev.* **2006**, *35*, 512-523.
5. Livramento, J. B., Helm, L., Sour, A., O'Neil, C., Merbach, A. E., Tóth, É. *Dalton Trans.* **2008**, *9*, 1195-1202.
6. Pierre, V. C., Botta, M., Aime, S., Raymond, K. N *J. Am. Chem. Soc.* **2006**, *128*, 9272-9273.
7. Tóth, É., Helm, L., Merbach, A. E. *Comprehensive Coordinate Chemistry II*, **2004**, *9*, 841-881.
8. Mohs, A. M., Lu, Z-R., *Expert Opin. Drug Deliv*, **2007**, *4*, 149-164.
9. Torchilin, V., Babich, J., Weissig, V. *J. Liposome Res.* **2000**, *10*, 483-499.
10. Mohs, A. M., Wang, X., Goodrich, K. C., Zong, Y., Parker, D. L., Lu, Z.-R., *Bioconjugate Chem.* **2004,** *15*, 1424-1430.
11. Langereis, S., Dirksen, A., Hackeng, T. M., Van Genderen, M. H. P., Meijer, E. W. *New J. Chem.* **2007,** *31*, 1152-1160.
12. Ranganathan, R. S., Fernandez, M. E., Kang, S. I., Nunn, A. D., Ratsep, P. C., Pillai, K. M. R., Zhang, X., Tweedle, M. F, **1998,** *33*, 779-797.
13. Srinivasachari, S., Fichter, K. M., Reineke, T. M. *J. Am. Chem. Soc.* **2008,** *130*, 4618-4627.
14. Bartlett, D. W., Davis, M.E. *Biotech. Bioeng*. **2008,** *99*, 975-985.

15. Bellocq, N. C., Pun, S. H., Jensen, G. S., Davis, M. E. *Bioconjugate Chem.* **2003,** *14*, 1122-1132.

16. Aime, S., Botta, M., Fedeli, F., Gianolio, E., Terreno, E., Anelli, P. *Chem.-Eur. J.* **2001**, *7*, 5261-5269.

17. Song, Y., Kohlmeir, E. K., Meade, T. J. *J. Am. Chem. Soc.* **2008**, *130*, 6662 – 6663.

18. Ruloff, R., van Koten, G., Merbach, A. E *Chem. Commun.* **2004**, *7*, 842-843.

19. Ruloff, R., Muller, R. N., Pubanz, D., and Merbach, A. E. *Inorg. Chim. Acta*, **1998**, *275*, 15-23.

20. Davies, J. S., and Al-Jamri, L. *J. Pept. Sci.* **2002**, *8*, 663-670.

21. Boger, J., Corcoran, R. J., Lehn, J.-M. *Helv. Chim. Acta* **1978,** *61*, 2190-2218.

22. Ashton, P. R., Gattuso, G., Ko¨niger, R., Stoddart, J. F., Williams, D. J. *J. Org. Chem.* **1996,** *61*, 9553-9555.

23. Rostovtsev, V. V., Green, L. G., Fokin, V. V., Sharpless, K. B. *Angew. Chem., Int. Ed.* **2002**, *41*, 2596-2599.

24. Mynar, J. L., Choi, T.-L., Yoshida, M., Kim, V., Hawker, C. J., Fréchet, J.M. J. *Chem. Commun.* **2005**, 5169-5171.

25. Johnson, D. A. *J. Chem. Ed.* **1980**, *57*, 475-476.

26. Supkowski, R. M., Horrocks, J., W. D. *Inorg. Chim. Acta* **2002**, *340*, 44-48.

27. Urbanczyk-Pearson, L. M., Fermia, F. J., Smith, J., Parigi, G., Duimstra, J. A., Eckermann, A. L., Luchinat, C., Meade, T. J. *Inorg. Chem*. **2008**, *47*, 56-68.

Chapter 4: Characterization of **Gd10** *in vivo* and *in vitro*

4.1 Abstract

MRI characterization has shown Heptakis{6-*N*-[(Gd(III)-diethylenetriamine-tetraaceticacid)butyl]-6-(1,2,3-triazole)} cyclomaltoheptaose (**Gd10)** to be a highly efficient contrast agent with interesting MR properties. **Gd10** was studied for toxicity *in vitro* in cardiomyoblast cells. Toxicity did occur, as it did in other clinically used contrast agents such as Magnevist™. Sprague-Dawley rats were given tail vein injections of **Gd10** (0.1 mmol/kg) and monitored via MRI for contrast agent bio-distribution and washout. No acute toxicity was observed in the rats studied (n = 2) and from image analysis, renal clearance is the primary route of elimination. In light of the negative *in vitro* data, further metal analysis in the organs is required to uncover any possible accumulation of **Gd10** in tissue.

4.2 Introduction

The great promise shown by **Gd10** as a contrast agent needed to be further evaluated to validate its potential.[1] For this reason, toxicity and imaging capabilities of this agent have been examined in both cells and rats. As described earlier in this work, contrast agents can impart significant diagnostic value in imaging. Shown below is an example of the enhancement imparted by Magnevist™ in full body images acquired in this study using the same conditions we describe *vide infra* for **Gd10** analysis. Figure 4-1a shows a typical MR image without the use

of contrast agent which was attained in one of the Sprague-Dawley rat subjects. The contrast in the image is due to the differences in proton relaxation rates in the lipophilic and hydrophilic tissues. Upon injection with Magnevist, the image demonstrates brightness in regions that were previously dark, especially vasculature and the kidneys.

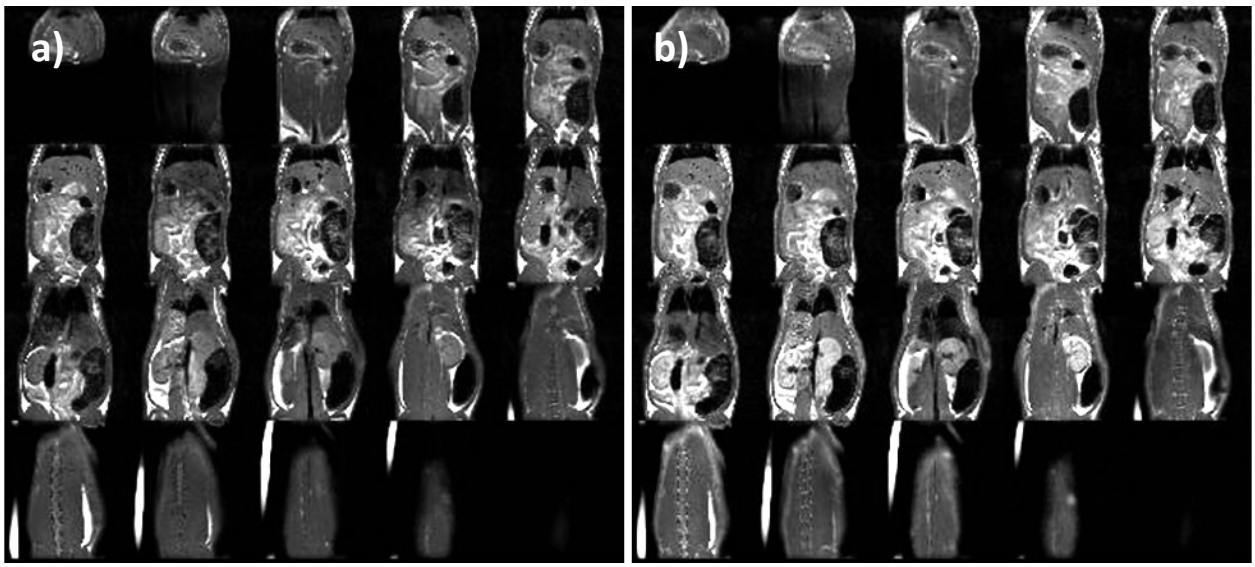

Figure 4-1. Magnevist induced contrast in rats. Image a) is the control rat with no contrast agent. Image b) is the same rat after injection 6 min after injection with Gd-DTPA contrast agent.

Previous work *in vitro* in polymeric and dendritic systems, has given a good indication of how a contrast agent will be cleared from a system.[2,3] Ideally, the contrast agent will stay in the system for a time period long enough to retain a high resolution image, but short enough to minimize distribution into tissue. The main factors in determining how quickly an agent will wash out are related to its size and charge. Typically molecules smaller than 5 nm, roughly the size of the renal pore, and that carry a negative or neutral charge will be eliminated via renal clearance and demonstrate lower tissue permeation.[4] Bretenbeich et al. demonstrated the clear

relationship between molecular weight and clearance times with PAMAM dendrimer contrast agents.[5-7] They found at higher dendrimer generations the blood pool retention was quite high, however clearance from the blood stream was handled primarily by hepatic routes, which can lead to complications and side effects. Based on previous work *in vivo* and our own analysis, we predicted that due to the size and charge profile of our molecules, clearance would happen via the kidneys with reasonable blood pool lifetimes.[8-12]

4.3 Materials and Methods

4.3.1 Materials

Media and supplements were purchased from Gibco/Invitrogen (Carlsbad, CA). HeLa cells were purchased from ATCC (Rockville, MD) and cultured according to specified conditions. Nuclease free water, Opti-MEM, and DMEM (supplemented with 10% fetal bovine serum (FBS), 100 units/mL penicillin, 100 μg/mL streptomycin, and 0.25 μg/mL amphotericin) and PBS were all purchased from Invitrogen (Carlsbad, CA). An Bio-Rad MTT assay kit used in the H9C2 cell viability assay was purchased from Bio-Rad (Hercules, CA).

4.3.2 MTT Assay

Twenty-four hours prior to treatment with **Gd10,** a rat cardiomyocyte cell line (H9C2) was seeded onto a 48-well plate at a density of 15k cells/well and incubated in supplemented DMEM (%10 FBS) at 37°C and 5 % CO_2. The DMEM in the wells was removed and treated in triplicate with various prepared solutions of **Gd10** dissolved in supplemented DMEM at various concentrations (1mM, 3mM, 5mM, and 10mM). The cells were then incubated at 37°C under a

5% CO_2 atmosphere for 4 hours (at the higher end of clearance time for contrast agents). Subsequently, the **Gd10** containing media was removed and replaced with 500 μl per well of a 0.5 mg/mL solution of 3-(4,5-dimethylthiazol-2-yl)-2,5-diphenyltetrazolium bromide (MTT) in DMEM and allowed to incubate for an additional hour. After an hour, each well was evacuated of medium and washed with PBS. Following PBS removal, each well was treated with 300μl of DMSO and colorimetrically assayed for UV-vis absorption on a plate reader at 570 nm. Results were standardized to control absorbencies to calculate toxicity.

4.3.3 Gd10 Effect on Cell Morphology

Twenty-four hours prior to treatment with **Gd10,** H9C2 cells were seeded onto a 48-well plate at a density of 15k cells/well and incubated in supplemented DMEM (%10 FBS) at 37°C and 5 % CO_2. The wells were evacuated of DMEM and treated in triplicate with various prepared solutions of **Gd10** dissolved in supplemented DMEM at various concentrations (1mM, 3mM, 5mM, and 10mM). The cells were then incubated at 37°C under a 5% CO_2 atmosphere for 4 hours and visualized on a Nikon TE 2000 inverted epifluorescence microscope, equipped with a CoolSnap HQ CCD camera. Images were recorded for each **Gd10** concentration of 0, 1, 5, and 10 mM.

4.3.4 Animal Handling Protocol

Male Sprague-Dawley rats were purchased, fed, and stored in accordance with NIH guidelines. All procedures were performed under anesthesia (5% isoflurane). Anesthesia was maintained in the magnet and radiofrequency coil using a special, close-fitted nose cone and administered via air delivery of 2.5 % isoflurane. The rat's body was placed inside the coil and held steady using tape. Ointment was placed in the eyes and the rat was fitted with a device to

monitor its respiration rate and temperature. The animal's temperature, as well as the magnetic bore temperature, were regulated via a special stage permitting the circulation of 37^{o}C water. After the stage was positioned within the magnetic bore, simple scans were acquired to check the location of the rat within the instrument. At this point, rats were dosed (0.1 mmol/kg) with the appropriate contrast agent (**Gd10**, Magnevist), via tail-vein injection, and subjected to multiple scans to determine bio-distribution and kinetics.

4.3.5 MRI pulse sequence optimization

Rats were placed in the coil to optimize pulse sequence based on time. Slice optimization was carried out using RARE sagittol and coronal T_2 scans. The images were acquired using a FLASH sequence with centric encoding. Acquisition parameters are as follows: TR (repetition time) = 31.47 msec, TE (echo time) = 3.606 msec, flip angle = 30 degrees. Total time required for one acquisition was 3 min. Pulsing was synchronized with the rat's breathing rate to minimize image distortions. Image contrast was adjusted relative to the controls.

4.3.5 MRI analysis

Upon completion of rat full body montage images, all image processing was carried out in Image-J software. Images were processed in 8-bit grayscale mode and normalized to the intensity of an internal contrast agent standard (Magnevist^{TM} 0.1mM in NMR tube). A specific slice was chosen from the rat's full body array scan that contained portions of the renal medulla, the renal cortex, the liver, the bladder, the inferior vena cava, and lipid. Specific pixels were chosen in each of these organs to be representative of organ contrast intensity as shown in Figure 4-4. These pixels were analyzed for each image in the rat's profile over an hour period and used as a way of determining contrast agent washout and regional enhancement.

4.4 Results and Discussion

4.4.1 *In vitro* data

In vitro studies are not ideal to determine the behavior and toxic effects from contrast agents, which are largely extracellular entities and are cleared from the blood with short half lives via renal clearance. However, **Gd10** was evaluated in cell culture to seek information before animal studies were carried out. The results from the MTT assay suggest that **Gd10** does exhibit toxicity to cardiomyocytes cells *in vitro*. This could likely be for several reasons. First, though not studied for **Gd10**, β-cyclodextrin is known to abstract cholesterol from cellular walls, which decreases membrane integrity, ultimately leading to apoptosis.[13,14] This could possibly be an issue that results in toxicity, especially in cell culture. Likely this accounts for the fact that **Gd10** exhibits higher toxicity than Magnevist™ within its effective dose therapeutic window (Figure 4-2). Another important factor that could explain toxicity would be that cells are exposed **Gd10** for long enough that contrast agent is possibly entering the cells through active uptake pathways and initiating a toxic response. Finally, **Gd10** is an anionically charged molecule and could sequester Ca(II) anions from culture media, eliciting a toxic response.

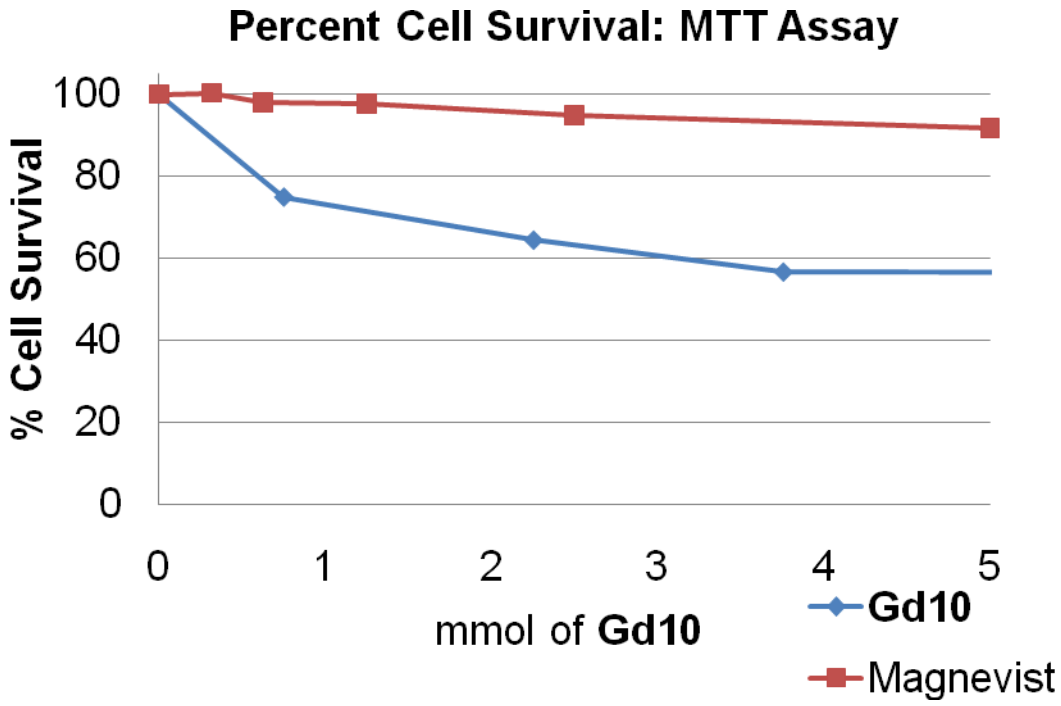

Figure 4-2. Results of MTT assay show increased toxicity in H9C2 cells as a function **Gd10** concentration.

Cell morphology after dosing with **Gd10** also indicates that the H9C2 cells have displayed a toxic response. Healthy H9C2 have a spread-out and elongated morphology. When these cells die, they condense into a spherical morphology and become detached from the flask's surface. Figure 4-2 indicates that as the dose of **Gd10** is increased within its therapeutic window, it initiates cytotoxity after a four hour time period. Cell morphology changes are certainly noticeable at lower concentrations and are highly pronounced at greater concentrations, with cell debris strewn throughout the image (Figure 4-3). H9C2 are extremely sensitive compared with other immortalized cell lines, and for this reason also, it is not a great surprise that they show a higher toxic response in both the *in vitro* MTT assay and the cell morphology microscopy images.

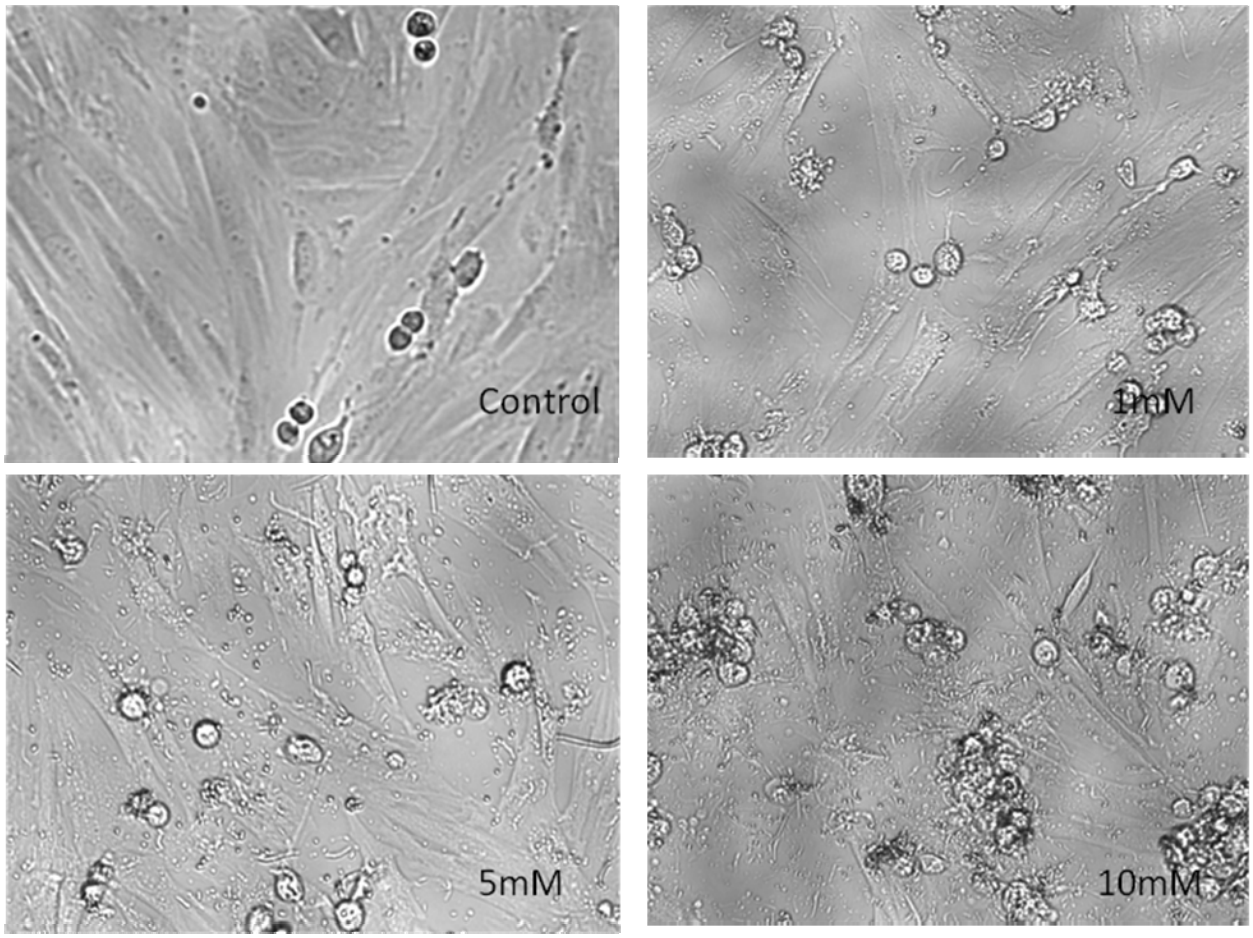

Figure 4-3. H9C2 cells treated with various concentrations of **Gd10** for four hours and visualized using an inverted wide field microscope to study their morphology. Healthy H9C2 cells have elongated structures. Dying cells have a spherical morphology and detach from the surface of the culture plate.

4.4.2 *In vivo* data

To get a preliminary idea of how **Gd10** would be tolerated in animals, studies were performed in rat models. Anesthetized Sprague-Dawley rats were given tail vein injections (0.1mmol/kg) of **Gd10** and evaluated for their ability to tolerate the agent and imaged to determine the clinical efficacy and washout rate/pathway of this agent. Using a FLASH pulse

sequence compensated for breathing movement, rats were imaged in 3 minute intervals over a total period of one hour. Full body profile images were generated at each time point and show excellent contrast enhancement upon injection, with illumination of the kidneys after 3 minutes. Image analysis of an organ inclusive slice (Figure 4-4), was performed to determine the primary pathway of washout, as shown in figures Figure 4-5 and Figure 4-6.

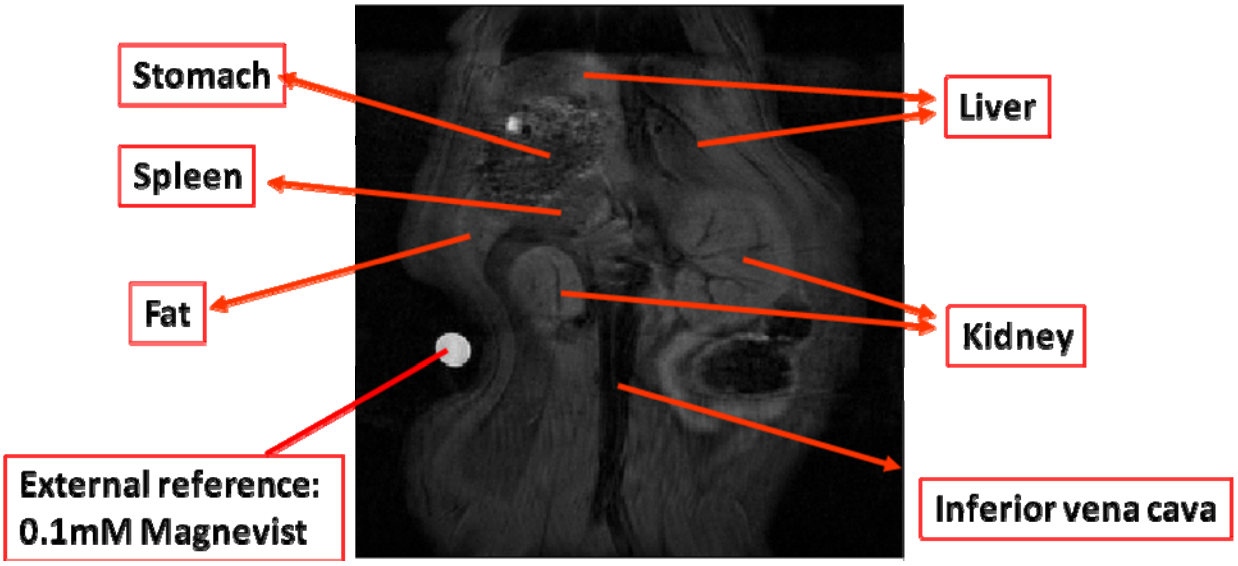

Figure 4-4. The image slice shown above contains several organs possibly involved in **Gd10** washout making it an ideal slice for image analysis.

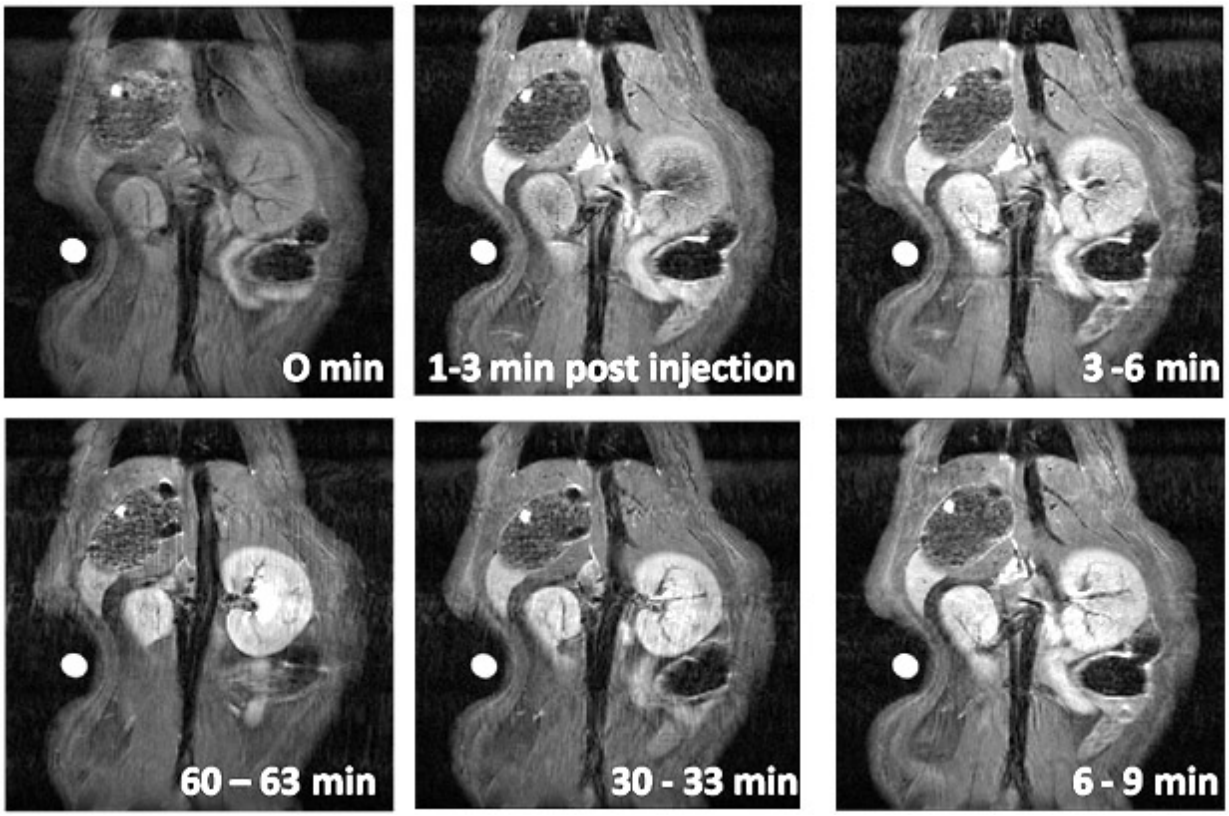

Figure 4-5. Images used for washout analysis. It is clear from the above time frame that the main route of clearance from the blood stream is through the kidneys. The white dot in the lower right quadrant of each image is an nmr tube filled with 0.1 mM magnevist for external referencing.

It is clear from Figure 4-5 that **Gd10** rapidly washes out of the blood pool, though this particular pulse sequence is not ideal for visualizing the blood pool. After 9 minutes it seems that the kidney on the right side, which this slice goes through, is fully permeated, with the medulla of this kidney continuing to brighten up to 33 minutes (figure 4-6). **Gd10** is sized (5.52 nm) towards the upper size constraints of the renal pore (~5 nm), which adds to its blood pool retention. Because of this long retention and bright signal, **Gd10** could be especially useful in applications requiring longer blood retention, which can be tricky and particularly dangerous to evaluate using small molecule contrast agents.[15] All of the other tissues observed here show

contrast enhancement as well. Most of these tissues immediately take up **Gd10** and continue to give an enhanced signal for the 60 minute period of this study. Enhancement in lipid tissue was of particular interest due to its uncharacteristic uptake of contrast agent. We think the hydrophobic cup contained by **Gd10** could be interacting with the hydrophobic surfaces of these tissues and promoting contrast there due to their locale. The fact that some enhancement was noted in the liver was of concern to us, since others have noted this to cause complication,[7] however no toxicity was observed in the animal studies, even two weeks after the conclusion of the study. Further analysis, especially metal analysis in organs and in urine, is necessary to make further conclusions about the bio-distribution and possible chronic damage caused by **Gd10** which has become somewhat of an issue in smaller contrast agents at high doses in people with nephrological disorders.[15]

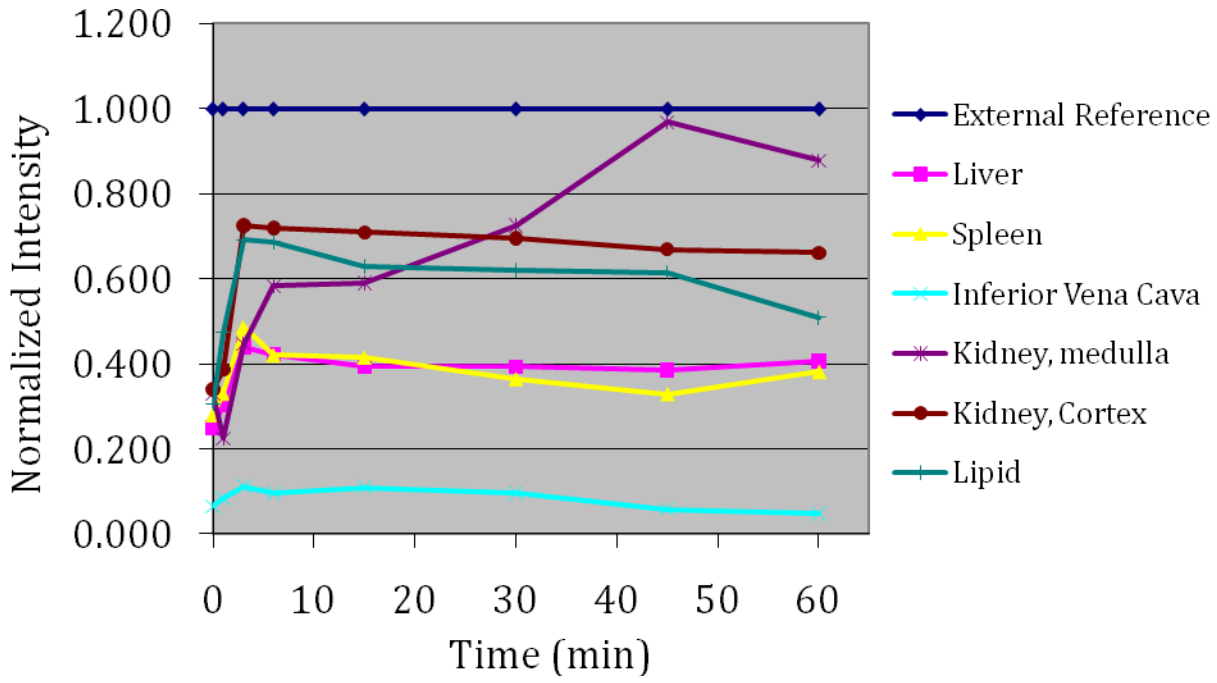

Figure 4-6. Plot shows the results of pixel analysis of rat organs to monitor washout of **Gd10**.

4.5 Conclusions

Gd10 has demonstrated to be a good contrast agent when studied in the test tube. In H9C2 cells, **Gd10** shows a toxic effect. This effect is likely due to several effects from **Gd10** including: membrane damage via hydrophobic leaching from the cyclodextrin core, Ca(II) sequestering, and possible Gd(III) release. This effect is also clear from cell morphology observations 4 h after treatment with **Gd10**. *In* vivo, no animal deaths (n = 9) or adverse reactions occurred of the period of study (2 weeks). Rats showed excellent washout profiles via image analysis, but further studies, such as organ and urine analysis, are required to elucidate the washout mechanism. Images showed that **Gd10** could be useful in monitoring hydrophilic tissues for clinical use, especially in applications where small fast-clearing contrast agents are not suitable. These cases require high renal contrast with lower Gd(III) dosing, which is ssential in patients in all stages of kidney failure.

4.6 Acknowledgement

The author would like to acknowledge NIH for funding this project and the center for animal imaging at Children's Hospital in Cincinnati Ohio for their expertise in animal handling and operating the 9.4 T MRI. Also thanks to Dr. Lee and Dr. Chu for their expertise in pulse sequences and animal imaging.

4.6 References

1. Bryson, J. M.; Chu, W. –J.; Lee, J. –H.; Reineke, T. M. *Bioconjugate Chem.* **2008**, *19*, 1505 – 1509.

2. Davis, M. E.; Chen, Z.; Shin, D. M.; *Nat. Rev. Drug Discovery* **2008,** *7*, 771 - 782.

3. Siauve, N.; Clément, O.; Cuénod, A.; Benderbous, S.; Frija, G. *Magn. Res. Imag.* **1996**, *14*, 381 – 390.

4. Helbich, T. H.; Gossman, A.; Mareski, P. A.; Radüchel, B.; Roberts, T. P. L.; Shames, D. M.; Mühler, M.; Turetschek; Brasch, R. C. *J. Magn. Res. Imaging* **2000**, *11*, 694 – 701.

5. Wiener, E. C.; Auteri, F. P.; Chen, J. W.; Brechbiel, M. W.; Gansow, O. A.; Scheider, D. S.; Belford, R. L.; Clarkson, R. B.; Lauterbur, P. C. *J. Am. Chem. Soc.* **1996**, *118*, 7774 – 7782.

6. Kobayashi, H.; Kawamoto, S.; Jo, S. –K.; Bryant, H. L.; Brechbiel, M. W.; Star, R. A. *Bioconjugate Chem.* **2003**, *14*, 388 – 394.

7. Kobayashi, H.; Brechbiel, M. W. *Mol. Imaging* **2003**, *2*, 1 – 10.

8. Daldrup-Link, H. E.; Shames, D. M.; Wendland, M.; Muhler, A.; Gossman, A.; Rosenau, W.; Brasch, R. C. *Acad. Radiol.* **2000**, *7*, 934 – 944.

9. Kim, Y. H.; Choi, B. I.; Cho, W. H.; Lim, S.; Moon, W. K.; Han, J. K.; Weinmann, H. –J.; Chang, K. –H *Invest. Rad.* **2003**, *38*, 539 – 549.

10. Misselwitz, B.; Schmidt-Willich, H.; Michaelis, M.; Oellinger, J. J. *Invest. Rad.* **2002**, *37*, 146 -151.

11. Fink, C.; Ley, S.; Puderbach, M.; Plathow, C.; Bock, M.; Kauczor, H. –U *Eur. Radiol.* **2004**, *14*, 1291 – 1296.

12. Krombach, G. A.; Higgins, C. B.; Chujo, M.; Saeed, M.; *Radiology* **2005**, *236*, 510 - 518.

13. Ulloth, J. E; Almaguel, F. G; Padilla, A.; Bu, L.; Liu, J. W.; Leon, M. D. *Neurotoxicology* **2007**, *28*, 613 – 621.

14. Boulmedarat, L.; Bochot, A.; Lesieur, S.; Fattal, E. *J. Pharm. Sci.* **2005**, *94*, 1300 – 1309.

15. Cowper, S. E.; Robin, H. S.; Steinberg, S. M.; Su, L. D.; Gupta, S.; LeBoit, P. E. *Lancet* **2001**, *356*, 1000–1001.

Chapter 5: Inclusion Mediated Self-Assembling Properties β-Cyclodextrin Based MRI Contrast Agents

5.1 Abstract

Adamantaneacetamidenonadodecane (**AD19**) has been synthesized to probe the inclusion and self assembling properties of Heptakis{6-*N*-[(Gd(III)-diethylenetriamine-tetraaceticacid)butyl]-6-(1,2,3-triazole)} cyclomaltoheptaose (**Gd10)** when coupled with large hydrophobic moieties. When formulated with **Gd10**, **AD19** initiates self-assembly in aqueous solutions, which is confirmed with dynamic light scattering and transmission electron microscopy. Sizes for self-assembled aggregates at lower concentrations (< 0.1mg/ml) are between 100 – 200 nm and are stable for up to six hours. At higher concentrations (> 0.1 mg/ml) higher-order rod shaped aggregates are observed with TEM. The specific morphology of these self-assembled complexes is not particularly clear from the techniques carried out, but based on the aggregate sizes, the morphologies are likely higher order multi-lamellar structures. Molecular modeling of **Gd10** and inclusion complexes using the PM3 molecular mechanics method confirms **Gd10** has the required structure to form inclusion complexes with **AD19**.

5.2 Introduction

Self-assembling materials are integral in the structure and function of biological systems. For this reason, these materials have been of great interest to the scientific community because of their potential biocompatibility, ability to carry hydrophobic drugs in biological systems and

across cell membranes and their prolonged blood pool retention due to the size imparted by self assembly. **Gd10** (introduced in chapter 3) displays some of the very interesting inclusion properties associated with other cyclodextrin-based molecules. Here, we are interested in demonstrating that this inclusion property can be utilized to make supramolecular assemblies that benefit from the properties mentioned above, as well as other contrast agent specific benefits (*vide infra).*

Numerous groups have studied the influence of amphiphilic behavior exhibited in modified or included cyclodextrins. Zemb and coworkers published several articles demonstrating cholesterol conjugated β-cyclodextrins, their self assembly with each other, and what extraneous factors, such as solvent and concentration, effect assembly.[1,2] Stephen Craig and coworkers showed that PEG linked adamantane is complexed by hydrophobically-modified cyclodextrins and causes their self assembly.[3] This system assembled to form both spheres and rods depending on concentration. Zhang and coworkers explored a similar system using a trans-azobenzene photo-isomerizing hydrophobic inclusion group, which forms the *cis* conformer after irradiation.[4] The *cis* conformer will not include in α-cyclodextrin, but the *trans* confirmer will, essentially giving a photo-initiated self-assembling system. Jiang and coworkers have demonstrated inclusion mediated self assembly between their poly-adamantanyl acrylate and poly-cyclodextrin polymer blends.[5] Finally, using smaller inclusion groups, Wu *et al.* formed micrometer length self-assembled rods exclusively from β-cyclodextrins.[6]

Several recent reports have touted the success of self assembled contrast agents, which have been shown to greatly improve contrast properties and are able to carry hydrophobic drugs in their hydrophobic cores. Yokoyama and coworkers developed polymeric micelle contrast agents that went selectively into tumors and unraveled to provide high contrast in tumor regions.[7]

Surprisingly, the self-assembled chelates showed lower relaxivity than the free chelates, likely because the water exchange site was blocked. Morelli and coworkers tethered Gd-DTPA to hydrophobic blocks, yielding an amphiphilic molecule, which self-assembled in water and formed micelle-like structures in which the Gd-DTPA protruded out from the hydrophobic core. These systems were characterized via relaxivity as a function of aggregate size (from DLS and TEM). They saw large enhancements in relaxivity compared to the unassembled controls.[8] Further studies in similar systems have lead to some interesting mixed aggregate micelles and have revealed fundamental structure property relationships.[9-12]

Heptakis{6-*N*-[(Gd(III)-diethylenetriamine-tetraaceticacid)butyl]-6-(1,2,3-triazole)} cyclomaltoheptaose has proven to be a valuable contrast tool and to be non-toxic in animals, in previous studies,[13,14] however little study has gone into studying one of the most unique features about **Gd10**, the inclusion capabilities. Here we demonstrate with molecular mechanics calculations and experimental characterization that **Gd10** can include and self-assemble with hydrophobic moieties such as **Ad19**.

5.3 Materials and Methods

5.3.1 Materials

Gd10 was synthesized according to procedures outlined in Chapter 3. All other chemicals unless specified otherwise were purchased from Alfa Aeser Chemical Co. (Boston, MA) and were used without further purification. Nonadecylamine was purchased from TCI chemicals (Tokyo, Japan). NMR spectra were collected on a Bruker AV-400MHz spectrometer. ^{1}H NMR data are reported as follows: chemical shift (δ ppm), multiplicity (s = singlet, d =

doublet, t = triplet, q = quartet, m = multiplet, bs = broad singlet), and the peak integration. Mass spectra were obtained with an IonSpec ESI mass spectrometer in positive ion mode. IR spectra were measured on a Perkins-Elmer IR spectrometer with ATR attachment. Relaxivity measurements were carried out on a Varian UNITY 400MHz and an Anasazi 60 MHz NMR spectrometer. TEM grids were obtained from Electron Microscopy Sciences (Hatfield, PA).

5.3.2 Synthesis

Preparation of Adamantylacetyl Chloride, (1). Adamantane acetic acid (1.0 g, 5.2 mmol) was dissolved in 10 ml of dry CH_2Cl_2 and cooled to 0^o C under N_2. Oxalyl chloride (1.9 g, 15 mmol) was added via syringe to the stirring solution of adamantane acetic acid. After allowing the mixture to re-cool to 0^o C, one drop of dry DMF was added to the mixture which was followed by vigorous gas liberation that continued for 10 min. After gas evolution ended, the reaction mixture was warmed to room temperature and allowed to react an additional hour during which some solid byproducts appeared to form. The reaction mixture was then filtered and rotovapped to yield a clear oil: the product. Yield = 743 mg, 67.5%. ^{1}H-NMR ($CDCl_3$) δ = 1.65 – 1.80 (bm, 12H), 2.01 (s, 3H), 2.12 (s, 2H). ^{13}C-NMR ($CDCl_3$) δ = 28.6, 33.2, 34.1, 36.6, 42.1, 44.8 48.7, 160.4.

Preparation of nonadecanyl-adamantylamide, (2). Aminononadecane (226 mg, 0.799 mmol) was dissolved in 5 ml of dry CH_2Cl_2 and dry triethylamine (161 mg, 1.6 mmol). Under stirring and in a N_2 environment, the reaction mixture was cooled to 0^o C. Adamantane acetyl chloride (170 mg, 0.799 mmol) in 5 ml of dry CH_2Cl_2 was added dropwise to the reaction mixture over a 5 min period with heat generation and precipitant formation. Reaction was allowed to proceed

for 1 h and then poured into a separation funnel, washed with pH = 5 HCl/water (2 x 20ml), ultrapure water (2 x 20ml), and dried over Na_2SO_4. The CH_2Cl_2 was removed via rotary evaporation to yield a white waxy substance, which was subjected to silica column purification using CH_2Cl_2 as the mobile phase. Compound **2** was recovered as a white solid. Yield = 220 mg, 55.6 %. ^{1}H-NMR ($CDCl_3$) δ = 0.87 (t, 3H), 1.24 (bs, 36H), 1.45 (q, 2H) 1.65 (bm, 14H) 1.89 (s, 2H), 1.96 (bs, 3H)**.** ^{13}C-NMR ($CDCl_3$) δ = 19.2, 22.3, 24.2, 28.6, 29.3, 29.5, 29.7, 31.2, 32.6, 34.2, 34.4, 35.3, 39.4, 41.4, 44.8 49.2, 57.2, 157.5. ESI-MS (m/z): Theoretical $(M + H)^+$ = 460.4513; Actual $(M + H)^+$ = 460.4528. MP = 65° C. FTIR (cm^{-1}): 3317.2, 1639.5, 719.3.

5.3.3 Preparation of Gd10 self-assembled structures.

Preparation conditions for self-assembled **Gd10** were based upon conditions developed by Jiang and coworkers.[5] To prepare the self-assembled structures, stock solutions of both host (**Gd10**) and guest (**2**) were prepared. **Gd10** was dissolved in ultrapure water (10 mg/ml) and **2** was dissolved in 1:1 mixture of DMF/$CHCl_3$ (10 mg/ml). With DMF as a co-solvent, $CHCl_3$ and H_2O are fully miscible. The stock solutions were mixed together and vortexed for 30 sec. This mixture was then added dropwise to ultrapure water, under sonication, to obtain the following final concentrations of **Gd10**: 0.001 mg/ml, 0.01 mg/ml, 0.1mg/ml, 0.5 mg/ml, 0.9 mg/ml, and 4mg/ml.

5.3.4 Dynamic Light Scattering of Self-Assembled Structures.

The solutions of self-assembled structures were studied by dynamic light scattering to determine their hydrodynamic radii (R_h). Sizes were measured using a 633nm laser using a Zetasizer (Nano ZS) dynamic light scattering instrument (Malvern Instruments, Malvern, UK).

The measurements were carried out at 25ºC with a detection angle of 173º using a multimodal algorithm to calculate particle size(s).

5.3.5 Transmission Electron Microscopy

As a means of studying the structural morphology of the self-assembled structures, transmission electron microscopy (TEM), was performed. Each self-assembled solution was deposited (10 μl) onto a 400 mesh glassy carbon on copper grid and blotted off after a few seconds. Subsequently, the sample was stained with 10 μl of uranyl acetate and blotted dry. TEM was performed on a Phillips EM420 using a 120 kV electron beam.

5.3.6 Obtaining Proton Relaxation Rate Enhancement Constants (R_1)

T_1 measurements were carried out on Varian UNITY 400MHz (9.4T) and Anasazi FT-NMR 60MHz (1.41T) NMR spectrometers. **Gd10** aggregates were formed as described above, such that the concentration of Gd^{3+} was 1mM. After an incubation time of 5 min, the longitudinal relaxation time (T_1) for each solution was measured using an inversion recovery pulse sequence (180° – d_t – 90° – acquire) at 298K. Arrayed data [n(d_t) = 10] was processed using Acorn NUTS software and fit to a three-parameter model. The inverse of the T_1 data was used to determine the longitudinal relaxation rate constants (R_1) imparted by the aggregates and the free **Gd10**.

5.3.7 PM3 geometry optimization calculations for Gd10 models

Models of unchelated **Gd10** with the chelate acetic acid groups removed, i.e. Heptakis{6-*N*-[diethylenetriamine)butyl]-6-(1,2,3-triazole)} cyclomaltoheptaose, were modelled in Scigress software (Fujitsu Biosciences, Beaverton, OR). Structural peices, such as the pendant arms and

the cyclodextrin core, were optimized as seperate molecules using molecular mechanics (MM3). Optimized moities were bonded together and the full molecule was reoptimized using a higher level molecular mechanics calculation method (PM3). Because of the low accuracy of these types of calculations, results were only used to visualize final structures and not to quantify compounds **2** binding in the **Gd10** cavity.

5.4 Results and Discussion

After being inspired by the wealth of β-cyclodextrin self-assembly literature,[1-6] we set off to find out if **Gd10** would form self-assembled aggregates, to try and understand the fundamental conditions that affected this formation, and finally to find out if these aggregates could be beneficial for MRI related applications. The ultimate goal here is to make stable aggregates with controllable sizes, which could be used to promote blood pool retention and tumor uptake of contrast enhancing media, due to the EPR effect. Realizing that in comparison to lower molecular weight amphiphiles **Gd10** would make an extremely large head group, it was necessary to try and choose a hydrophobic tail group that would also be large. We chose a strategy of coupling the sterically bulky adamantane group with a hydrophobic tail using an acid chloride amine coupling reaction (Scheme 1), due to the high yields and good efficiency associated with these couplings. The acid chloride conversion happened quickly and was verified by the shift in its α proton NMR resonance from 2.72 ppm, for the acid, to 2.12 ppm for the acid chloride. The largest aliphatic primary amine that was commercially available was aminononadecane, which was coupled to adamantyl acetyl chloride. After column purification, formation of product **2** was noted from signature amide IR absorbencies (N-H stretch = 3317.2

cm^{-1}, C-O stretch = 1639.5 cm^{-1}, and N-H wag = 719.3 cm^{-1}) and further confirmed with NMR and ESI-MS (see Materials and Methods and Appendix A).

Scheme 5-1[a]

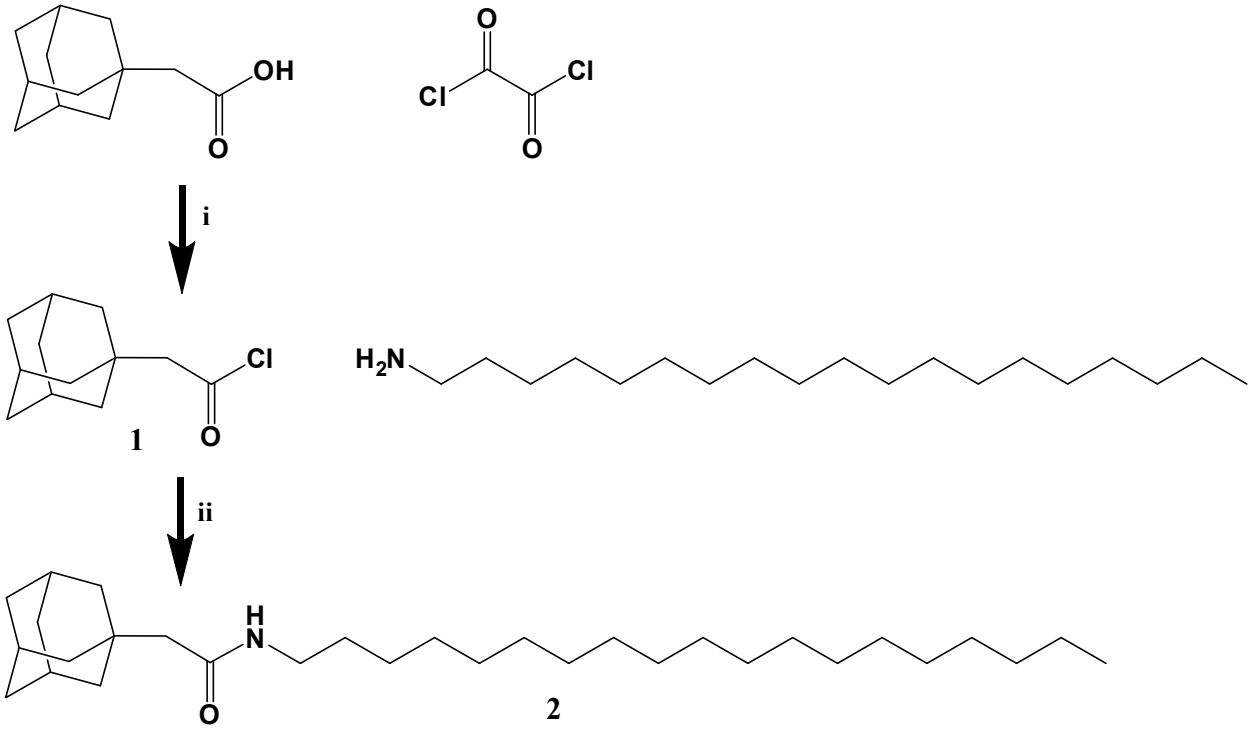

[a] **i**) CH_2Cl_2, $DMF_{(cat.)}$ **ii**) Triethylamine, CH_2Cl_2.

Because of the solubility differences between the very hydrophilic **Gd10** and **2**, which is very hydrophobic, it was necessary to choose solvents that were miscible with each other, but also solvents that would dissolve each compound. To initiate self assembly, **Gd10** was dissolved in water and titrated with compound **2** (which was dissolved in a 1:1 mixture of CH_2Cl_2 and DMF). Upon combining, **2** began to include into the cup of **Gd10** (Figure 5-1b). These miscible solutions were then mixed and added dropwise to various volumes of water under sonication, which promotes self assembly into supramolecular aggregates, as shown in Figure 5-1c. This process yielded several final sample concentrations that were then further studied by particle

sizing techniques such as dynamic light scattering (DLS) and transmission electron microscopy (TEM)

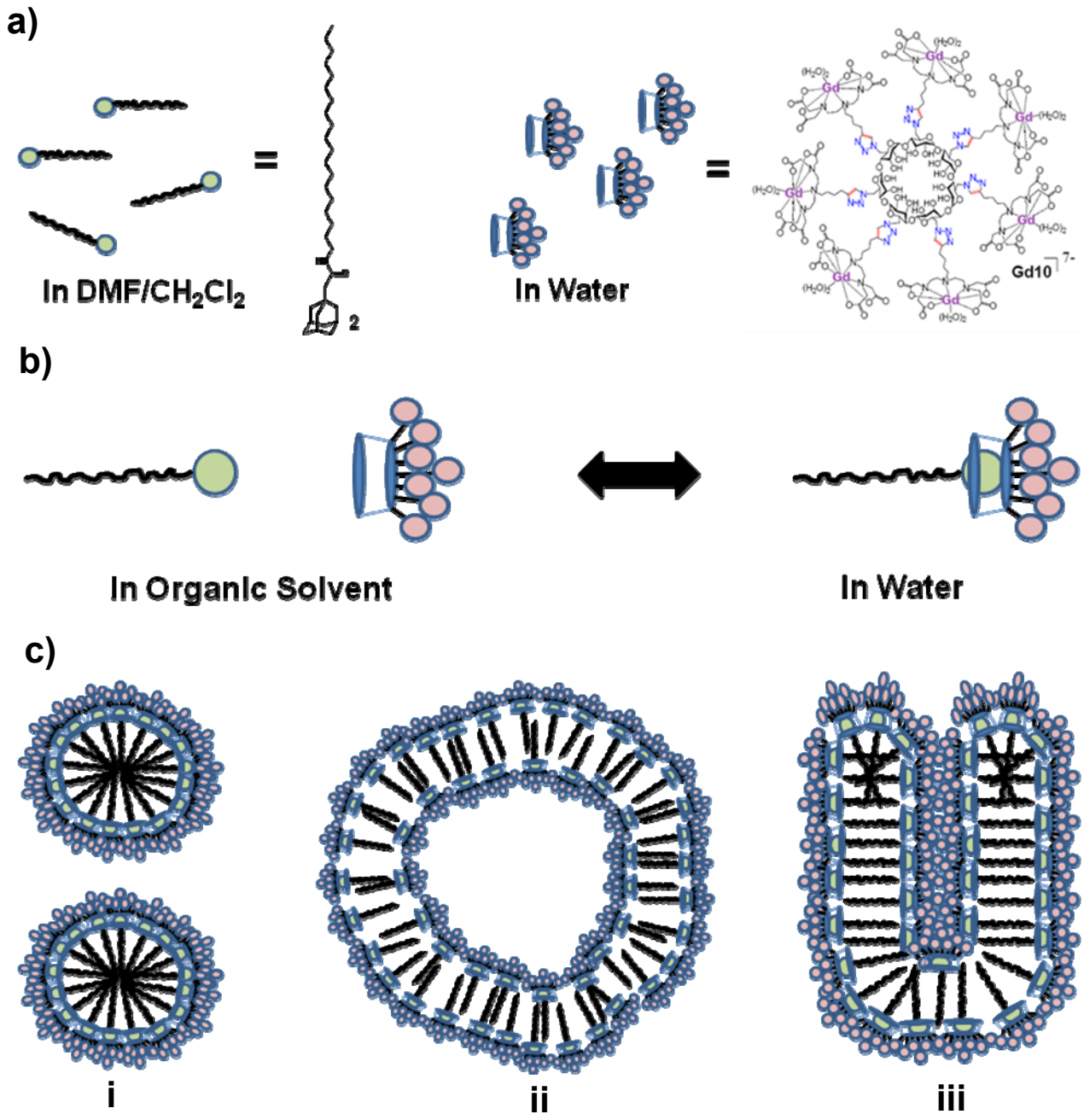

Figure 5-1. a) Schematic representation of **2** and **Gd10**. **b)** Scheme showing the inclusion of guest **2** into host **Gd10**. **c) i)** Micelles, **ii)** liposomes, and **iii)** higher order multi-lamellar structures, are all possible supramolecular aggregates that can form upon mixing solutions of **2** and **Gd10** in water.

After forming the supramolecular aggregates in solution, they were evaluated by DLS to try and understand the relationship between their size and formulation conditions. Particles were formed at a variety of concentrations from 0.001 mg/ml to 10 mg/ml, in water, phosphate buffered saline (PBS), and serum containing media. Size does not change over the concentration range from 0.001 mg/ml – 0.01 mg/ml in water and PBS, though there is a statistical difference in the sizes of particles formed at 0.001 mg/ml and 0.1 mg/ml, in which aggregate size seems to increase as a function of concentration in both water and PBS buffer (Figure 2a). There seems to be a similar trend in serum containing media, however large error is observed in the non-concentrated samples due to light scattering interference from serum proteins. Aggregates on the size order of microns were noted at concentrations of 0.50 mg/ml and higher. Later, we discovered, with the help of TEM, the higher order aggregates we were detecting with DLS are non-spherical, which can make DLS less reliable due to the complex non-linear algorithms required to interpret this scattering.[15] Micelle stability in water was also monitored using DLS. Particle size was compared at 5 min, 90 min, and 300 min, with no significant difference in particle size vs. time (Figure 5-2b).

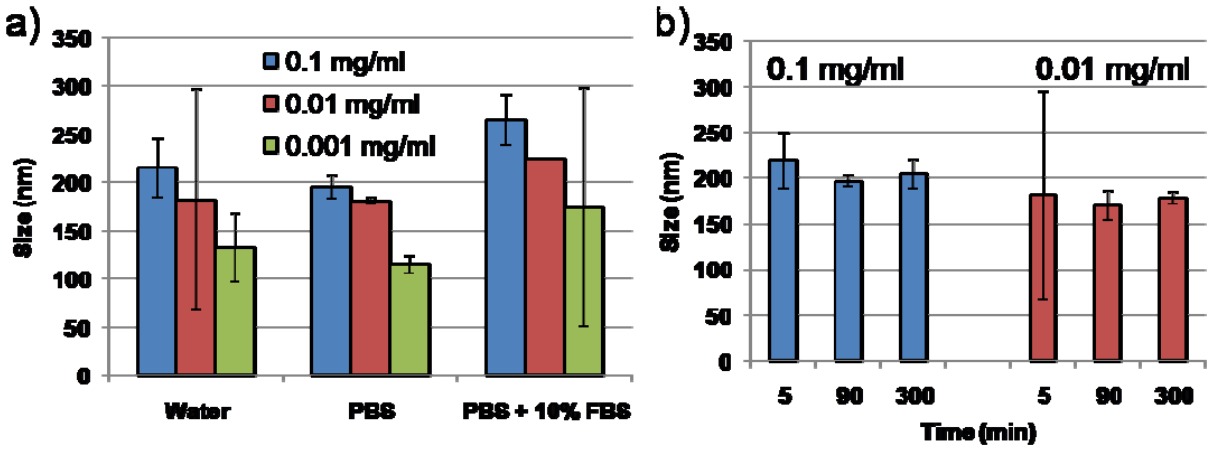

Figure 5-2. a) Graph denoting size of self-assembled aggregates as a function of buffer (150 mM phosphate-buffered NaCl. Particle size was taken in triplicate 5 min after particle formation. b) Particle size in water as a function of time taken in triplicate on 3 seperately made samples. Error bars represent a standard deviation in each direction.

In an attempt to further study the morphology of the self assembled complexes, TEM was performed. Aggregates were formed using the same procedure described in the Materials and Methods section and deposited on TEM grids with uranyl acetate as a stain. Ideally, since we are looking at solution structures, this work would be carried out on some type of cryogenic scope, however due to lack of access, more conventional methods were utilized. Also, the melting point of **2** is well above room temperature, so even though aggregates might change in size, they will likely retain resemblance of their solution shape. Lower concentration aggregate solutions show clusters of small (< 50 nm) spherical particles, that when aggregated, are larger than 100 nm. It seems at concentrations greater than 0.1 mg/ml that rods begin to appear, along with aggregates of smaller spheres. The size of the rods also seems to change as a function of concentration (Figure 5-3). This interesting morphological change was curious at first, but indeed others have observed similar behavior in related systems.[3] Future experiments should involve trying to understand these systems using better solution nanoscale imaging such as cryo-TEM and freeze-

fracture-SEM, to study the possibility and morphology of multi-lamellar structures being formed using techniques such as small-angle x-ray scattering (SAXS).

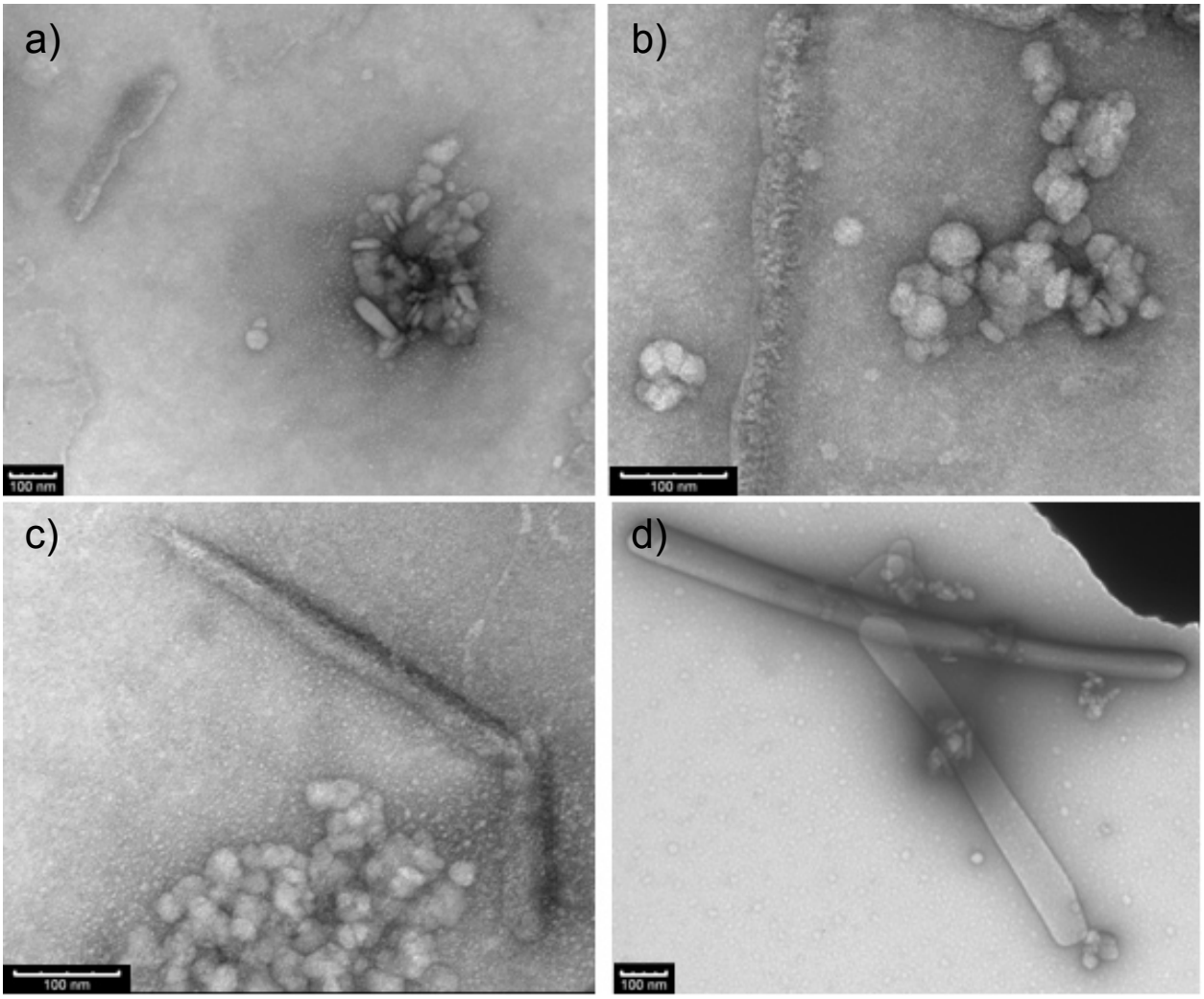

Figure 5-3. TEM micrographs of self-assembled aggregates prepared at various concentrations: a) 0.1 mg/ml, b) 0.4 mg/ml, c) 0.9 mg/ml, d) 4.0 mg/ml.

After obtaining evidence that **Gd10** does in fact assemble with itself after inclusion of **2**, we were curious to investigate how this inclusion might affect longitudinal relaxivity. Aggregates were formed and immediately analyzed at both 400 MHz and 60 MHz. Interestingly, relaxivity did increase by a small amount at the lower field, but decreased at 400 MHz. This could mean the rotational rates of the aggregates decreased to be further away from 400 MHz

than **Gd10**, but closer to 60 MHz than **Gd10**. If the rotational rates are indeed close to the 60 MHz field, it is surprising the gains are so small. If these aggregates are multi-lamellar assemblies, several of the Gd(III) water exchange sites could be restricted to bulk water exchange, which could certainly become a limiting parameter in contrast enhancement.

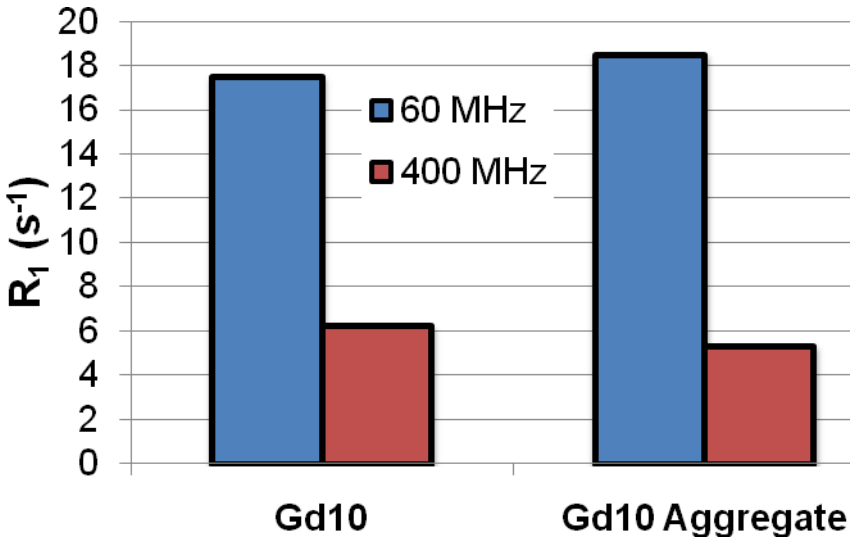

Figure 5-4. Relaxation constants for free **Gd10** and **Gd10** self-assembled aggregates. Particle formulation was carried out as described in the Materials and Methods section at [Gd(III) = 1mM.

Molecular mechanical modeling was carried out in attempt to better visualize the 3-D structure of **Gd10** and **Gd10** included with **2**. Structures of both **Gd10** and **2** were optimized separately (Figures 5-5a-c) to their lowest energy conformations. **Gd10** shown from two different viewpoints to show its tube-like shape (Figure 5-5b) and looking into the hydrophobic cavity (Figure 5-5c). These individual components were then combined so was **2** coupled within the cavity located on the core of **Gd10** and optimized to their minimum energy conformation using a PM3 basis set (Figure 5-4d). The 3-D models give are a good tool to visualize the hydrophobic core of **Gd10** and how it looks in 3-D space with included moieties.

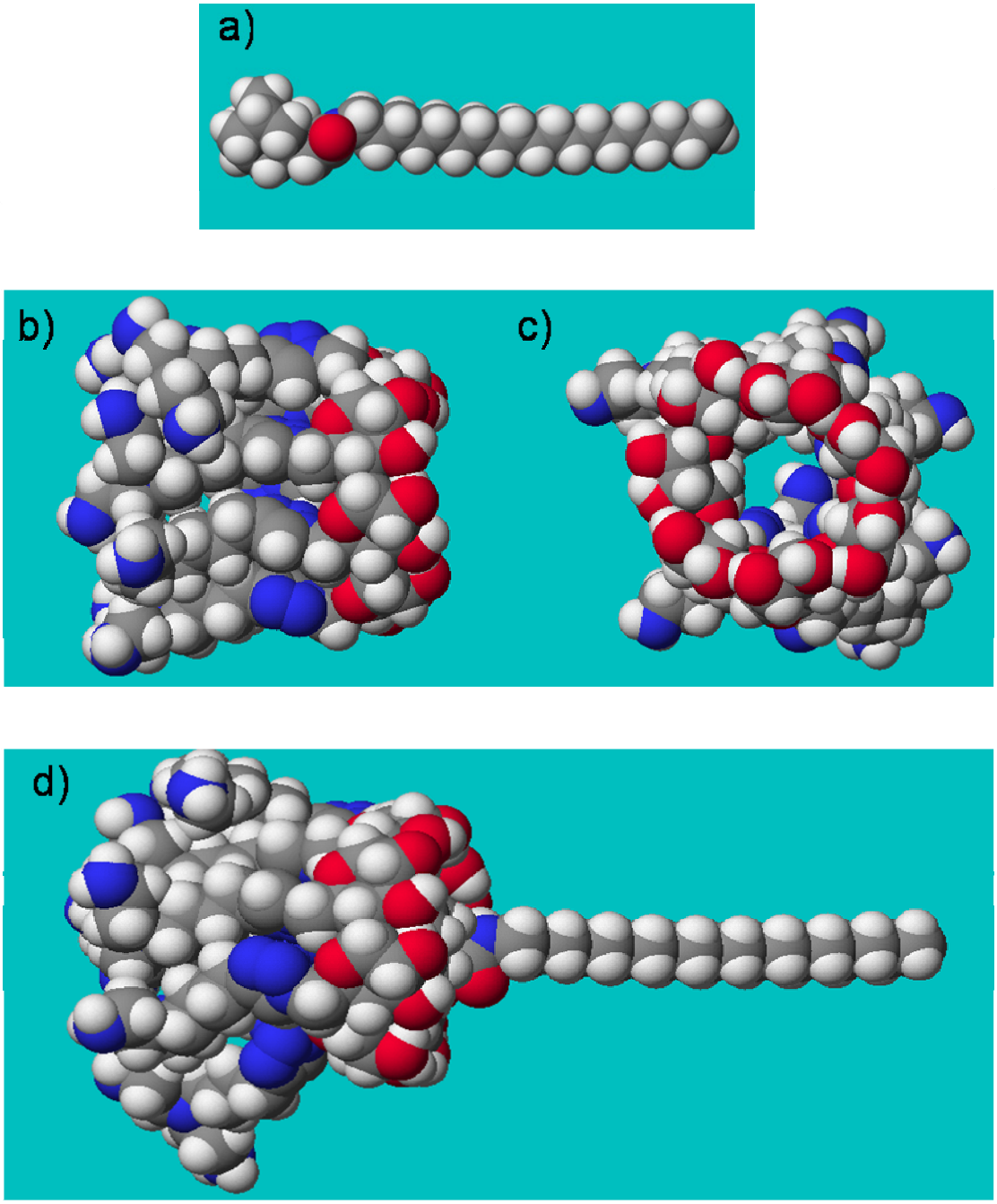

Figure 5-5. a) Optimized structure of: **2**, b) Heptakis{6-*N*-[diethylenetriamine)butyl]-6-(1,2,3-triazole)} cyclomaltoheptaose from the side, c) and looking into the cavity. The optimized structure of **2** included within a model for **Gd10**. This view helps to visualize the hydrophobic tail (right, aliphatic chain) and the polar head group (left).

5.5 Conclusions

Here, we have synthesized adamantane hydrophobic conjugates as guest inclusion moieties for **Gd10**. There is strong evidence, from both DLS and TEM, that these hydrophobic guests mediate self-assembly of **Gd10**. Concentration of self assembled **Gd10** complexes seem to be a driving factor in the final morphology of said complexes. These complexes are stable over a period of 5 hours in water and do not significantly alter the relaxivity enhancement imparted by **Gd10**. Based on the sizes and shapes of aggregates formed, these self-assembled complexes are likely multi-lamellar supramolecular complexes. Further investigations of these complexes are warranted to study the possibility of using these or similar systems *in vivo*.

5.6 Acknowledgement

The authors would like to acknowledge John McIntosh from ICTAS NCFL for his expertise in TEM operation and Prof. Christopher Gulgas, of Longwood University, for access to the Anasazi 60 MHz NMR spectrometer.

5.7 References

1. Auzely-Velty, R.; Djednaini-Pilard, S.; Desert, S.; Perly, B.; Zemb, T. *Langmuir* **2000**, *16*, 3727 – 3734.
2. Auzely-Velty, R.; Pean, C.; Djednaini-Pilard, S.; Zemb, T.; Perly, B. *Langmuir* **2001**, *17*, 504 – 510.
3. Liu, Y.; Xu, J.; Craig, S. L. *Chem. Comm.* **2004**, 1864 – 1865.
4. Wang, Y.; Ma, Z.; Wang, Z.; Zhang, X. *Angew. Chem. Int. Ed.* **2007**, *46*, 2823 – 2826.
5. Wang, J.; Jiang, M. *J. Am. Chem. Soc.* **2006**, *128*, 3703 – 3708.
6. Wu, A.; Shen, X.; He, Y. *J. Colloid and Interface Sci.* **2006**, *302*, 87 – 94.
7. Nakamura, E.; Makino, K.; Okano, T.; Yamaoto, T.; Yokoyama, M. *J. Cont. Rel.* **2006**, *114*, 325 – 333.
8. Accardo, A.; Tesauro, D.; Roscigno, P.; Gianolio, E.; Paduano, L.; D'errico, G.; Pedone, C.; Morelli, G. *J. Am. Chem. Soc.* **2004**, *126*, 3097 – 3107.
9. Accardo, A.; Tesauro, D.; Morelli, G.; Gianolio, E.; Aime, S.; Vaccaro, M.; Mangiapia, G.; Paduano, L.; Schillen, K. *J. Biol. Inorg. Chem.* **2007**, *12*, 267 – 276.
10. Torres, S.; Prata, M. I. M.; Santos, A. C.; Andre, J. P.; Martins, J. A.; Helm, L.; Toth, E.; Garcia-Martin, M. L.; Rodrigues, T. B.; Lopaz-Larrubia, P.; Cerdan, S.; Geraldes, C. F. G. C. *NMR Biomed.* **2008**, *21*, 322 – 336.
11. Shiraishi, K.; Kawano, K.; Minowa, T.; Maitani, Y.; Yokoyama, M. *J. Controlled rel.* **2009**, *136*, 14 – 20.
12. Laurent, S.; Vander Elst, L.; Thirifays, C.; Muller, R. N. *Eur. Biophys. J.* **2008**, *37*, 1007 – 1014.

13. Bryson, J. M.; Chu, W. –J.; Lee, J. –H.; Reineke, T. M. *Bioconjugate Chem.* **2008**, *19*, 1505 – 1509.

14. Bryson, J. M. *Doctoral Dissertation*, **2009**, *Chpt. 4*, 59 – 72.

15. Berne, B. J.; Pecora, R. *Dynamic light scattering*; John Wiley & Sons, Inc.; New York, **1976**.

Chapter 6: Polymeric Lanthanide Beacons for Luminescence and Magnetic Resonance Imaging of DNA Delivery*

*Adapted From: Bryson, J. M.; Fichter, K. M.; Chu, W. –J.; Lee, J. –H.; Li, J.; Madsen, L. A.; McLendon, P.; Reineke, T. M. *Proc. Natl. Acad. Sci.* **2009**, *In Press.*

6.1 Abstract

The delivery of nucleic acids with polycations offers tremendous potential for developing highly specific treatments for a variety of therapeutic targets. While materials have been developed and studied for polynucleotide transfer, the biological mechanisms and fate of the synthetic vehicle has remained elusive due to the limitations with current labeling technologies. Here, we have developed new theranostic polymeric beacons that allow the delivery of nucleic acids to be visualized at different biological scales. The novel polycations have been designed to contain repeated oligoethyleneamines, for binding and compacting nucleic acids into nanoparticles, and lanthanide chelates [either luminescent europium (Eu^{3+}) or paramagnetic gadolinium (Gd^{3+})]. The chelated lanthanides allow the visualization of the delivery vehicle both on the nm/μm scale via microscopy and on the sub-mm scale via magnetic resonance imaging (MRI). We demonstrate that these new delivery beacons effectively bind and compact pDNA into nanoparticles and protect nucleic acids from nuclease damage. The lanthanide-chelate materials have been found to efficiently deliver pDNA into cultured cells and do not exhibit toxicity. Micrographs of cultured cells exposed to the nanoparticle complexes formed with fluorescein-labeled pDNA and the europium-chelated polymers reveal effective

intracellular imaging of the delivery process. MRI of bulk cells exposed to the complexes formulated with pDNA and the gadolinium-chelated structures show bright image contrast, allowing visualization of effective intracellular delivery on the tissue-scale. Because of their versatility as imaging probes, these delivery beacons posses remarkable potential for tracking and understanding nucleic acid transfer *in vitro* and have promise for *in vivo* imaging applications.

6.2 Introduction

The delivery of therapeutic nucleic acids such as siRNA, antisense agents, transcription factor decoys, and plasmid DNA (pDNA) offers an unprecedented opportunity for developing highly specific treatments for many devastating diseases.[1-5] The use of synthetic materials, such as polymers, for polynucleotide delivery has rapidly grown and presents a wealth of promising alternatives to conventional viral vectors,[6-11] which have caused serious problems in the clinic. While much is known about the infection pathways, advantages, and troubles of viral vectors,[12-14] researchers in the field of non-viral delivery are just beginning to understand the transfection mechanisms, benefits, and potential issues with the multitude of materials being developed as macromolecular drug carriers.[15-18] Considering that the delivery vehicle plays a central role in the mechanisms, kinetics, efficacy, and toxicity of nucleic acid medicines, little is known about how the vehicle structure affects drug fate both *in vitro* and *in vivo*. For this reason, smart biomaterials termed "theranostic" agents are being developed that provide therapeutic delivery, diagnostic imaging, and the ability to monitor treatment efficacy.[19-21] Indeed, the parallel development of novel nucleic acid drugs and theranostic vehicles that offer disease diagnosis,

treatment, and the ability to understand the delivery mechanisms/kinetics on a range of biological scales will advance this field toward the discovery of personalized treatment strategies.

Tracking the delivery of nucleic acids within cells and tissues has traditionally been accomplished by a number of methods such as labeling nucleotides with fluorescent dyes,[18,22] radiotracers,[19,23] quantum dots,[24,25] and/or with various reporter gene assays.[9,19] While these methods have yielded a means of monitoring the presence and location of nucleic acids, many issues have surfaced with labeling polymeric delivery vehicles with these techniques. For example, the polymer labeling efficiency is often poor, non-uniform, irreproducible, and difficult to characterize. Also, dyes can alter the delivery mechanisms and/or increase side-effects, thus misrepresenting the true delivery mechanisms and location of the native unlabeled materials.[24] For this reason, the development of new material-based delivery systems that allow monitoring of both the nucleic acid and the delivery vehicle, on the cellular and tissue scales, is essential to improve the delivery efficiency, optimize the vehicle structure, and monitor treatment efficacy in living systems.

Lanthanide (Ln) metals are endowed with several unique properties that can be exploited for the development and study of non-viral delivery vehicles. Chelates of these metals are routinely used as luminescent probes,[26] sensors,[27,28] and imaging agents,[29-32] in many diverse fields. Complexes housing luminescent lanthanides, such as europium (Eu^{3+}), offer many unique advantages over the aforementioned labeling methods due to their small hydrophilic structures, long luminescence lifetimes, large Stokes shifts, and their stability from quenching and photobleaching.[27, 33-35] Also, the chelates of lanthanides are relatively nontoxic;[31,36] structures containing gadolinium (Gd^{3+}) are FDA-approved as MRI contrast agents due to their paramagnetic nature and slow electronic relaxation time.[30-32] Moreover, polymers and

macromolecules containing gadolinium chelates generally have higher relaxivity profiles than small molecule chelates because of increases in the rotational correlation time, which improves resolution and sensitivity.[37,38] MRI is advantageous for following drug delivery *in vivo* with very high resolution because it is non-invasive, safe, and new high magnetic field MRI instruments are rapidly being developed to further improve sensitivity.[39,40] Lastly, this technique does not expose patients to harmful radiation, which occurs in other imaging methods used to follow drug treatment such as computed tomography and positron emission tomography.[41]

The novel polymer delivery vehicles developed herein offer a creative and powerful method for tracking the delivery of nucleic acids. As shown in Figure 1, we have designed these novel delivery beacons to contain systematically repeated lanthanide chelates within an oligoethyleneamine backbone. We have found that these materials can bind and compact pDNA into nanoparticles (termed polyplexes) that are taken up into cultured human cervix adenocarcinoma (HeLa) cells in an effective and nontoxic manner. We reveal that these novel delivery beacons offer a dual imaging modality for tracking transport *in vitro* on the nm/μm-scale via microscopy (using the luminescent Eu^{3+}-chelated structures) and for detection via MRI within bulk cultured tissues on the sub mm-scale (using the paramagnetic Gd^{3+}-chelated materials). These scaffolds offer a unique motif that can be readily tailored and optimized as both luminescent and MRI theranostic pDNA delivery agents.

6.3 Materials and Methods

6.3.1 Materials

Diethylenetriaminepentacetic acid and ethyl trifluoroacetate were obtained from Alfa Aesar Chemical Co. (Ward Hill, MA). All other reagents and solvents used in the synthesis were obtained from Aldrich Chemical Co. (Milwaukee, WI) and were used without further purification. Monomers **1a** and **1b** were synthesized following a previously published procedure developed in our lab.[10] Diethylenetriaminepentacetic acid bisanhydride (DTPA-BA) was prepared using a standard procedure.[45]

6.3.2 Cell Culture Materials

Media and supplements were purchased from Gibco/Invitrogen (Carlsbad, CA). HeLa cells were purchased from ATCC (Rockville, MD) and cultured according to specified conditions. Plasmid DNA, pCMVb and gWiz-Luc, were purchased from PlasmidFactory (Bielefeld, Germany), and Aldeveron (Fargo, ND), respectively. Nuclease free water, Opti-MEM, and DMEM (supplemented with 10% fetal bovine serum (FBS), 100 units/mL penicillin, 100 μg/mL streptomycin, and 0.25 μg/mL amphotericin) and PBS were all purchased from Invitrogen (Carlsbad, CA). Luciferase substrate reagent and cell culture lysis buffer used in the transfection efficiency assays were purchased from Promega (Madison, WI). A Bio-RAD DC protein assay kit used in the viability assay was purchased from Bio-Rad (Hercules, CA). FITC-labeled pDNA and the Cy5 nucleic acid labeling kit was purchased from Mirus (Madison, WI).

6.3.3 Monomer and Polymer Synthesis

Synthesis of *Poly*([N^2, N^3, N^4 – tris(*tert*-butoxycarbonyl)tetraethylenetriamine] amidodiethylenetriaminetriaacetic acid), **2a.** Polymer **2a** was prepared by dissolving monomer **1a** (3.63g, 7.41mmol) in 25ml of dimethylsulfoxide (DMSO) at room temperature. DTPA-BA (2.64g, 7.41mmol) was dissolved in 5ml of DMSO and added directly to the solution of **1a** under constant stirring. The polymerization was carried out for 18h after which the solution was pipetted into a 6000-8000 Da MWCO dialysis bag (Spectrum laboratories Inc., Rancho Dominguez, CA) and dialyzed extensively against methanol for 18h, after which the solution was removed from the bag and evaporated *in vacuo* to yield **2a** as an orange viscous oil (yield = 3.88g, 47%). ^{1}H-NMR (d^3-MeOD): δ = 1.57 (s, 27H), 3.08 (s, 4H), 3.30 (bm, 20H), 3.43 (bs, 6H), 3.69 (s, 4h) ^{13}C-NMR (d^3-MeOD): δ = 30.21, 37.42, 40.87, 44.33, 46.03, 47.10, 49.02, 50.94, 52.63, 55.52, 57.64, 79.14, 154.95, 15 5.14, 169.77, 170.89, 173.02. FTIR (KBr): See Table 1

Synthesis of *Poly*([N^2, N^3, N^4, N^5, - tetrakis(*tert*-butoxycarbonyl)pentaethylenetetramine] amidodiethylenetriaminetriaacetic acid), 2b. Monomer **1b** (4.77g, 7.54mmol) was dissolved in 25ml of DMSO at RT. DTPA-BA (2.69g, 7.54mmol) was dissolved in 5ml of DMSO and added directly to the solution of **1b** under constant stirring. The polymerization was carried out for 18h after which the solution was transferred to a 6000-8000 Da MWCO dialysis bag (Spectrum laboratories Inc., Rancho Dominguez, CA) and dialyzed extensively against methanol for 18h, after which the solution was removed from the bag and evaporated to yield 2b *in vacuo*

as a deep amber oil (yield = 4.17g, 56%). ^{1}H-NMR (d^3-MeOD): δ = 1.57 (s, 27H), 3.10 (s, 8H), 3.28-3.53 (bm, 20H), 3.43 (bs, 6H), 3.69 (s, 4H). ^{13}C-NMR (d^3-MeOD): δ = 28.49, 37.27, 37.79, 40.87, 44.33, 45.04, 45.96, 46.98, 49.02, 50.94, 52.63, 55.52, 57.64, 79. 14, 154.95, 155.14, 169.77, 170.89, 173.02. FTIR (KBr): See Table 1

General Synthesis of *Poly*[(tetraethylenetriamine)amidodiethylenetriaminetriaacetic acid], 3a and *Poly*[(pentaethylenetetramine)amidodiethylenetriaminetriaacetic acid], 3b. An aliquot of 5 mmol of each protected polymer (**2a** or **2b**) was dissolved in 20ml of CH_2Cl_2 and cooled to 0°C. Next, 20 ml of trifluoroacetic acid was added to each solution and the reaction was warmed to room temperature. The reactions were allowed to proceed for 3h, after which the solvents were removed *in vacuo* and each mixture was redissolved in water. Both water solutions were brought to a pH = 6 using a 1M sodium bicarbonate. Subsequently, the solutions were each deposited in a separate 6000-8000 Da MWCO dialysis bag (Spectrum laboratories Inc., Rancho Dominguez, CA) and dialyzed against ultrapure water for 24h. The dialyzed solutions were lyophilized to yield the fluffy, unchelated polymers **3a** and **3b** (yields = 1.88g, 76%; 1.97g, 80%, respectively)

Characterization for Polymer **3a**

Yield = 1.88g, 76%

^{1}H-NMR (D_2O): δ = 3.08 (s, 4H), 3.24-3.50 (bm, 20H), 2.54 (bs, 6H), 3.77 (s, 4H)

^{13}C NMR (D_2O): δ = 35.67, 43.90, 44.08, 47.56, 50.93, 53.43, 55.04, 58.72, 171.61, 173.31, 177.64.

FTIR (KBr): See Table 1

GPC-light scattering: See Table 3

Characterization for Polymer **3b**

Yield = 1.97g, 80%

^{1}H-NMR (D_2O): δ = 3.03 (s, 4H), 3.21-3.49 (bm, 20H), 2.54 (bs, 6H), 3.77 (s, 4H)

^{13}C NMR (D_2O): δ = 35.74, 43.86, 44.28, 45.11, 47.34, 50.88, 53.39, 55.00, 58.72, 171.59, 173.29, 177.67.

FTIR (KBr): See Table 1

GPC-light scattering: See Table 3

General Synthesis of *Poly*[(tetraethylenetriamine)amido (Ln^{3+})diethylenetriaminetriacetate], Eu3a or Gd3a and *Poly*[(pentaethylenetetramine)amido (Ln^{3+})diethylenetriaminetriacetate], Eu3b or Gd3b. A 2mmol aliquot of each unchelated polymer, **3a** and **3b**, was dissolved in 20ml of ultrapure water at room temp. Next, 2 mmol of $LnCl_3$ (either $EuCl_3$ or $GdCl_3$) was dissolved in 5ml of water and dripped into the respective polymer solution in 3 separate aliquots. The pH was adjusted to pH = 6 after each aliquot addition. The solution was allowed to stir for 2h and then was dialyzed in a 6000-8000 Da MWCO bag against ultrapure water for 24h. Dialyzed solutions were lyophilized to yield fluffy off-white polymers **Gd3a**, **Gd3b**, **Eu3a**, and **Eu3b** (yields = **Gd3a**=1.20g, 86%; **Gd3b** = 1.19g, 80%; **Eu3a** = 1.13g, 81%; **Eu3b** = 1.17g, 79%)

FTIR (KBr): See Table 1

Lanthanide Quantification: See Table 2

GPC-light scattering: See Table 3

6.3.4 Polymer Characterization.

The molecular weight and polydispersity for polymers **3a**, **3b**, **Eu3a, Eu3b, Gd3a**, and **Gd3b**, were measured with a Viscotek GPCmax instrument equipped with a $GMPW_{xl}$ (aqueous phase) column coupled to a triple detection system (static light scattering, viscometry, and refractive index) as shown in Table 3. A solution of 0.5M sodium acetate containing 20% acetonitrile was used as the mobile phase. Each sample was dissolved in the mobile phase, injected into the instrument (100uL loop, 8-12mg/mL), and eluted at a flow rate of 0.80 ml/min. A monodisperse polyethylene oxide standard weighing 22kDa was used as a reference standard for these experiments. NMR spectra were acquired on a Bruker AV-400 MHz spectrometer. ^{1}H NMR data are reported as follows: chemical shift (δ ppm), multiplicity (s = singlet, d = doublet, t = triplet, q = quartet, m = multiplet, bs = broad singlet), and the peak integration. It should be mentioned that neither ^{1}H nor ^{13}C NMR data could be collected for **Eu3a**, **Eu3b**, **Gd3a**, and **Gd3b**, due to the paramagnetic nature of these materials. Mass spectra were obtained with an IonSpec ESI mass spectrometer in positive ion mode. IR spectra were measured on a Perkin Elmer Spectrum One Fourier transform infrared spectrometer as KBr pellets. Lanthanide quantification was carried out on a ICP-MS (Octapoler detection, Agilent Technologies, Santa Clara, CA), which monitored Gd isotopes (157, 158 Da) and Eu isotopes (151, 153 Da). These data was used to generate a calibration curves for both Gd^{3+} and Eu^{3+}. Polymers were dissolved and diluted to the ppb range so they could be analyzed within the proper calibration curve range.

6.3.5 Gel Electrophoreses Shift Assay.

Polymers **3a**, **3b**, **Gd3a**, **Gd3b**, **Eu3a**, and **Eu3b**, were studied for their ability to bind pDNA using gel electrophoreses. Each polymer was dissolve in nuclease-free water (Gibco,

Carlsbad, CA). Next, solutions of pDNA (1ug, 0.1ug/uL) were titrated with equal volumes of polymer solutions to form polyplexes at N/P ratios varying from 0-50 (N = secondary amines on polymer, P = phosphate groups on the pDNA) and allowed to incubate for 30min at room temperature. Loading buffer (2μl) was added to each of the prepared polymer-pDNA solutions (Blue Juice, Invitrogen, Carlsbad, CA). The gel composition was agarose 0.6% w/v, which contained ethidium bromide (0.6 ug/mL) and was prepared in TAE buffer (40 mM Tris-acetate, 1 mM EDTA). Aliquots (20ul) of each polyplex solution were deposited into each well. An applied field of 60V was used to facilitate pDNA migration. Polymer-pDNA complex formation is illustrated by lack of pDNA band migration in the electrophoretic field, illustrating charge neutralization of the DNA phosphates.

6.3.6 Nuclease Degradation Assay.

Polymers were tested for their ability to protect nucleic acids from nuclease degradation. The experimental procedure to monitor the ability of the polymers to protect pDNA from nuclease degradation was modified from a previously published procedure.[42] Each polymer (5 μL) was combined with pCMVβ (1μg in 5μL of water) to form polyplexes at N/P = 40. After 30 min, fetal bovine serum (FBS, 5 μL) was added to each polyplex solutoin. Polyplexes for all polyplexes were allowed to incubate for times of: 0, 1 , 2, 4, and 6h, at 37°C. After each incubation time, the samples were treated with 10% sodium dodecyl sulfate (SDS, 2 μL) and then stored at 4^{o}C until all samples were finished incubating. All trials were then incubated at 60°C for 18h to release the polymer from the pDNA. After incubation each aliquot was titrated with a loading buffer (Blue Juice, Invitrogen, Carlsbad, CA, 2 μL), loaded onto an agarose gel

(0.6%, 3 μL ethidium bromide) in 20 μL aliquots, and electrophoresed to show evidence of plasmid degradation. pDNA only and FBS were used as negative controls.

6.3.7 Dynamic Light Scattering and Zeta Potential Measurements.

Polyplex sizes were measured using a Zetasizer (Nano ZS) dynamic light scattering instrument with a 633nm laser (Malvern Instruments, Malvern, UK). Polyplexes were formed at N/P ratios at 10, 20, 30, 40, and 50 by combining equal volumes of a polymer solution in ultrapure water with a 0.02mg ml^{-1} pDNA solution and allowing the polyplexes to form for 1 hr. The particle size measurements were carried out at 25ºC with a detection angle of 173º. The Zeta potential measurements of the polyplexes (formed with the same technique as described above) were carried out on the same instrument using a detection angle of 17º. Plasmid DNA was measured in PBS buffer (Appendix B)

6.3.8 Transmission Electron Microscopy (TEM).

Polyplexes were formed at an N/P=40 ([pDNA] = 0.02 mg/ml, using equal volume aliquots of polymer or pDNA solutions in water). Samples (1μL) were applied to 400-mesh carbon-coated grids (EMS, Fort Washington, PA) and allowed to set for 60 sec before blotting with filter paper. Samples were negatively stained with a 2% uranyl acetate solution and allowed to settle for 60 sec before excess solution was blotted off and air dried for 5 min. Transmission electron micrographs were obtained on a Philips EM 420 Scanning Transmission Electron Microscope in TEM mode with a 120kV beam.

6.3.9 Cellular Delivery of pDNA and Cell Viability Analysis.

Twenty-four hours prior to transfection, HeLa cells were seeded in 6 well plates at a density of 250,000 cells/well and incubated in supplemented DMEM (10% FBS) at 37°C and 5 % CO_2. Polyplexes were formulated by adding 250μL solutions of each polymer dissolved in water (concentration calculated based on N/P ratios of 40 and 60) to 5 μg of Cy5-labeled pDNA (250 μL solution). Polyplexes of Jet-PEI and **G4** were formulated using the same methodology. Polyplexes were incubated at room temperature for 1 hour. Just prior to transfection, 1mL Opti-MEM was added to each solution. Cells were aspirated of old media, washed with 1mL PBS, and the appropriate polyplex solution was added to each well. Cells were then incubated at 37°C under a 5% CO_2 atmosphere for 4 hours. The cell suspensions were then prepared for analysis as previously described.(*10*) HeLa cell suspensions were analyzed on a FACS Canto II flow cytometer equipped with a 633 nm helium-neon laser. Mean Cy5 fluorescence intensity was measured using the appropriate forward and side scatter gates. A control of un-transfected cells was used to create a gate such that less than 1% of cell-associated autofluorescence is detected in the Cy5 channel. This gating strategy was used for subsequent samples of transfected cells to determine the percent of cells transfected. For gene expression analysis, polyplexes were formulated in an identical manner as above except with GWiz-luc pDNA and allowed to transfect cells for 48 hr prior to assaying for luciferase activity according to previously published methods.(*42*) Cell viability was characterized by measuring the amount of protein in cell lysates using a Bio-Rad DC protein assay kit (Hercules, CA) in triplicate. Viability is reported as the fraction of protein in each sample normalized to a control of untransfected cells.

6.3.10 Fluorescence microscopy.

Twenty-four hours prior to transfection, cells were seeded in 6 well plates containing 25 mm No. 1 glass coverslips at a density of 50,000 cells/well. Just prior to transfection, polyplexes were formed as noted above for the cellular uptake assays except 200 μL of polymer solution was added to 200 μL of FITC-labeled pDNA ([pDNA] = 0.02 mg/ml, N/P = 40. Cells were removed from the incubator, aspirated of old media, washed with 2mL PBS, and 2mL Opti-MEM was added to each well. To transfect cells, 1mL Opti-MEM from each well was added to the appropriate polyplex solution, pipetted up and down to mix, and returned to the well to deliver a total of 4 μg DNA per well. Four hours after transfection, 2.4mL of supplemented DMEM was added to each well. Twenty-four hours after transfection, cells were aspirated of old media, washed 3 times with 1mL PBS, and fixed for 2 hours using 2% paraformaldehyde in PBS (pH 7.4) at 4 °C. Afterwards, coverslips were removed from each well and carefully washed 4 times with 0.5 mL PBS. Coverslips were then mounted in Pro-long antifade mounting media (Molecular Probes, Eugene, OR) and allowed to dry at room temperature overnight. Cells were observed using a Zeiss Axioplan Imaging 2 infinity-corrected, upright scope (Thornwood, NY), a 63x oil objective (N.A. 1.4), and standard filter sets for FITC and Rhodamine. To visualize Europium luminescence, a custom filter set (excitation max 405 nm +/- 40 nm, dichroic 440 nm LP, emission max 610 +/- 75 nm) was built from filters purchased from Chroma (Rockingham, VT). Images of each cell were collected as z-stacks with a z-spacing of 0.27 μm (**Eu3a** and **Eu3b**) using an Orca-ER CCD camera (Hamamatsu, Japan). The resulting images were processed using AutoQuant Autodeblur (Media Cybernetics, Bethesda MD). Data correction for each z-stack was applied for bias and flatfield frame and optical density. Then stacks were

processed using 3D blind deconvolution over 50 iterations. The final fluorescence images were minimally processed for background subtraction, brightness, and contrast. To increase fine detail in some DIC images, filters for pseudoflatfield and kalman stack were applied. After deconvolution, all image processing was completed using ImageJ open source software (U.S. National Institutes of Health, Bethesda, MD).[46]

6.3.11 Inversion Recovery Experiments of Polyplexes in Solution.

T_1 measurements were carried out on Bruker AMX-400MHz (9.4T) and Anasazi FT-NMR 60MHz (1.41T) NMR spectrometers. Polyplexes were formed at an N/P = 40 such that the concentration of Gd^{3+} was 1mM. Additionally, the relaxivity of Magnevist^{TM} (Gd^{3+}-DTPA) was measured at both fields for comparison. After an incubation time of 30 min the longitudinal relaxation time (T_1) for each solution was measured using an inversion recovery pulse sequence (180° – d_t – 90° – acquire) at 298K. Arrayed data [n(d_t) = 10] was processed using Acorn NUTS software and fit to a three-parameter model. The inverse of the T_1 data was used to determine the longitudinal relaxation rate constants (R_1) imparted by the polyplexes. Solution concentration data for beacons **Gd3a** and **Gd3b**, as well as the Magnevist^{TM} control were used to calculate relaxivity ($\mathbf{r_1}$) by generating a curve fit to $(1/T_1) = [Gd^{3+}](r_1) + b$, where $b = (1/T_1)$ for the working solvent (water).

6.3.12 Magnetic Resonance Imaging of Transfected Cells.

Twenty-four hours prior to transfection, HeLa cells were seeded in 10 flasks (with a surface area of $75cm^3$) at a density of $4.0x10^6$ cells/flask. Polyplexes were prepared 1 hour prior

to transfection using βCMV pDNA and the respective polymer at an N/P ratio of 40. Cells were transfected in 15mL Opti-MEM using 80μg pDNA/flask. Non-transfected cells were subjected to the same media changes as the transfected cells. Four hours after transfection, 15mL of DMEM containing 10% FBS was added to each well. Twenty-four hours after transfection, cells were aspirated of media, washed extensively with PBS and collected via trypsination. Cells were pelleted and resuspended in PBS twice, then pelleted again in 0.5 mL Eppendorf tubes for analysis. All MR images were acquired with a Bruker Avance III NMR spectrometer equipped with an imaging probe containing a 3cm transverse coil. The images were acquired using a RARE-inversion recovery T_1-weighted pulse sequence. Acquisition parameters are as follows: TR (repetition time) = 3500 msec, TI (inversion time) = 1200 msec, TE (echo time) = 8.5 msec, FOV = 3x3 cm and resolution = 256x256. T_1 measurements of these same cell pellets and controls were carried out using this same on a Bruker AMX-400MHz spectrometer. For the T_1 experiments, the Hela cell pellets used for the MRI experiment were suspended in PBS buffer to make turbid solutions that were deposited into NMR tubes and allowed to rest for 24h. Upon settling, each tube contained ~4cm of sedimented HeLa cell pellets. NMR tubes were placed so the entirety of the HeLa pellet was within the NMR coil. The longitudinal relaxation time (T_1) for each pellet and the control solutions were measured using an inversion recovery pulse sequence ($180° - d_t - 90° -$ acquire) at 298K. Arrayed data ($n(d_t) = 10$) was processed using Acorn NUTS software and fit to a three-parameter model.

6.4 Results and Discussion

6.4.1 Polymer Synthesis and Polyplex Formation.

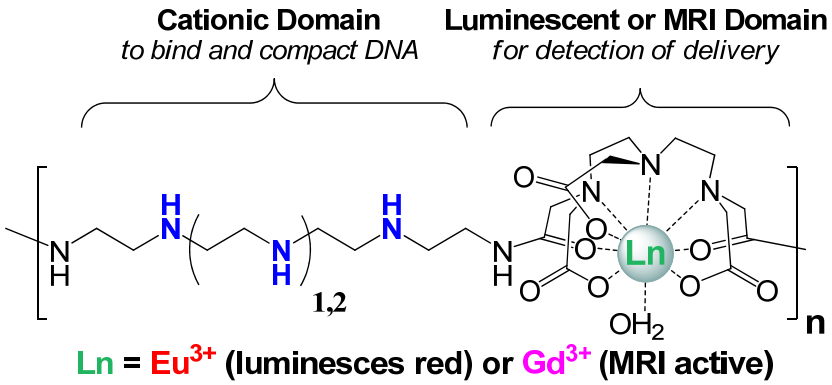

Figure 6-1: We have developed two novel polymeric DNA delivery vehicles that contain systematically-repeated lanthanide chelates, which serve as imaging beacons. The figure above represents two analogous structures that differ in the length of the ethyleneamine block in the repeat unit (**3a** or **3b** containing 3 or 4 ethyleneamines, respectively). These two analogs can be chelated with either Eu^{3+} or Gd^{3+} for microscopy and MRI imaging respectively.

The design of these materials (Figure 1) was inspired by the characteristics of successful cationic nucleic acid delivery vehicles and the many elegant macromolecular imaging agents being examined for disease diagnosis. The amine-containing co-monomer precursors were synthesized using a series of protection/deprotection reactions previously published by our lab to obtain **1a** and **1b** (Scheme 6-1).[10] Next, DTPA-BA was reacted with **1a** or **1b** in dimethylsulfoxide at room temperature for 24 hours to form two new polymer structures **2a** and **2b** with protected oligoethyleneamine units and pendant carboxylates from the anhydride ring opening during polymerization (Scheme 6-1). The Boc protecting groups were removed via conventional methods yielding **3a** and **3b**, which was confirmed by NMR analysis. The deprotected precursors were then fully-chelated with the chloride salts of Eu^{3+} and Gd^{3+}

(confirmed via FT-IR and ICP-MS, Table 6-1 and 6-2), while maintaining a neutral pH. The final Ln-chelated polymers were analyzed via GPC using a triple detection system (refractive index, static light scattering, viscometry) to determine the weight averaged molecular weight (M_w), polydispersity index (M_w/M_n), and degree of polymerization (n_w) (Table 6-3). A similar molecular weight, degree of polymerization, and polydispersity, were achieved for all polymer structures **3a, 3b, Eu3a**, **Eu3b Gd3a,** and **Gd3b** (Table 6-3), which was expected because all of the Ln-containing polymers were synthesized from the same parent batches of **3a** and **3b**. Because of similarities in polymer characteristics and the similar chemical properties of lanthanides in the 3+ oxidation state, sound comparison of polymer biological activity was possible between the different analogs.

Scheme 6-1: Polymer Synthetic Scheme[a]

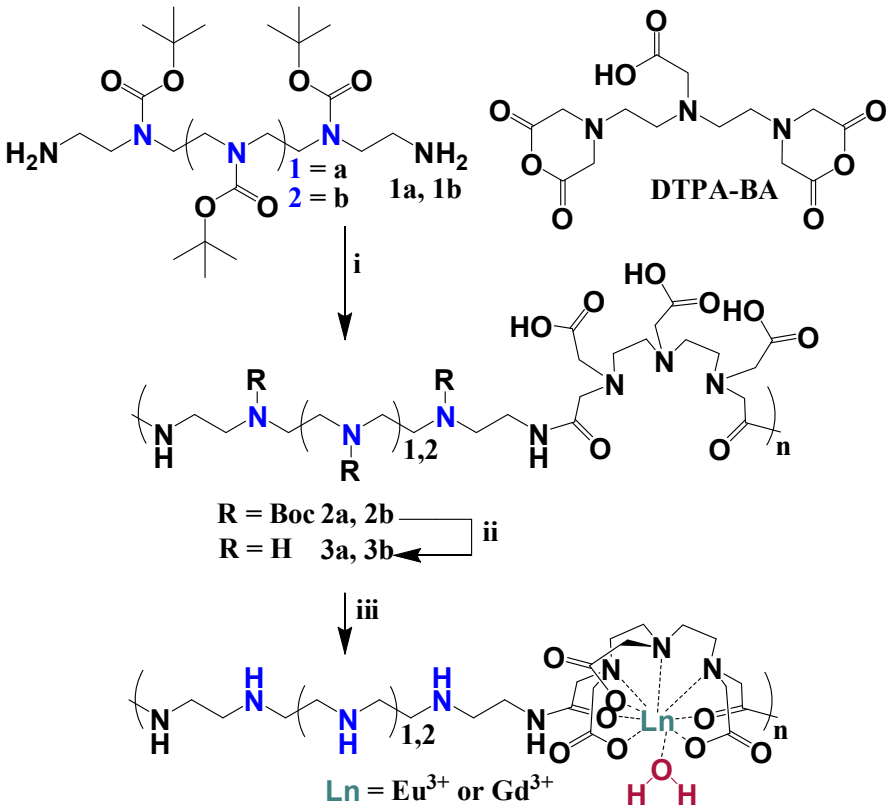

[a]Conditions: (i) DMSO, 25°C, 24h; (ii) TFA, CH_2Cl_2; (iii) [$LnCl_3$] = 0.1 M, H_2O, $NaHCO_3$ pH = 6.

Polymer	υ (cm^{-1})		
2a	1663.3,	1712.3,	3334.2
2b	1666.3,	1692.9,	3346.3
3a	1641.2,	1692.9,	3415.2
3b	1650.8,	1667.8,	3419.2
Eu3a	1585.4,	1634.5,	3419.4
Eu3b	1585.2,	1633.8,	3419.9
Gd3a	1587.2,	1641.2,	3433.7
Gd3a	1586.1,	1633.9,	3419.6

Table 6-1: FT-IR data for the polymers. Samples of each polymer (5mg) were crushed by mortar and pestle with 20 mg of anhydrous KBr and compacted into a translucent pellet. Spectra were measured on a Perkin Elmer Spectrum One Fourier transform infrared spectrometer.

Polymer	Calculated Lanthanide Content	Observed Lanthanide Content
Eu3a	21.8%	21.8%
Eu3b	20.5%	20.4%
Gd3a	22.5%	22.8%
Gd3a	21.1%	21.9%

Table 6-2: Lanthanide quantification for the polymer series. The percent of lanthanide by mass was determined by diluting polymer samples to the ppb range (< mg/mL) and analyzed by inductively coupled plasma mass spectrometry. For each polymer, the signal integration was fitted to calibration curves generated from lanthanide standards.

Polymer	M_w (kDa)	M_w/M_n	n_w
3a	43	1.7	78
3b	54	1.9	91
Eu3a	64	1.7	91
Eu3b	68	1.7	92
Gd3a	67	1.9	96
Gd3a	62	2.0	89

Table 6-3: The weight averaged molecular weight (M_w), polydispersity (M_w/M_n), and degree of polymerization (n_w) for the polymers.

The polymers, **3a**, **3b**, **Eu3a**, **Eu3b**, **Gd3a**, and **Gd3b** were examined for their ability to complex pDNA using an electrophoretic gel shift assay (Figure 6-2). Polyplexes were formulated at N/P ratios (N = the polymer secondary amine number and P = the DNA phosphate number) between 0 and 40 before being electrophoresed in an agarose gel. Polymers **Eu3a**, **Eu3b**, **Gd3a**, and **Gd3b** began to charge-neutralize pDNA at an N/P ratio of 5 and pDNA migration was mostly suppressed at N/P of 20. With these polymers, the N/P ratio needed to fully inhibit gel migration of pDNA was slightly higher than expected when compared to similar polyamidoamine vehicles created in our laboratory.[9,10] The slight bulkiness of the lanthanide chelate and the presence of the carboxylate groups could have an effect on suppressing the binding through steric hindrance and lower cationic charge on the polymer backbone. It is interesting to note that the non-chelated polymers (**3a** and **3b**) do not bind with pDNA in these assays even at an N/P ratio of 100 likely because these structures do not exhibit a high cationic charge and are zwitterionic at physiological pH.

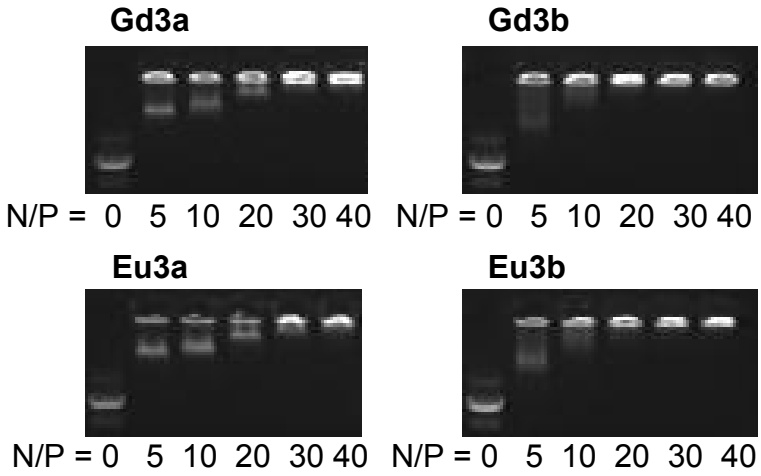

Figure 6-2: Agarose gel electrophoresis shift assays that allow observation of **Gd3a**, **Gd3b**, **Eu3a**, and **Eu3b** binding with pDNA at increasing N/P ratios from 0 to 40. Hindrance of pDNA migration is noted with all polymers at N/P = 5, however, migration is not completely hindered until N/P = 30 for **Eu3a** and **Gd3a** and N/P = 20 for **Gd3b** and **Eu3b**. Non-chelated polymers **3a** and **3b** do not hinder to pDNA migration in agarose gel (data not shown) and thus do not bind pDNA.

The size and morphology of the polyplexes were then examined via transmission electron microscopy (TEM) and dynamic light scattering. TEM micrographs indicate that the polyplexes formulated with **Eu3a** and **Eu3b** and pDNA at N/P of 40, exhibit spherical morphology with particle diameters between 35-60 nm in their dehydrated form (Figures 6-3a and 6-3b). Dynamic light scattering (DLS) and zeta potential data (Figure 6-3b) generally showed larger particle sizes as a result of the hydrodynamic radii that the particles gain in aqueous solution. In the DLS studies, the size of **Gd3a** polyplexes slightly decreased with the N/P ratio (from 74 nm to 66 nm), yet, **Gd3b** polyplexes generally increased in size with the N/P ratio (from 53 nm to 78 nm). Zeta potential measurements reveal that polyplexes exhibited a positive surface charge (between 20-40 mV) that increased with the N/P ratio. It should be noted that we could not analyze polyplexes formed with **Eu3a** and **Eu3b** via dynamic light scattering and Zeta potential measurements due to laser/detector interference with the absorption/luminescence emission bands of Eu^{3+}.

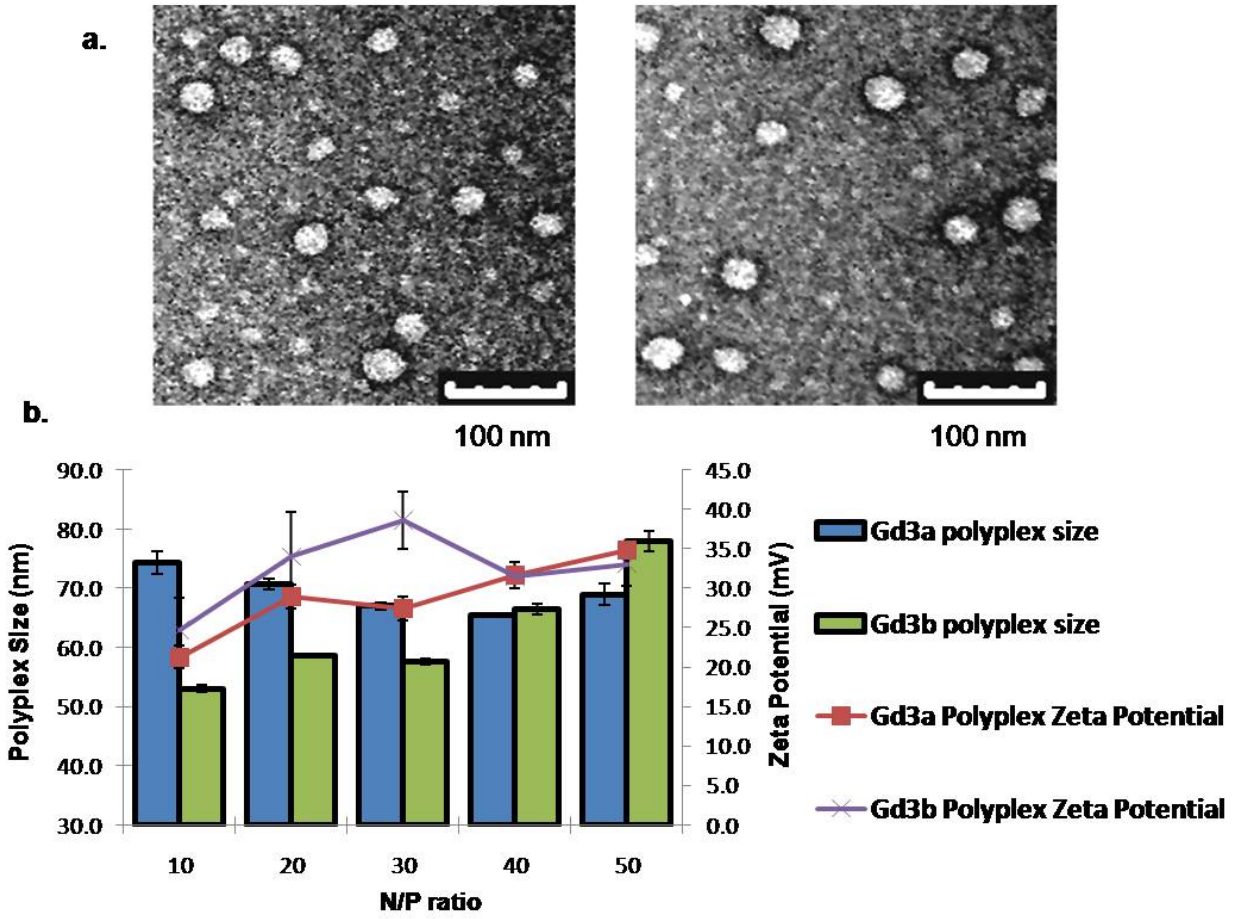

Figure 6-3: a) Transmission electron microscopy (TEM) micrographs of dehydrated (i) **Eu3a** and (ii) **Eu3b** polyplexes. Polyplexes were prepared using a pDNA concentration of 0.02 mg/mL and polymer concentration corresponding to N/P = 40. Polyplexes were negatively stained with uranyl acetate. Images were acquired with a 120kV electron beam, using an LCD camera. The scale bars represent 100 nm in both images. b) Dynamic light scattering and Zeta potentials of polyplexes at N/P ratios of 10, 20, 30, 40 and 50. Polyplexes were prepared in a similar manner to the TEM experiments. Dynamic light scattering and zeta potential were measured in triplicate.

Next, we examined the stability of these polyplexes from nuclease degradation by exposing them to fetal bovine serum (FBS) and observing pDNA integrity via gel electrophoresis. These data show there is no evidence of pDNA degradation in the polyplexes at any time point assayed (shown as the lack of formation of band 4, Figure 6-4, Gels **Eu3a**, **Eu3b**, **Gd3a**, and **Gd3b**). Furthermore the brightness of the pDNA band in the polyplex gels (band 2,

Figure 6-4) remains constant as a function of exposure time. In the control gel of naked pDNA (gel **pDNA**, lanes 9-12), band 2 was completely absent and band 4 (degraded DNA) was clearly observed, indicating full degradation after only one hour of incubation in 25% FBS.

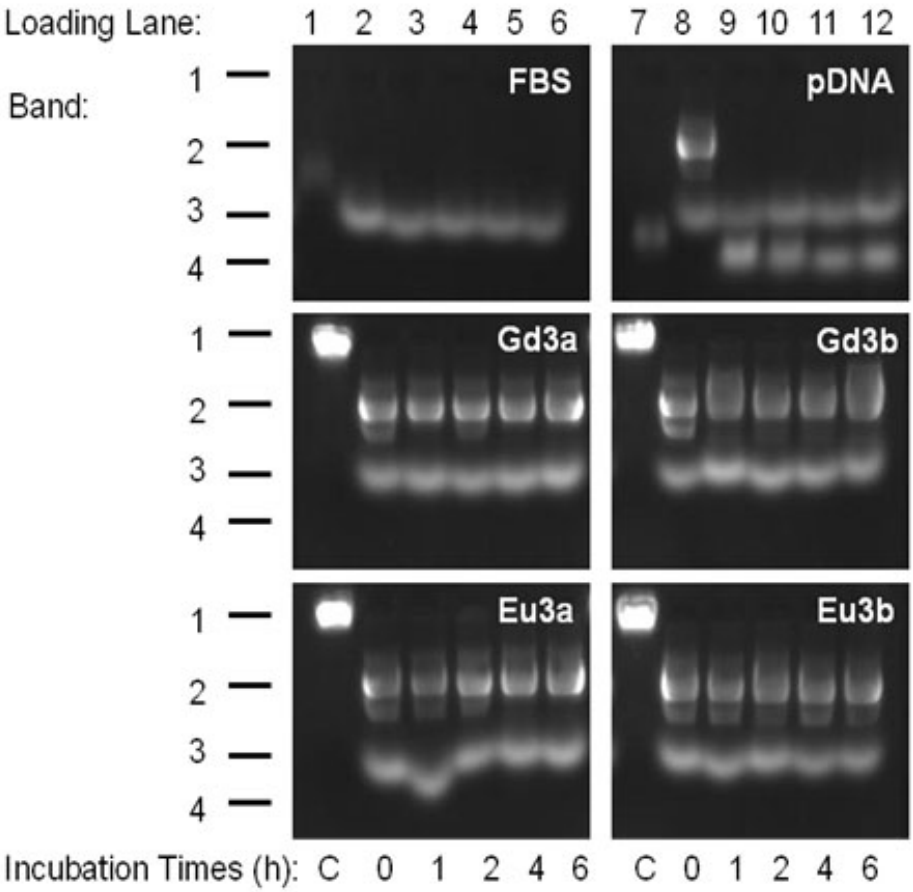

Figure 6-4: The ability of each polymer beacon to protect pDNA from nuclease degradation. Polyplexes are exposed to fetal bovine serum (FBS) for the indicated incubation times: C (control, no FBS or SDS), 0, 1, 2, 4, and 6 hours, as denoted at the bottom of the gels. Samples are then are then exposed to SDS to release the polymer from the pDNA and electrophoresed in an agarose gel to observe pDNA integrity. Control sample gels are also shown as fetal bovine serum (FBS gel, lane 1) FBS + SDS (FBS gel lanes 2–6), naked pDNA only without the addition of FBS or SDS (pDNA gel, lane 7), and naked pDNA with the addition of FBS and SDS (pDNA gel, lanes 8–12). Other controls samples of polyplex only without the addition of FBS or SDS formed with each polymer beacon are labeled as C for control in the incubation time (**Gd3a** gel, lane 1; **Gd3b** gel, lane 7; **Eu3a** gel, lane 1; **Eu3b** gel, lane 7). It should also be noted here that Band 1 is the position of the sample loading (and also shows the position of polyplexes without FBS and SDS treatment). Band 2 is intact pDNA. Band 3 results from combining both FBS and SDS. Band 4 reveals the degraded pDNA (observed in the pDNA gel lanes 9-12). As shown, the polymer beacons protect pDNA from degradation when exposed to FBS as band 4 is not observed (**Gd3a** gel, lanes 2-6; **Gd3b** gel, lanes 8-12; **Eu3a** gel, lanes 2-6; **Eu3b** gel, lanes 8-12).

6.4.2 Cellular Delivery and Toxicity Studies.

A series of assays were conducted to assess the cellular uptake, toxicity, and transfection efficiency of the polyplexes formulated with the polymer beacons. HeLa cells were transfected with polyplexes formulated with Cy5-pDNA and either **Eu3a**, **Eu3b**, **Gd3a**, or **Gd3b**. Four hours after transfection, cellular uptake efficiency was determined by monitoring the fluorescence intensity of Cy5-labeled pDNA via flow cytometry. Cell viability experiments were conducted by assaying the cells for protein content 48 hours after transfection. Toxicity was assessed by normalizing the results of the protein assay to a control of untreated cells; this is used to calculate the fraction of viable cells in each well. The transfection efficiency was also monitored 8 hours after transfection using a luciferase reporter gene expression assay. These results are reported as relative light units (RLU) per mg of protein. It should be mentioned that these conventional delivery assays only yield pDNA uptake and transcription efficiency but do no yield information about the fate of the polymer (hence the development and study of our intracellular delivery beacons, *vide infra*).

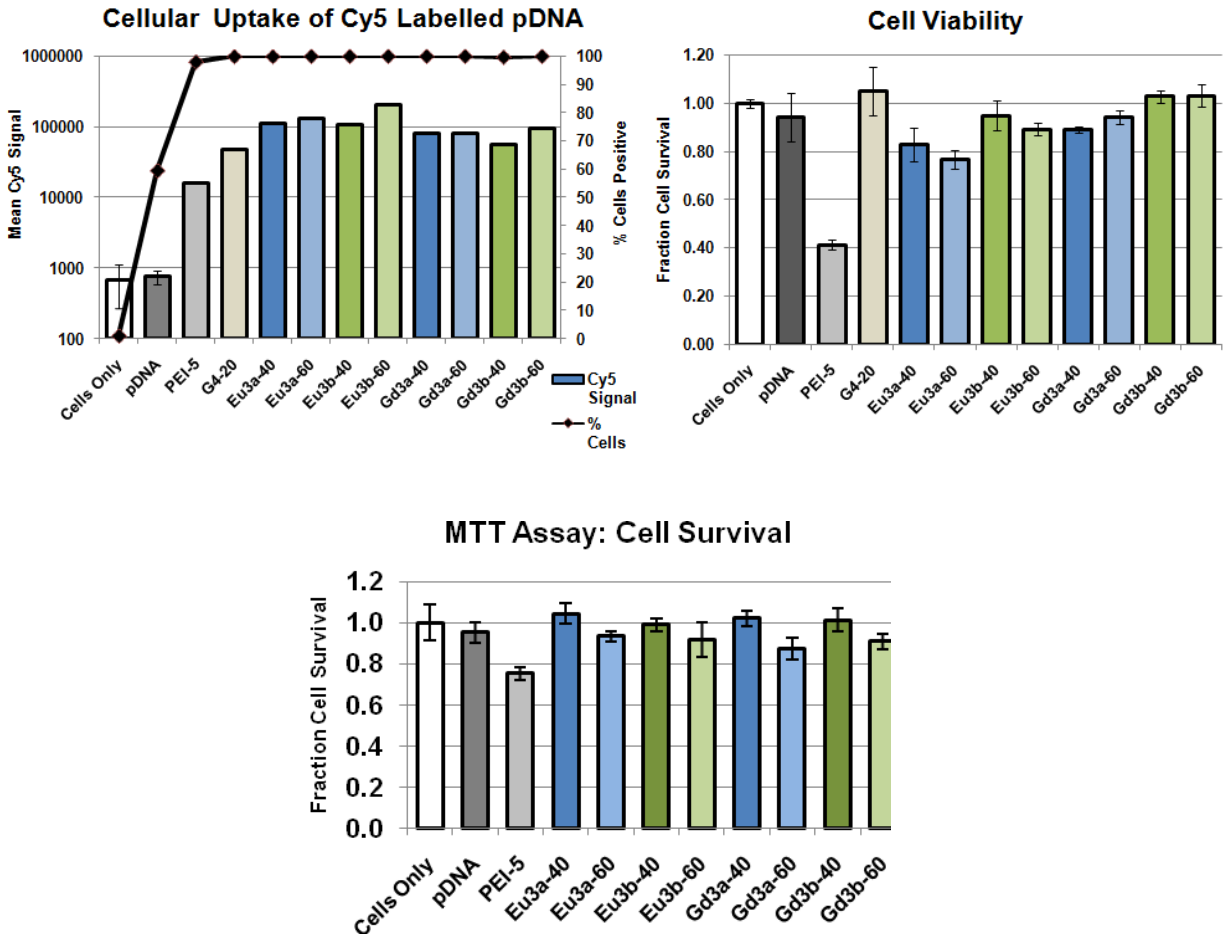

Figure 6-5: Cellular uptake of polyplexes formulated using Cy5-pDNA. The percent of cells (line) containing Cy5 pDNA and mean fluorescence intensity (bar) of Cy5 in a population of at least 30,000 cells. b) Cell viability after exposure to polyplexes using unlabeled pDNA. Viability is reported as a measure of the protein content of a transfected cells normalized to untreated cells. c) Cell viability after exposure to polyplexes using unlabeled pDNA. Viability is reported as a measure of MTT turnover by healthy cells normalized to cells only control. The N/P ratio of the polyplex used is indicated after the polymer name on the x-axis. Polyplexes were formed using the same methodology as DLS studies.

All polyplexes formed with these delivery beacons promoted high cellular uptake while maintaining high cell viability, as depicted in Figure 6-5. In this study, negative controls consisted of cells only and pDNA only while positive controls consisted of polyplexes formed with Jet-PEI at an N/P=5 and polyplexes formed with **G4** at N/P of 20. Polymer **G4** is a

polyamidoamine delivery vehicle previously developed by our group that consists of alternating *meso*-galactaramide units and four ethyleneamine groups.[9, 42] As shown, the new polymer beacons studied herein yielded high pDNA uptake (approximately 100% of cells) and the intensity of Cy5 fluorescence was higher than our positive controls, Jet-PEI and **G4**, indicating that these vehicles are promising for further studies. Figure 6-5 reveals that the toxicity of these structures is very low; even at very high polymer concentrations (high N/P ratios), cell viability remained very high (between 80-100% cell viability) when compared to our positive control Jet-PEI (cell viability only 40% at low N/P=5 in protein assay, 75% in MTT). When the luciferase expression was compared (data not shown), these novel systems displayed slightly lower gene expression (10^7-10^8 RLU/mg) compared to our positive controls, **G4** (>10^9 RLU/mg) and Jet-PEI (10^{10} RLU/mg). However, as previously discussed, these polymer vehicles yielded higher cellular uptake than both positive controls and much lower toxicity than Jet-PEI,[43,44] which could be due to breaking up the amine density along the backbone with hydrophilic chelating units. While we currently do not fully understand the small discrepancy between the uptake and gene expression data, the imaging experiments (*vide infra*) indicate that a much higher fraction of the internalized polyplexes are located in the cytoplasm while a lower fraction is found in the nucleus. Thus, nuclear entry may be the main barrier for gene expression. Indeed, for many forms of nucleic acid therapeutics, such as siRNA, antisense agents, and transcription factor decoys, high cytoplasmic delivery is the ultimate goal.[1-3,6] These novel delivery vehicles could be extremely useful in these therapeutic methodologies.

6.4.3 Cellular Imaging of the Polymer Beacons.

Further investigation of the polymer beacons chelated with luminescent Eu^{3+} was examined via fluorescence microscopy. Hela cells were transfected with polyplexes formulated with FITC-labeled pDNA and either **Eu3a** or **Eu3b** at an N/P ratio of 40. After 24 hours, the cells were fixed and imaged. Figures 6-6 and 6-7 each represent one vertical optical slice obtained by deconvolution of a Z-stack series. The intracellular location of both FITC-pDNA (Figure 6-6a and 6-7a) and the polymers (Figure 6-6b and 6-7b) can be clearly observed. By overlaying the pDNA and polymer images (Figures 6-6c and 6-7c), co-localization can be qualitatively observed by yellow punctuate staining. Most of the staining resulting from FITC-pDNA or Eu^{3+}-polymer luminescence is localized to the cytoplasm and a lower fraction appears in the nucleus. As previously stated, this observation could be a contributing factor to the lower luciferase gene expression but could prove useful in the development of cytoplasmic-targeted nucleic acid therapies. Also, it is clearly noticed that while a small amount of uncomplexed pDNA is present within the cells, a larger fraction of free polymer is observed in the cellular cytoplasm. This could be attributed to the excess used to formulate polyplexes at high N/P ratios, but may indicate premature pDNA release during cellular uptake and early intracellular trafficking (both are concerns in this area but not well understood). Moreover, for **Eu3a**, the intracellular staining pattern is more punctuate whereas diffuse staining is more apparent for **Eu3b**. These data could indicate that **Eu3a** is more localized to endocytic vesicles, whereas **Eu3b** (with more secondary amines per repeat unit) could promote higher endocytic release. These data reveal that our "proof of concept" polymer beacons (and future derivatives) will be useful in understanding intracellular polymer fate as well as elucidating the mechanisms of delivery.

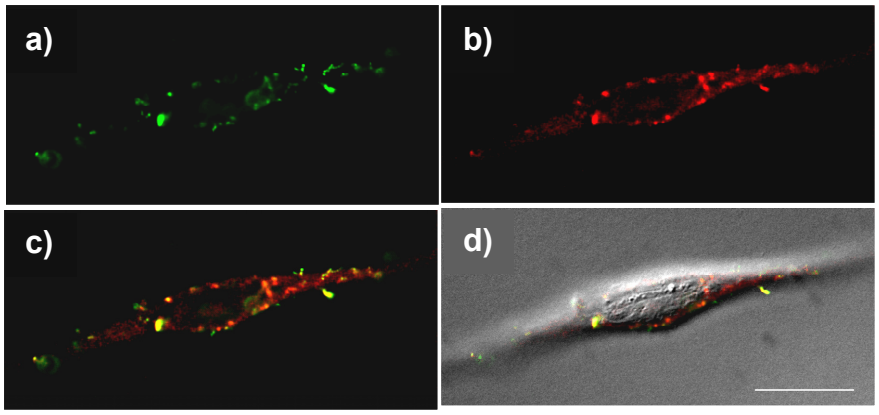

Figure 6-6: Deconvoluted micrographs of a HeLa cell transfected with FITC-pDNA/**Eu3a** polyplexes. a) FITC-pDNA fluorescence (green). b) Eu^{3+} luminescence within the **Eu3a** beacons (red). c) An overlay of the FITC-pDNA and **Eu3a** images. Yellow pixels can be qualitatively used to visualize regions of co-localization. d) An overlay of image c and a DIC image to show contrast of the cell (scale bar = 20μm).

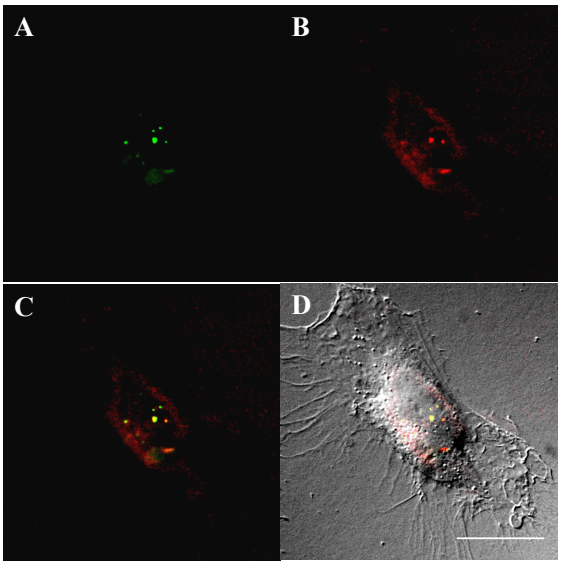

Figure 6-7: Deconvoluted micrographs of a HeLa cell transfected with FITC-pDNA/**Eu3b** polyplexes. a) FITC-pDNA fluorescence (green). b) Eu^{3+} luminescence within the **Eu3b** beacons (red). c) An overlay of the FITC-pDNA and **Eu3b** images. Yellow pixels can be qualitatively used to visualize regions of co-localization. d) An overlay of image c and a DIC image to show contrast of the cell (scale bar = 20μm).

While the Eu^{3+} polymer analogs can be visualized on the nm/μm scale within cells, the Gd^{3+} analogs provide the ability to understand nucleic acid delivery within tissues on the sub-mm scale. The ability of these Gd^{3+} materials to be detected in tissues can be preliminarily examined by determining their relaxivity (r_1) and relaxation rate constants (R_1). This characteristic of the polymers (r_1, determined by plotting $1/T_1$ versus concentration) or polyplexes (R_1, equivalent to $1/T_1$) is used to understand the contrast enhancement of the delivery beacons. We performed the relaxivity experiments on both the free **Gd3a** and **Gd3b** polymers (Figure 6-8a) in solution and commercially available Magnevist™ at two different magnetic field strengths (60 MHz/1.41T and 400MHz/9.4T at 37°C). Furthermore, we tested the ability of polyplex-incorporated beacons to enhance longitudinal water proton relaxation (Figure 6-8b). The relaxivities of both polymers in solution were higher than the clinically-utilized

chelate Gd^{3+}-DTPA (Magnevist™), and a dramatic enhancement was observed at 1.41T, likely due to the slower rotational correlation time of the beacons when compared to Magnevist™. When comparing the longitudinal relaxation rates (R_1) of free polymer to polyplexes at 1.41T (Gd^{3+} concentration is identical) a dramatic relaxivity increase was observed. These results were expected as it is well-known that at low magnetic fields, relaxivity can be significantly enhanced by increasing the rotational correlation time (polyplexes are much larger and have less internal flexibility than free polymer). This difference in relaxivity between free polymer and polyplex could provide a unique method to track nucleic acid release within tissues.

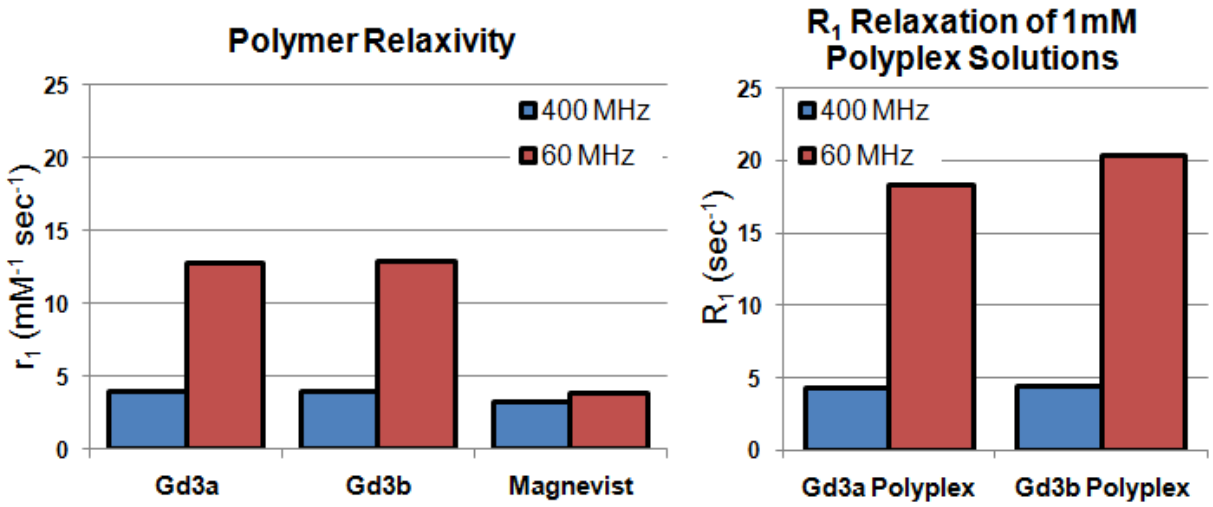

Figure 6-8: a) Relaxivity (r_1) of aqueous solutions containing free polymer (**Gd3a** and **Gd3b** only) and Magnevist™ at 400MHz (9.4 T) and 60 MHz (1.41T). Relaxivity was calculated from four concentrations (5, 2.5, 1.25, 0 mM) of each agent in water. b) The relaxation rate constants (R_1) of polyplexes formed with **Gd3a** and **Gd3b** at a concentration of 1mM at 400MHz (9.4 T) and 60 MHz (1.41T).

To further investigate the MRI contrast capabilities of the Gd^{3+}-chelate materials, HeLa cells were transfected with the polyplexes formulated with **Gd3a** and **Gd3b**. Twenty four hours after transfection, the cells were collected and gravity pelleted into Eppendorf tubes. As shown

in Figure 6-9a, tubes containing live transfected or untrasfected cells were then inserted into a 9.4 Tesla Bruker Avance III NMR equipped with a MR imaging probe (3 cm coil). The samples were subjected to a T_1-weighted pulse sequence, imaged for tissue contrast, and then analyzed for water ^{1}H T_1 values. Untransfected cells that do not contain **Gd3a** or **Gd3b** demonstrate minimal image brightness/contrast (Figure 6-9a image i) and this control cell pellet has a higher T_1 value (2.4 s, Figure 6-9c) than cells transfected with **Gd3a** and **Gd3b** polyplexes. Cells transfected with **Gd3a** and **Gd3b** (Figure 6-9a images ii and iii) show a clear enhancement in the cellular image brightness and substantially lower T_1 values (0.65 s and 0.83 s, respectively). Figure 6-7b shows the T_1–weighted images, using the same pulse conditions as in Figure 6-9a, with 1 mM beacon solutions (Figure 6-9b: ii, iii) versus a PBS control. Because the beacon solutions are so bright relative to the saline control, the control becomes unobservable. This is confirmed by their T_1 analysis at 9.4T which agrees with the MR imaging experiment (T_1 = 2.86 s, 0.22, 0.20, for PBS, **Eu3a**, and **Eu3b**, respectively). These promising data clearly show the potential of our imaging beacons to trace the spatial and temporal delivery of nucleic acids within bulk cells and/or tissues.

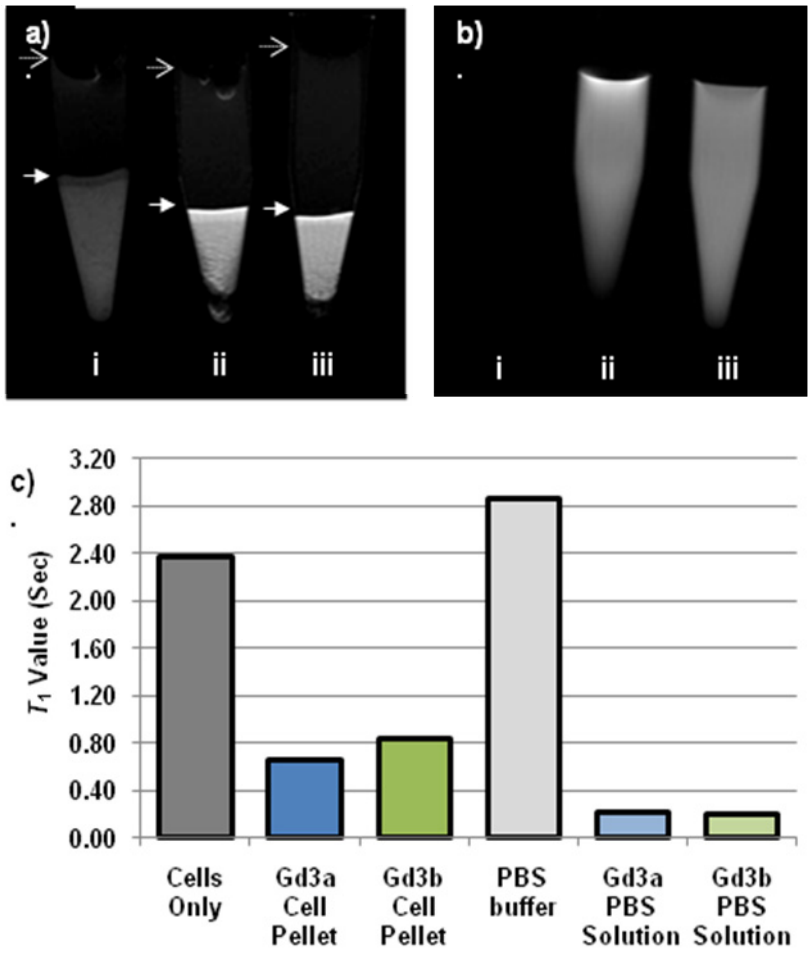

Figure 6-9: MRI data for cells transfected with **Gd3a**/pDNA and **Gd3b**/pDNA polyplexes. Cells were washed thoroughly and allowed to settle into pellets in PBS. a) Transfected cell pellets and controls: i) Pellet of untreated HeLa cells, ii) cell pellets transfected with **Gd3a** polyplexes (N/P = 40), and iii) cells transfected with **Gd3b** polyplexes (N/P = 40). Solid arrows indicate the buffer-cell interface in each sample. Data was acquired on a Bruker Avance III 400MHz spectrometer using an imaging probe (30mm coil) and an inversion recovery pulse sequence (TR/TI/TE = 3500 ms /1200 ms /8.5 ms, FOV = 3 cm). The perturbations at the top of the buffer (dotted arrows) are due to bubbles at the buffer-air interface. The darker spots in the cell pellet are due to cell density gradients. b) MR images of i) PBS buffer, ii) **Gd3a** ($[Gd^{3+}]$ = 1 mM), and iii) **Gd3b** ($[Gd^{3+}]$ = 1 mM) using the same pulse parameters as above. PBS is completely dark in the presence of the detector saturating Gd-containing polymer solutions. c) T_1 quantification of cell and solution samples imaged. Cell samples were allowed to settle into NMR tubes for 24h and then analyzed with an inversion recovery pulse sequence to determine their relaxation times.

6.5 Conclusions

This proof-of-concept study has revealed that our novel nucleic acid delivery beacons show great promise in the development of innovative techniques to understand the delivery, trafficking mechanisms, and fate of nonviral delivery vehicles on differing biological scales. The lanthanide metals offer many unique properties which can be exploited to enhance these imaging techniques. The Eu^{3+}-chelated polymers can be visualized by their luminescence within cultured cells on the nm/μm scale for tracking the intracellular delivery of polyplexes. For larger-scale MR imaging, the paramagnetic nature of the Gd^{3+}-chelated polymers offers a safe and noninvasive probe for following nucleic acid delivery within tissues on the sub-mm scale. These scaffolds have potential for monitoring *in vivo* delivery in a spatial and temporal manner and can be used in-tact (without removal of the imaging probe) due to their non-toxic and effective delivery profile. Indeed, these creative and powerful materials can be broadly applied and exploited by researchers for the discovery of unique nucleic acid drug/vehicle conjugates and to understand and treat many devastating diseases.

6.6 Acknowledgment

The authors would like to thank Dr. Katye Fichter for her help and contribution in the cell culture and microscopy work. Thanks to Dr. Jing Li and Dr. Louis Madsen for their MR imaging expertise and contribution. We sincerely thank the Camille Dreyfus Teacher-Scholar Award program for funding this project. We also thank Prof. Chris Gulgas of Longwood University for his help in performing the relaxivity experiments at 60MHz.

6.7 References

(1) Opalinska, J. B.; Gewirtz, A. M. *Nat. Rev. Drug Discovery* **2002**, *1*, 503 - 514.

(2) Dorsett, Y; Tuschl, T. *Nat. Rev. Drug Discovery* **2004**, *3*, 318 - 329.

(3) Leong PL, *et al. Proc. Natl. Acad. Sci. U. S. A.* **2003**, *100*, 4138-4143.

(4) Heidel, J. D. *et al. Proc. Natl. Acad. Sci. U. S. A.* **2004**, *104*, 5715-5721.

(5) Scherer, L. J.; Rossi, J. J. *Nat. Biotechnol.* **2003**, *21*, 1457-1465.

(6) Davis, M. E.; Chen, Z.; Shin, D. M. *Nat. Rev. Drug Discovery* **2008**, *7,* 771 - 782.

(7) Jeong, J. H.; Mok, H.; Oh, Y. –K.; Park, T. G. *Bioconjugate Chem* **2009**, *20,* 5-14.

(8) Schaffert, D.; Wagner, E. *Gene Ther.* **2008**, *15*, 1131-1138.

(9) Liu, Y.; Reineke, T. M. *J. Am. Chem. Soc.* **2005**, *127*, 3004-3015.

(10) Srinivasachari, S.; Liu, Y.; Zhang, G.; Prevette, L.; Reineke, T. M. *J. Am. Chem. Soc.* **2006**, *128*, 8176-8184.

(11) Srinivasachari, S; Fichter, K. M.; Reineke, T. M. *J. Am. Chem. Soc.* **2008**, *130*, 4618-4627.

(12) Everts, M.; Curiel, D. T. *Curr. Gene Ther.* **2004**, *4*, 337-346.

(13) Thomas, C. E.; Ehrhardt, A.; Kay, M. A. *Nat. Rev. Genet.* **2003**, *4*, 346-358.

(14) Reid, T.; Warren, R.; Kirn, D.; *Cancer Gene Ther.* **2002**, *9*, 979-986.

(15) Karmali, P. P.; Chaudhuri, A. *Med. Res. Rev.* **2007**, *27*, 696-722.

(16) Kodama, K.; Katayama, Y.; Shoji, Y.; Nakashima, H. *Curr. Med. Chem.* **2006**, *13*, 2155-2161.

(17) Kulkarni, R. P.; Wu, D. D.; Davis, M. E.; Fraser, S. E. *Proc Natl Acad Sci USA* **2005**, *102*, 7523-7528.

(18) Sonawane, N. D.; Szoka, F. C.; Verkman, A. S. *J. Biol. Chem.* **2003**, *278*, 44826-44831.

(19) Bartlett, D. W.; Su, H.; Hildebrandt, I. J.; Weber, W. A.; Davis, M. E. *Proc. Natl. Acad. Sci. U. S. A.* **2007**, *104*, 15549-15554.

(20) Pan, D. *et al. J. Am. Chem. Soc.* **2008**, *130*, 9186-9187.

(21) McCarthy JR, Jaffer FA, Weissleder R (2006) A macrophage-targeted theranostic nanoparticle for biomedical applications. *Small* 2:983-987.

(22) Akinc, A.; Langer, R. *Biotechnol. Bioeng.* **2002**, *78*, 503-508.

(23) Malik, N. *et al. J. Control Release* **2002**, *65*, 133-148.

(24) Resch-Genger, U.; Grabolle, M.; Cavaliere-Jaricot, S.; Nitschke, R.; Nann, T. *Nat Methods* **2008**, *5*, 763-775.

(25) Qi, L.; Gao, X. *ACS Nano* **2002**, *2*, 1403-1410.

(26) Sculimbrene, B. R.; Imperiali, B. *J. Am. Chem. Soc.* **2006**, *128*, 7346-7352.

(27) Bünzli, J. –C.; Piguet, C. *Chem. Soc. Rev.* **2005**, *34*, 1048-1077.

(28) Gulgas, C. G.; Reineke, T. M. *Inorg. Chem.* **2008**, *47*, 1548-1559.

(29) Bryson, J. M.; Chu, W. –J.; Lee, J. –H.; Reineke, T. M. *Bioconjugate Chem.* **2008**, *19*, 1505-1509.

(30) Aime, S.; Botta, M.; Fasano, M.; Terreno, E. *Chem. Soc. Rev.* **1998**, *27*, 19-29.

(31) Lauffer, R. B. *Chem. Rev.* **1987**, *87*, 901-927.

(32) Thompson, M. K.; *et al. J. Am. Chem. Soc.* **2003**, *125*, 14274-14275.

(33) Bünzli J. –C. G. *Acc Chem Res* **2006**, *39*, 53-61.

(34) Marriott, G.; Heidecker, M.; Diamandis, E. P.; Yan-Marriott, Y. *Biophys. J.* **1994**, *67*, 957–965.

(35) Poole, R. A.; *et al. Org Biomol Chem* **2007**, *5*, 2055-2062.

(36) Caravan, P.; Ellison, J. J.; Mcmurray, T. J.; Lauffer, R. B. *Chem. Rev.* **1999**, *99*, 2293-2352.

(37) Bryant, H. L.; *et al. J. Magn. Reson. Imaging* **1999**, *9*, 348-352.

(38) Töth, E.; Helm, L.; Kellar, K. E.; Merbach, A. E. *Chem. Eur. J.* **1999**, *5*, 1202-1211.

(39) Caravan, P. *Chem Soc Rev* **2006**, *35*, 512-523.

(40) Chen HH, *et al. Magn. Reson. Med.* **2005**, *53*, 614-620.

(41) Lundqvist, H.; Antoni, G.; Långström, B. *Eur. J. Clin. Pharmacol.* **2007**, *63*, 641-645.

(42) Liu, Y.; Reineke, T. M. *Bioconjugate Chem.* **2006**, *17*, 101-108.

(43) Chollet, P.; Favrot, M. C.; Hurbin, A.; Coll, J.-L. *J. Gene Med.* **2002**, *4*, 84-91.

(44) Wightman, L.; *et al. J. Gene Med.* **2001**, *3*, 362-372.

(45) Prudêncio, M.; *et al. Chem. Eur. J.* **2004**, *10,* 3252-3260.

(46) Rasband, W. S. (1997-2007), U. S. National Institutes of Health, Bethesda.

Chapter 7: Galactaramide-Based Ln-Chelating Polymers for Nucleic Acid Delivery

7.1 Abstract

As discussed in Chapter 6, the delivery of nucleic acids offers great promise in new therapeutics. The *poly*[(oligoamine)amido (Ln^{3+})diethylenetriaminetriacetate] polymers discussed in that chapter offer huge diagnostic potential, but suffer from relatively low expression of the transgene they carry. Here, we have developed a new series of Ln-chelating polymers that feature the high diagnostic potential offered by the previous generation, but also with the potential to promote high gene expression. These new vehicles contain *poly*[(pentaethylenetetraamine)amido (Ln^{3+})diethylenetriaminetriacetate] like their predecessors, however they also contain galacteramide(pentaethylenetetramine)amido (which have been shown to increase transgene expression when combined with oligoamines) repeat units randomly decorated throughout the backbone. We have shown that as the amount of galactose in the backbone increases (from 16% to 50%), the luciferase gene expression in HeLa cells also increases (10^6 to 10^8 RLU/mg, respectively), with little toxicity (cell viability > 80%). We have also found that these polymers promote 20 to 30 times higher cellular uptake using Cy5-labelled pDNA compared with Cy5-pDNA only. Research to visualize these polymers with non-linear microscopy technigues is currently underway.

7.2 Introduction

We demonstrated in Chapter 6 that lanthanides show great promise in monitoring delivery of pDNA in cells at both the microscopic and macroscopic levels with p*oly*[(oligoethyleneamine)amido-(Ln^{3+})diethylenetriaminetriacetate] polymers.[1-2] These polymers show high cellular uptake, high cell viability, and great promise as beacons at sub-cellular levels via florescence microscopy and at the extracellular level via MRI. One drawback of this system is that it has very low transgene expression of genetic materials delivered. Another weakness of this system is that there is no clear degradation pathway, which could limit its potential for clinical applications. With these problems in mind, we set out to design a system with the diagnostic benefits of our first series of p*oly*[(oligoethyleneamine)amido-(Ln^{3+})diethylenetriaminetriacetate] polymers, without the drawbacks stated above.

Previous work carried out by our group[3-6] indicates that integrating carbohydrates into the repeat unit (Figure 1) along an oligoamine backbone can promote high transgene expression with minimal cytotoxicity. Adding a carbohydrate in the backbone is advantageous for several reasons. First, carbohydrates are traditionally considered biocompatible in gene delivery applications, as they have high hydration volumes and few toxic interactions.[7,8] Secondly, binding studies have shown they actually promote pDNA binding through H-bonding interactions.[9,10] Finally, we have also found that the alpha and beta hydroxyl groups on the carbohydrate promote hydrolysis of the proximal amide in neutral media.[11] These three factors make carbohydrates ideal candidates for adding higher transgene expression and degradability into the first generation p*oly*[(oligoethyleneamine)amido-(Ln^{3+})diethylenetriaminetriacetate] polymers.

Scientists studying non-viral delivery beginning to understand the mechanism of transfection and potential drawbacks associated with with the multitude of materials being developed as polymeric nucleic acid carriers.[11-13] Delivery vehicle plays a central role in the mechanisms, kinetics, efficacy, and toxicity of nucleic acid medicines, but little is known about how the vehicle structure affects drug delivery both *in vitro* and *in vivo*. For this reason, diagnostic-therapeutic "theranostic" agents are being developed that provide therapeutic delivery, diagnostic imaging, and the ability to monitor and study treatment efficacy.[14-16] The fist attempts towards this goal were to use fluorescent dyes, but dyes can alter the delivery mechanisms and/or increase side-effects, thus misrepresenting the true delivery mechanisms and location of the native unlabeled materials.[17] This approach is also constrained to one imaging modality, which has huge limitations *in vivo*. The development of new material-based delivery systems that allow monitoring of both the nucleic acid and the delivery vehicle, on the cellular and tissue scales, is essential to improve the delivery efficiency, optimize the vehicle structure, and monitor treatment efficacy in living systems.

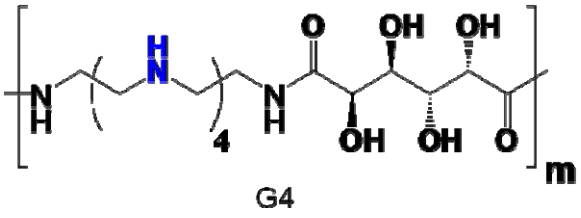

Figure 7-1. Structure of *poly*-galactoamidoamine polymer for nucleic acid delivery.[3]

A new polymer design is needed to benefit from the diagnostic benefits of the first generation lanthanide polymers with the high transgene expression of *poly*-glycoamidoamines. The system that accomplishes this consists of

diethylenetriaminetriacetatebisamideoligoamineamido (DTPA-oligoamine) units similar to the polymers discussed in chapter 6, with galacteramide moieties randomly dispersed throughout the backbone in various ratios. We created four groups of novel copolymers that incorporate different ratios of galactose-oligoamine to DTPA-oligoamine in the backbone (see figure 7-2). Here, we describe the synthesis and properties of these polymers, and their performance *in vitro*.

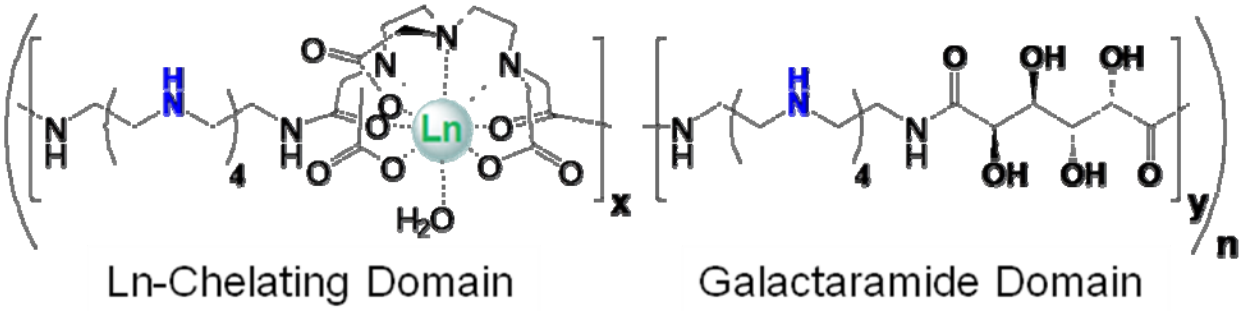

Figure 7-2. Structure of novel Ln-chelating nucleic acid delivery polymers. This polymer features a Ln-chelating domain (x) and a galactose chelating domain (y), in controlled ratios, randomly arranged throughout the polymer backbone. Comonomer ratios are described in nomenclature with lanthanide (Ln), x fraction (X), and y fraction (Y): LnX:Y.

7.3 Materials and Methods

7.3.1 Materials

Diethylenetriaminepentacetic acid and ethyl trifluoroacetate were obtained from Alfa Aesar Chemical Co. (Ward Hill, MA). All other reagents and solvents used in the synthesis were obtained from Aldrich Chemical Co. (Milwaukee, WI) and were used without further purification. Dried solvents were obtained from a MBRAUNN 5-port solvent purification system. N', N'', N''', N'''' – Tetrakis(*tert*-butylcarbomate)pentaethylenehexamine,

diethylenetriaminepentacetic acid bisanhydride (DTPA-BA), and dimethylgalactarate were prepared using standard procedures.[6,18,19]

7.3.2 Cell Culture Materials

Media and supplements were purchased from Gibco/Invitrogen (Carlsbad, CA). HeLa cells were purchased from ATCC (Rockville, MD) and cultured according to specified conditions. Plasmid DNAs: pCMVb and gWiz-Luc, were purchased from PlasmidFactory (Bielefeld, Germany), and Aldeveron (Fargo, ND), respectively. Nuclease free water, Opti-MEM, and DMEM (supplemented with 10% fetal bovine serum (FBS), 100 units/mL penicillin, 100 μg/mL streptomycin, and 0.25 μg/mL amphotericin) and PBS were all purchased from Invitrogen (Carlsbad, CA). Luciferase substrate reagent and cell culture lysis buffer used in the transfection efficiency assays were purchased from Promega (Madison, WI). A Bio-RAD DC protein assay kit used in the viability assay was purchased from Bio-Rad (Hercules, CA). FITC-labeled pDNA and the Cy5 nucleic acid labeling kit were purchased from Mirus (Madison, WI).

7.3.3 Synthesis

Comonomer ratios for specific polymers are described in nomenclature in the form LnX:Y where Ln is the lanthanide (Eu(III) or Gd(III)), X is the (oligoamine)amidodiethylenetriaminetriacetate fraction, and Y is the galacteramidopentaethylenehexamine fraction (Y). Before Ln is chelated in the polymer structure their name is simply denoted by ratio the ratio of (oligoamine)amidodiethylenetriaminetriacetate to galacteramidopentaethylenehexamine; X:Y (See Figure 7-2). A series of ratios was attempet based on starting monomer ratios: 5:1, 3:1, 2:1, and 1:1.

***poly*[penta(oligoamine)amidodiethylenetriaminetriacetate-galacteramidopentaethylenehexamine], 5:1**. N', N'', N''', N'''' – Tetrakis(*tert*-butylcarbamate)pentaethylenehexamine (1.47 g, 2.32 mmol), dimethylgalactarate (0.092 g, 0.38 mmol), and catalytic 4-dimethylaminopyridine (DMAP, 0.141 g, 1.16 mmol) were dissolved in dry methanol (25 ml) at room temperature and allowed to stir for 24h. After this time period, the methanol was removed via evaporation and replaced with 10 ml of DMSO. Diethylenetriaminepentacetic acid dianhydride (0.690 g, 1.93 mmol) dissolved in 15 ml of DMSO was added to the stirring polymer solution and allowed to react for an additional 24h. The reaction mixture was then deposited into a 3500 MW dialysis membrane and dialyzed against methanol (4 x 500 ml) for 24 h to remove all DMSO in the reaction mixture. The dialysis solution was recovered and evaporated to yield a waxy white solid, which was then subjected to BOC group removal using neat trifluoroacetic acid (TFA, 25 ml). After removing the TFA with evaporation, the polymer was dissolved in $NaHCO_3$ buffered water and dialyzed for 24 h against ultrapure water (6 x 3000 mL). The dialyzed solution was recovered and lyophilized to yield a fluffy off white solid, **5:1**. Yield = 436 mg, 33 %. ^{1}H-NMR (D_2O): δ = 2.64 – 3.15 (bm, 100H), 3.2 (bm, 40H), 3.3 (bs, 50H), 3.82 (s, 2H), 4.24 (s, 2H). GPC-MALS: Molecular Weight = 10,966 Da, PDI = 1.16. FTIR (cm^{-1}): 3265.2, 2924.7, 2832.0, 2368.7, 1636.0, 1575.5.

***poly*[tri(oligoamine)amidodiethylenetriaminetriacetate-galacteramidopentaethylenehexamine], 3:1.** N', N'', N''', N'''' – Tetrakis(*tert*-butylcarbamate)pentaethylenehexamine (1.47 g, 2.32 mmol), dimethylgalactarate (0.138 g, 0.58 mmol), and a catalytic amount of DMAP (0.141 g, 1.16 mmol) were dissolved in dry methanol (25 ml) at room temperature and allowed to stir for 24h. After this time period the methanol was

removed via evaporation and replaced with 10 ml of DMSO. Diethylenetriaminepentacetic acid dianhydride (0.621 g, 1.74 mmol) dissolved in 15 ml of DMSO was added to the stirring polymer solution and allowed to react for an additional 24h. The reaction mixture was then deposited into a 3500 MW dialysis membrane and dialyzed against methanol (4 x 500 ml) for 24 h to remove all DMSO in the reaction mixture. The dialysis solution was recovered and evaporated to yield a waxy white solid, which was then subjected to BOC group removal using neat TFA (25 ml). After removing the TFA with evaporation, the polymer was dissolved in $NaHCO_3$ buffered water and dialyzed for 24 h against ultrapure water (6 x 3000 mL). The dialyzed solution was recovered and lyophilized to yield a fluffy off-white solid, **3:1**. Yield = 325 mg, 25 %. ^{1}H-NMR (D_2O): δ = 2.78 – 2.99 (bm, 80H), 3.04 (bs, 12H), 3.16 – 3.45 (bm, 54H), 3.85 (s, 2H), 4.26 (s, 2H). GPC-MALS: Molecular Weight 11,591 Da, PDI = 1.14. FTIR (cm^{-1}): 3271.1, 2922.5, 2848.2, 1628.0, 1575.7.

***poly*[di(oligoamine)amidodiethylenetriaminetriacetate-galacteramidopentaethylenehexamine], 2:1** N', N'', N''', N'''' – Tetrakis(*tert*-butylcarbamate)pentaethylenehexamine (1.47 g, 2.32 mmol), dimethylgalactarate (0.184 g, 0.77 mmol), and a catalytic amount of DMAP (0.141 g, 1.16 mmol) were dissolved in dry methanol (25 ml) at room temperature and allowed to stir for 24h. After this time period the methanol was removed via evaporation and replaced with 10 ml of DMSO. Diethylenetriaminepentacetic acid dianhydride (0.552 g, 1.55 mmol) dissolved in 15 ml of DMSO was added to the stirring polymer solution and allowed to react for an additional 24h. The reaction mixture was then deposited into a 3500 MW dialysis membrane and dialyzed against methanol (4 x 500 ml) for 24 h to remove all DMSO in the reaction mixture. The dialysis solution was recovered and

evaporated to yield a waxy white solid, which was then subjected to BOC group removal using neat TFA (25 ml). After removing the TFA with evaporation, the polymer was dissolved in $NaHCO_3$ buffered water and dialyzed for 24 h against ultrapure water (6 x 3000 mL). The dialyzed solution was recovered and lyophilized to yield a crusty yellow-white solid, **2:1**. Yield = 519 mg, 41 %. ^{1}H-NMR (D_2O): δ = 2.79 – 2.93 (bm, 60H), 3.04 (s, 8H), 3.12 (bs, 8H), 3.22 - 3.64 (bs, 32H), 3.86 (s, 2H), 4.27 (s, 2H). GPC-MALS: Molecular Weight = 9,228 Da, PDI = 1.12. FTIR (cm^{-1}): 3270.6, 2905.2, 2848.8, 3796.2, 1631.1, 1577.1.

***poly*[(oligoamine)amidodiethylenetriaminetriacetate-galacteramidopentaethylenehexamine], 1:1** N', N'', N''', N'''' – Tetrakis(*tert*-butylcarbomate)pentaethylenehexamine (1.47 g, 2.32 mmol), dimethylgalactarate (184 mg, 0.77 mmol), and catalytic DMAP (0.141mg, 1.16 mmol) were dissolved in dry methanol (25 ml) at room temperature and allowed to stir for 24h. After this time period, the methanol was removed via evaporation and replaced with 10 ml of DMSO. Diethylenetriaminepentacetic acid dianhydride (0.552 g, 1.55 mmol) dissolved in 15 ml of DMSO was added to the stirring polymer solution and allowed to react for an additional 24h. The reaction mixture was then deposited into a 3500 MW dialysis membrane and dialyzed against methanol (4 x 500 ml) for 24 h to remove all DMSO in the reaction mixture. The dialysis solution was recovered and evaporated to yield a waxy white solid, which was then subjected to BOC group removal using neat TFA (25 ml). After removing the TFA with evaporation, the polymer was dissolved in $NaHCO_3$ buffered water and dialyzed for 24 h against ultrapure water (6 x 3000 mL). The dialyzed solution was recovered and lyophilized to yield a flakey white solid, **1:1**. Yield = 0.393 g, 32 %. ^{1}H-NMR (D_2O): δ = 2.52 – 2.98 (bm, 40H), 3.04 - 3.32 (bm, 18H) 3.86 (s, 2H), 4.23 (s,

2H). GPC-MALS: Molecular Weight = 9,010 Da, PDI = 1.12. FTIR (cm^{-1}): 3271.4, 2924.2, 2370.0, 1631.1, 1576.3.

General Procedure for chelation of lanthanide with polymer

The amount of material used in each polymerization varied based on the amount of material available from previous steps. For example, 0.5 mmol aliquots of each unchelated polymer (based on molar amount of chelate per repeat unit), **5:1, 3:1, 2:1**, and **1:1**, were dissolved in 5 ml of ultrapure water at room temp. Next, 0.5 mmol of $LnCl_3$ (either $EuCl_3$ or $GdCl_3$) was dissolved in 2 ml of water and dripped into the respective polymer solution in 3 separate aliquots. The pH was adjusted to pH = 6 after each aliquot addition with $NaHCO_3$. The solution was allowed to stir for 2 h and then was dialyzed in a 3500 Da MWCO bag against ultrapure water (4 x 3000 ml) for 24 h. Dialyzed solutions were lyophilized to yield fluffy off-white polymers.

Eu5:1

Yield = 94.0 mg, 68.2%. GPC-MALS: Molecular Weight = 10,035 Da, PDI = 1.19.

FTIR (cm^{-1}): 3263.9, 2918.7, 2849.1, 2340.4, 1592.7.

Elemental Analysis; Theoretical: **C** 44.79%; **Eu** 5.45%; **H** 7.81%; **N** 19.59%.

Actual: **C** 30.98%; **Eu** 11.8%; **H** 6.45%; **N** 12.59%

Eu3:1

Yield = 71.8 mg, 65.3%. GPC-MALS: Molecular Weight = 11,931, PDI = 1.13.

FTIR (cm^{-1}): 3264.3, 2918.9, 1848.9, 2334, 1592.8.

Elemental Analysis; Theoretical: **C** 43.76%; **Eu** 7.69%; **H** 7.55%; **N** 19.14%.

Actual: **C** 30.87%; **Eu** 12.8%; **H** 6.35%; **N** 12.85%

Eu2:1

Yield = 130.3 mg, 61.4 %. GPC-MALS: Molecular Weight = 11,676 Da, PDI = 1.13.

FTIR (cm^{-1}): 3261.5, 2867.4, 2854.9, 2368.9, 1580.2

Elemental Analysis; Theoretical: **C** 42.85%; **Eu** 9.68%; **H** 7.32%; **N** 18.74%.

Actual: **C** 32.18%; **Eu** 16.0%; **H** 6.54%; **N** 13.42%

Eu1:1

Yield = 43.4 mg, 61.4%. GPC-MALS: Molecular Weight = 5,712 Da, PDI = 1.13.

FTIR (cm^{-1}): 3260.3, 2920.6, 2848.6, 1586.2.

Elemental Analysis; Theoretical: **C** 41.31%; **Eu** 13.07%; **H** 6.93%; **N** 18.06%.

Actual: **C** 30.37%; **Eu** 38.4%; **H** 6.93%; **N** 18.06%

Gd5:1

Yield = 98.7 mg, 71.6%. GPC-MALS: Molecular Weight = 12,444 Da, PDI = 1.23.

FTIR (cm^{-1}): 3260.8, 2920.1, 2874.8, 2340.0, 1579.5.

Elemental Analysis; Theoretical: **C** 44.70%; **Gd** 7.77%; **H** 5.63%; **N** 19.55%.

Actual: **C** 33.72%; **Gd** 16.4%; **H** 6.54%; **N** 14.26%

Gd3:1

Yield = 68.2 mg, 62.0%. GPC-MALS: Molecular Weight = 12,332 Da, PDI = 1.18. Elemental FTIR (cm^{-1}): 3264.9, 2919.6, 2848.9, 2340.7, 1592.5.

Elemental Analysis; Theoretical: **C** 43.65%; **Gd** 8.01%; **H** 6.85%; **N** 19.09%.

Actual: **C** 31.93%; **Gd** 12.0%; **H** 6.85%; **N** 13.32%

Gd2:1

Yield = 146.1 mg, 75.3%. GPC-MALS: Molecular Weight = 9,339 Da, PDI = 1.18.

FTIR (cm^{-1}): 3259.8, 2919.8, 2848.6, 2326.7, 1593.5.

Elemental Analysis; Theoretical: **C** 42.71%; **Gd** 9.98%; **H** 7.30%; **N** 18.68%.

Actual: **C** 33.46%; **Gd** 11.6%; **H** 6.93%; **N** 13.68%

Gd1:1

Yield = 48.1 mg, 67.4%. GPC-MALS: Molecular Weight = 8,295 Da, PDI = 1.26.

FTIR (cm^{-1}): 3260.4, 2920.4, 2874.1, 2367.4, 1586.7.

Elemental Analysis; Theoretical: **C** 41.36%; **Gd** 13.67%; **H** 6.90%; **N** 18.07%.

Actual: **C** 32.13%; **Gd** 8.2%; **H** 6.59%; **N** 12.19%

7.3.4 Polymer Characterization.

The molecular weight and polydispersity for polymers **5:1, 3:1, 2:1**, **1:1, Eu5:1, Eu3:1, Eu2:1**, **Eu1:1**, **Gd5:1, Gd3:1, Gd2:1**, and **Gd1:1,** were measured with a Viscotek GPCmax instrument equipped with a $GMPW_{xl}$ (aqueous phase, Tosoh Biosciences, New York, NY) column coupled to a triple detection system (static light scattering, viscometry, and refractive index) as shown in Table 3. A solution of 0.5M sodium acetate containing 20% acetonitrile was used as the mobile phase. Each sample was dissolved in the mobile phase, injected into the instrument (100uL loop, 8-12mg/mL), and eluted at a flow rate of 0.80 ml/min. A monodisperse polyethylene oxide standard weighing 22 kDa was used as a reference standard for these experiments. NMR spectra were acquired on a Bruker AV-400 MHz spectrometer. ^{1}H NMR data are reported as follows: chemical shift (δ ppm), multiplicity (s = singlet, d = doublet, t = triplet, q = quartet, m = multiplet, bs = broad singlet, bm = broad multiplet), and the peak integration. It should be mentioned that neither ^{1}H nor ^{13}C NMR data could be collected for **Eu5:1**, **Gd5:1**, **Eu3:1**, **Gd3:1**, **Eu2:1**, **Gd2:1**, **Gd1:1**, and **Eu1:1**, due to the paramagnetic nature of these materials. These materials were studied with elemental analaysis. IR spectra were measured on a Perkins-Elmer FTIR.

7.3.5 Thermo Gravimetric Analysis (TGA)

In hopes of relating thermal degradation to polymer composition, polymers **Gd5:1**, **Gd3:1**, **Gd2:1**, and **Gd1:1**, were studied for their thermal stability profiles using TGA. Sample sizes between 5 – 10 mg were deposited on to a tared platinum sampling pan and loaded into the TGA. Sample degradation was monitored from 25°C to 800°C. Samples were compared for degradation similarities based upon their comonomer ratio composition.

7.3.6 Gel Electrophoreses Shift Assay

Polymers **Gd5:1**, **Gd3:1**, **Gd2:1**, **Gd1:1**, **Eu5:1**, **Eu3:1**, **Eu2:1**, and **Eu1:1**, were studied for their ability to bind pDNA using gel electrophoreses. Each polymer was dissolve in nuclease-free water (Gibco, Carlsbad, CA). Next, solutions of pDNA (1μg, 0.1μg/μL) were titrated with equal volumes of polymer solutions to form polyplexes at N/P ratios varying from 0-50 (N = secondary amines on polymer, P = phosphate groups on the pDNA) and allowed to incubate for 30min at room temperature. Loading buffer (2μl) was added to each of the prepared polymer-pDNA solutions (Blue Juice, Invitrogen, Carlsbad, CA). The gel composition was agarose 0.6% w/v, which contained ethidium bromide (0.6 μg/mL) and was prepared in TAE buffer (40 mM Tris-acetate, 1 mM EDTA). Aliquots (20ul) of each polyplex solution were deposited into each well. An applied field of 60V was used to facilitate pDNA migration. Polymer-pDNA complex formation is illustrated by lack of pDNA band migration in the electrophoretic field, illustrating charge neutralization of the DNA phosphates.

7.3.7 Polymer Relaxivity

T_1 measurements were carried out on Varian 400-MR NMR (9.4T) and Anasazi FT-NMR 60MHz (1.41T) NMR spectrometers. The longitudinal relaxation time (T_1) for each solution was measured using an inversion recovery pulse sequence (180° – d_t – 90° – acquire) at 298K. Arrayed data [$n(d_t) = 10$] was processed using Acorn NUTS software and fit to a three-parameter model. The inverse of the T_1 data was used to determine the longitudinal relaxation rate constants (R_1) imparted by the polyplexes. Solution concentration data for beacons **Gd5:1**, **Gd3:1**, **Gd2:1**, and **Gd1:1**, were used to calculate relaxivity ($\mathbf{r_1}$) by generating a curve fit to $(1/T_1) = [Gd^{3+}](r_1) + b$, where $b = (1/T_1)$ for the working solvent (water).

7.3.8 Cellular uptake in HeLa cells

Flow cytometry studies were carried out in collaboration with Patrick McLendon, a member of the Reineke group. Twenty-four hours prior to transfection, HeLa cells were seeded in 6 well plates at a density of 250,000 cells/well and incubated in supplemented DMEM (10% FBS) at 37°C and 5 % CO_2. Polyplexes were formulated by adding 250μL solutions of each polymer dissolved in water (concentration calculated based on N/P ratios of 40 and 60) to 5 μg of Cy5-labeled pDNA (250 μL solution). Polyplexes of Jet-PEI and **G4** were formulated using the same methodology. Polyplexes were incubated at room temperature for 1 hour. Just prior to transfection, 1mL of Opti-MEM was added to each solution. Cells were aspirated of old media, washed with 1mL PBS, and the appropriate polyplex solution was added to each well. Cells were then incubated at 37°C under a 5% CO_2 atmosphere for 4 hours. The cell suspensions were then prepared for analysis as previously described. HeLa cell suspensions were analyzed on a FACS Canto II flow cytometer equipped with a 633 nm helium-neon laser. Mean Cy5 fluorescence intensity was measured using the appropriate forward and side scatter gates. A control of untransfected cells was used to create a gate such that less than 1% of cell-associated autofluorescence is detected in the Cy5 channel. This gating strategy was used for subsequent samples of transfected cells to determine the percent of cells transfected.

7.3.9 Luciferase assay in HeLa cells

For gene expression analysis, polyplexes were formulated in an identical manner as above except with GWiz-luc pDNA and allowed to transfect cells for 48 hr prior to assaying for luciferase activity. Cell viability was characterized by measuring the amount of protein in cell

lysates using a Bio-Rad DC protein assay kit (Hercules, CA) in triplicate. Viability is reported as the fraction of protein in each sample normalized to a control of untransfected cells.

7.4 Results and Discussion

The design of these polymers was inspired by the characteristics of previous successful cationic nucleic acid delivery vehicles. The amine-containing co-monomer precursors were synthesized using a series of protection/deprotection reactions previously published by our lab to obtain **1** (Scheme 1).[6] These oligoamines were first polymerized with the appropriate portions of dimethylgalactarate, in methanol for 24h at RT. Next, diethylenetriaminepentaacetic acid bisanhydride was added to this reaction mixture in dimethylsulfoxide at room temperature for 24 hours to form four new random copolymer structures, consisting of protected oligoethyleneamine, galactaramide, and pendant carboxylates from the anhydride ring opening during polymerization, in various monomer ratios (Scheme 7-1). The Boc protecting groups were removed via conventional methods yielding the unchelated polymers **5:1**, **3:1**, **2:1**, and **1:1**. NMR analysis indicated that intended monomer ratios used for polymerization carried over into the unchelated polymer structure (Figure 7-3). The deprotected precursors were then chelated with the chloride salts of Eu^{3+} and Gd^{3+}, while maintaining a neutral pH, using $NaHCO_3$. This chelation is confirmed via shifting of the FT-IR carbonyl stretch absorbance bands from ~1575 cm^{-1} to between 1580 cm^{-1} and 1592 cm^{-1}.

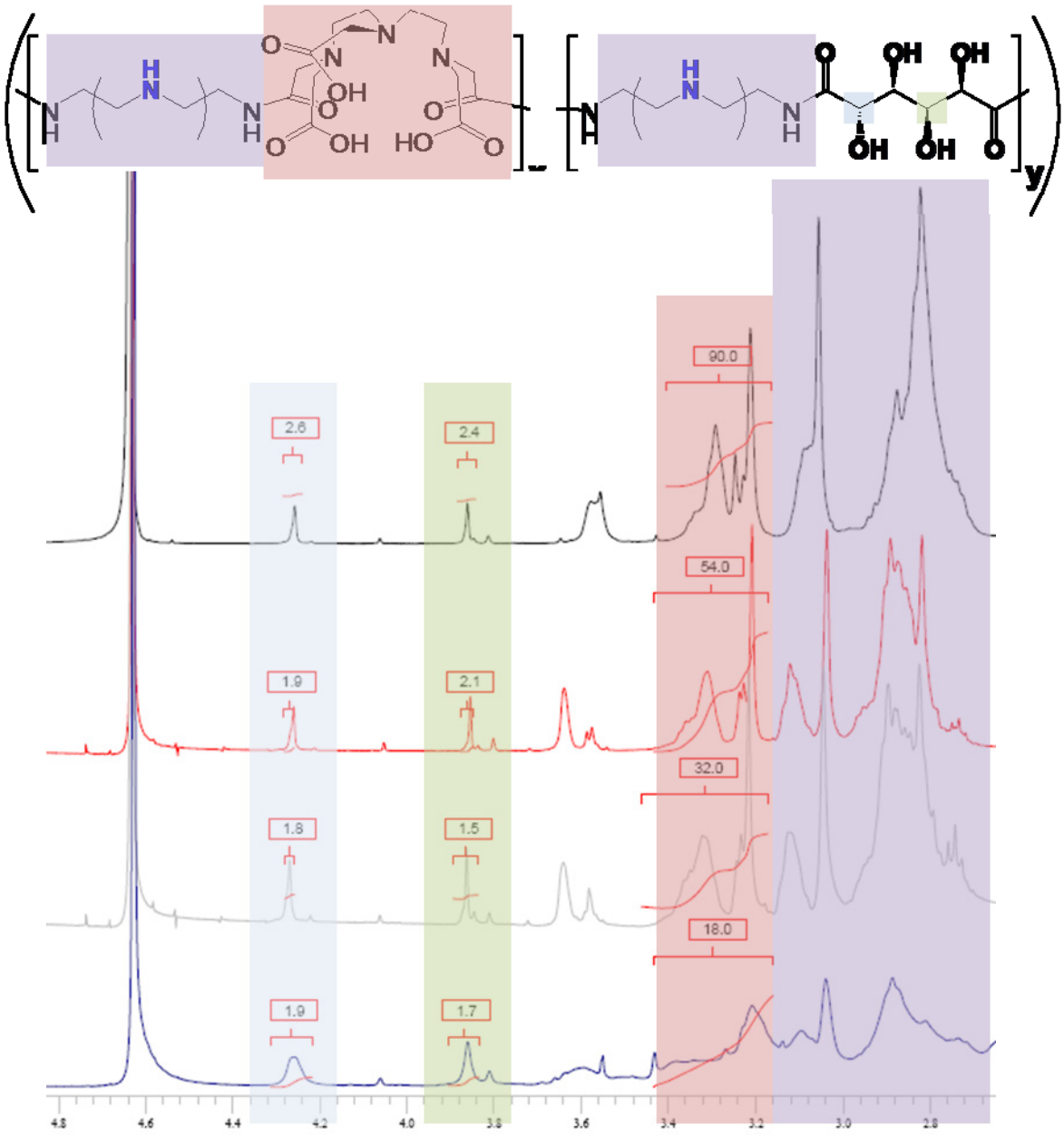

Figure 7-3. NMR comparison to determine galacteramide content relative to diethylenetriaminetriacetic acid diamide content.

Elemental analysis (see Materials and Methods) indicates that Ln levels are significantly higher than theoretical values predict. Unfortunately, it seems that significant degradation is occurring in the dialysis step after chelation. After galactaramide hydrolysis, it seems a

significant amount of cleaved oligomer is washing out of the dialysis bag. This elemental analysis data is further supported by the molecular weight loss observed in later experiments (*vide infra*). Because of the degradation happening during this step, dialysis is likely not a viable option for purification of these chelated polymers in future work. Non-aqueous purification of centrifugal membrane purification might indeed be a more successful option.

The unchelated and Ln-chelated polymers were analyzed via GPC using a triple detection system (refractive index, static light scattering, viscometry) to determine the weight averaged molecular weight (M_w) and polydispersity index (M_w/M_n) (Table 7-1 and Figure 7-4). Molecular weight varied between the polymer structures **5:1, 3:1, 2:1**, **1:1, Eu5:1, Eu3:1, Eu2:1**, **Eu1:1**, **Gd5:1, Gd3:1, Gd2:1**, and **Gd1:1**. This is likely due to the amount of hydrolysable amide bonds in each structure, which are attributed to the galactaramide linkages,[7] and can hydrolyze during the dialysis purification they are subjected to. This is also likely why very low yields were recovered after each step. Possible degradation via hydrolysis is further confirmed by the loss of M_w (determined by GPC-light scattering, Figure 7-4) between the non-chelated **1:1** polymer and its chelated analogues (Table 7-1).

Scheme 7-1. Synthesis of Ln-DTPA-*poly*-galactoamidoamine copolymers.[a]

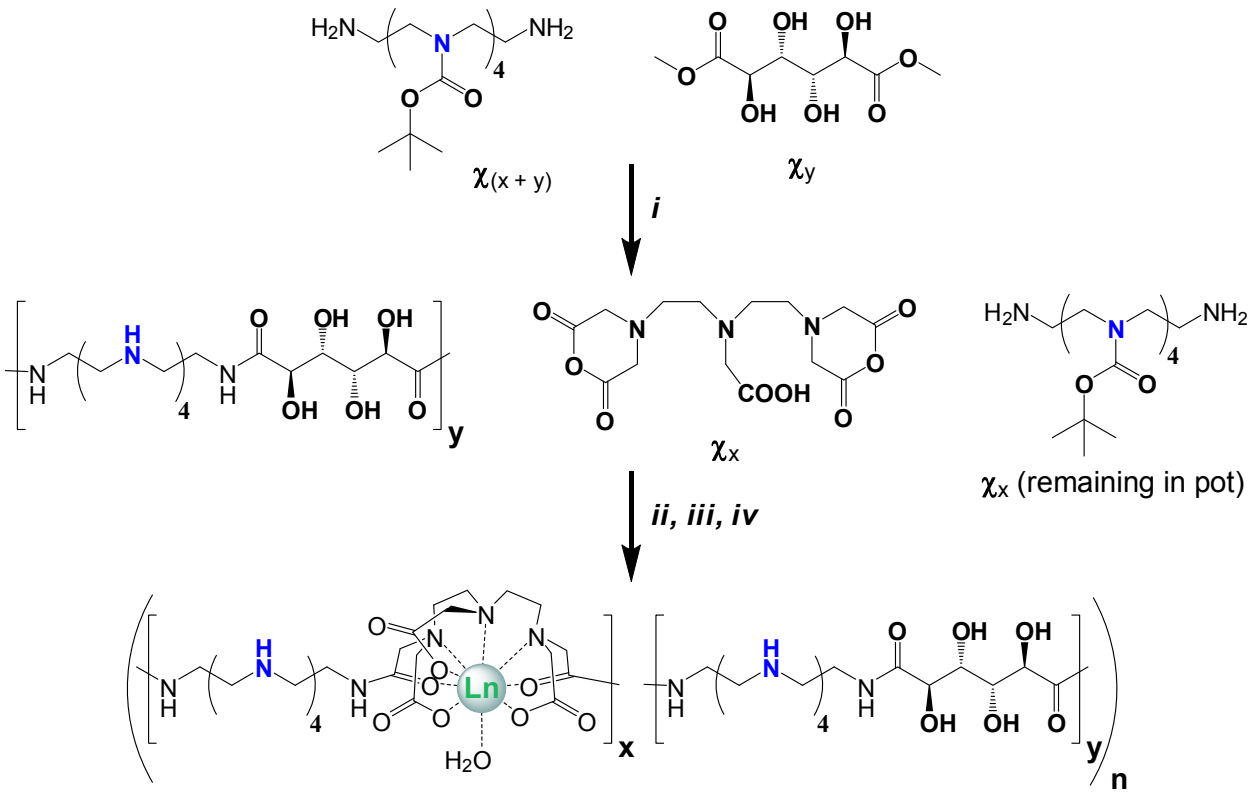

[a] ***i)*** Reagents 1 and 3, DMAP, MeOH, 24h RT. followed with reagents 1, 2, and 3, DMAP, DMSO, 24h, RT. ***ii)*** TFA neat, 1h, RT, ***iii)*** $LnCl_3$, $NaHCO_3$, H_2O, 1h. χ represents the molar ratios of each monomer, which carriy through to the final structure.

Polymer	M_w (Da)	M_w/M_n
5:1	10,966	1.16
3:1	11,591	1.14
2:1	9,228	1.12
1:1	9,010	1.12
Gd5:1	12,444	1.23
Gd3:1	12,332	1.18
Gd2:1	9,339	1.18
Gd1:1	8,205	1.23
Eu5:1	10,035	1.10
Eu3:1	11,931	1.13
Eu2:1	11,676	1.13
Eu1:1	5,712	1.13

Table 7-1. Polymer M_w and PDI as determined by GPC light scattering.

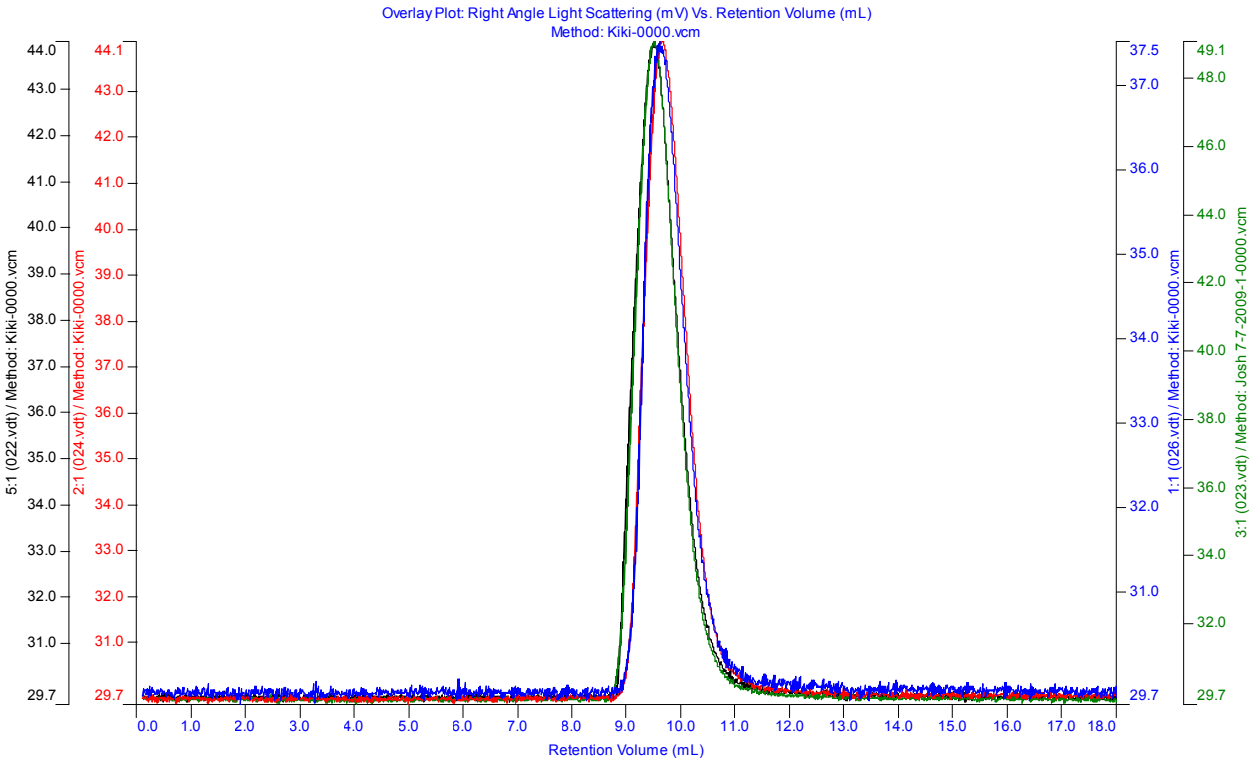

Figure 7-4. GPC right angle light scattering traces of **5:1** (black)**, 3:1** (red)**, 2:1** (blue), and **1:1** (green); show a monomodal light scattering trace for each polymer sample.

Because of the large amount of degradation observed between the chelated and unchelated polymers in the GPC experiments and in attempt to try to understand the stability differences between the random copolymers, especially relating to the amount of galactose comonomer, the polymers were evaluated with thermo gravimetric analysis (Figure 7-5). **Gd5:1, Gd3:1, Gd2:1**, and **Gd1:1** were analyzed between 35 ^{o}C and 800 ^{o}C. All polymers, especially samples with higher amounts of Gd-DTPA comonomer, showed two distinct weight loss regions. The first transition occurs around 300 ^{o}C and is likely related to the amount of galactose comonomer since the amount of degradation at this temperature increases as a function of galactose molar ratio (**Gd5:1 → Gd1:1**). The second degradation occurs at 475 ^{o}C and is likely related to the Gd-DTPA comonomer. The final weight percentage (20% - 30%) is likely comprised of non-thermally degradable remnants, probably gadolinium oxides. Interestingly, the

"char" remaining in the TGA pan is a white fluffy powder which indicates these likely are Ln-oxides.

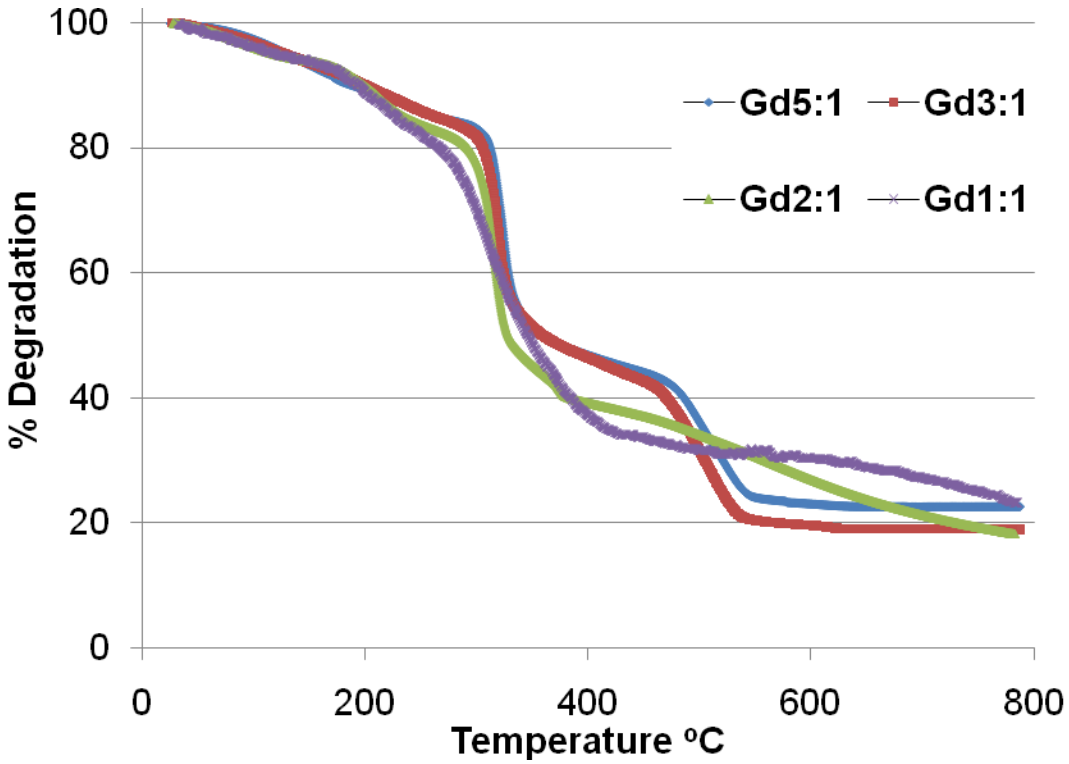

Figure 7-5. TGA profiles for family of Gd-containing polymers. Degradation traces for the Gd-chelated polymers Gd5:1 (blue), Gd3:1 (red), Gd2:1 (green), and Gd1:1 (purple).

The polymers, **Gd5:1, Gd3:1, Gd2:1**, and **Gd1:1** were examined for their ability to complex pDNA using a gel shift assay (Figure 7-6). Polyplexes were formulated at N/P ratios (N = the polymer secondary amine number and P = the DNA phosphate number) between 0 and 50 before being electrophoresed in an agarose gel. N/P ratio was calculated based on the molecular weight for the total repeat unit. In the case of Gd5:1, each (pentaethylenetetraamine)amido-(Gd^{3+})diethylenetriaminetriacetate unit has a MW = 744.92 Da and each galacteramideamidopentaethylenetetramine has an MW = 450.55 Da. There are five

(pentaethylenetetraamine)amido-(Gd^{3+})diethylenetriaminetriacetate units and one galacteramideamidopentaethylenetetramine unit per repeat, giving a MW = 4175.2 Da per repeat unit. This value and the total amount of secondary amines in the repeat unit (24) are used to calculate N/P. Polymers **Gd5:1, Gd3:1, Gd2:1**, and **Gd1:1** began to hinder gel migration at N/P ratio of 0.5, and pDNA migration was mostly suppressed between an N/P of 20 – 30 in all cases except for **Gd1:1**. With these polymers, the N/P ratio needed to fully inhibit gel migration of pDNA was slightly higher than expected when compared to similar polyamidoamine vehicles created in our laboratory.[3-6] The bulkiness of the lanthanide chelate and the presence of the carboxylate groups could have an effect on suppressing the binding through steric hindrance and lower cationic charge on the polymer backbone. As carbohydrate ratio increases in the polymer backbone, gel binding seems to decrease. Based on H-bonding interactions from galactaramide, quite the opposite was expected, but the small sizes of these polymers likely are the limiting parameter in binding. As observed with the first generation polymers, the non-chelated polymers (**5:1** and **3:1**, data not shown) do not bind with pDNA, likely due to their zwitterionic nature at physiological pH, imparted by their free carboxylate arms.

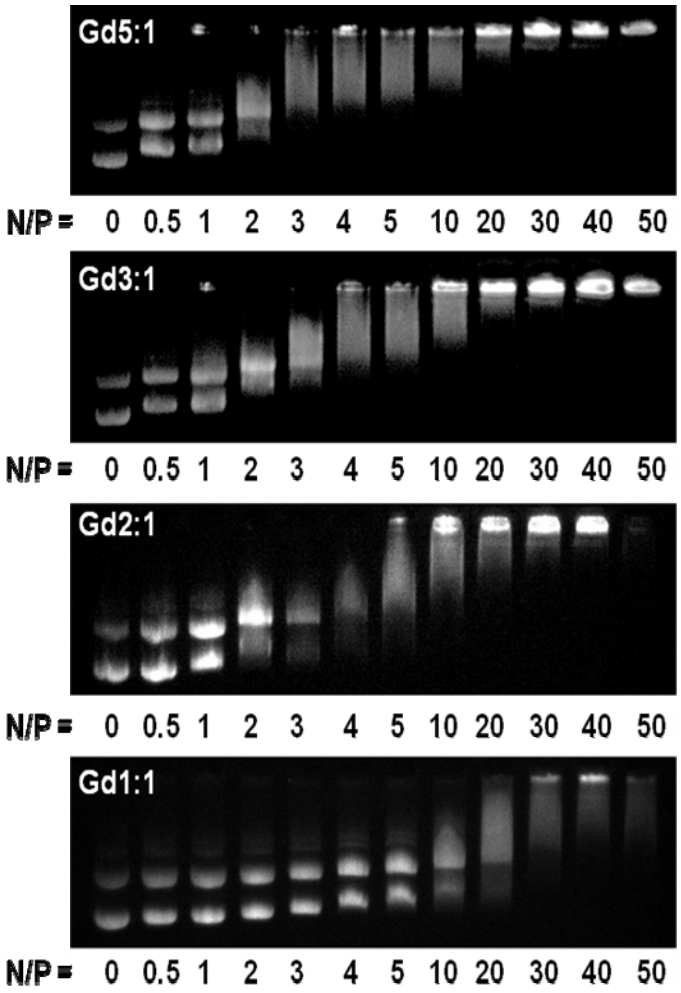

Figure 7-6. Gel binding of polymers **Gd5:1, Gd3:1, Gd2:1**, and **Gd1:1**.

After finding that these novel polymers can bind pDNA and are likely easily degraded via hydrolysis, we wanted to probe their biological properties. Human cervical cancer (HeLa) cells were transfected with Cy5 labeled pDNA that was complexed with the various novel Ln-containing polymers. After 4 h these cells were trypsinized, analyzed on a FACS Canto II flow cytometer, and compared to both positive (G4 polyplexes (Figure 7-1), linear PEI polyplexes) and negative controls (cells only, DNA only). It seems that as the ratio of galactose to DTPA increases, so does the cellular uptake of the related polyplexes (Figure 7-7). In fact, the **Ln1:1** polymer family seems to have twice as much Cy5 intensity as their non-galactose-containing

analogs described in Chapter 6 (**Gd3b** and **Eu3b**). This exciting trend would likely continue to approach the uptake of G4, if higher χ galactaramide to χ DTPA ratio polymers are synthesized.

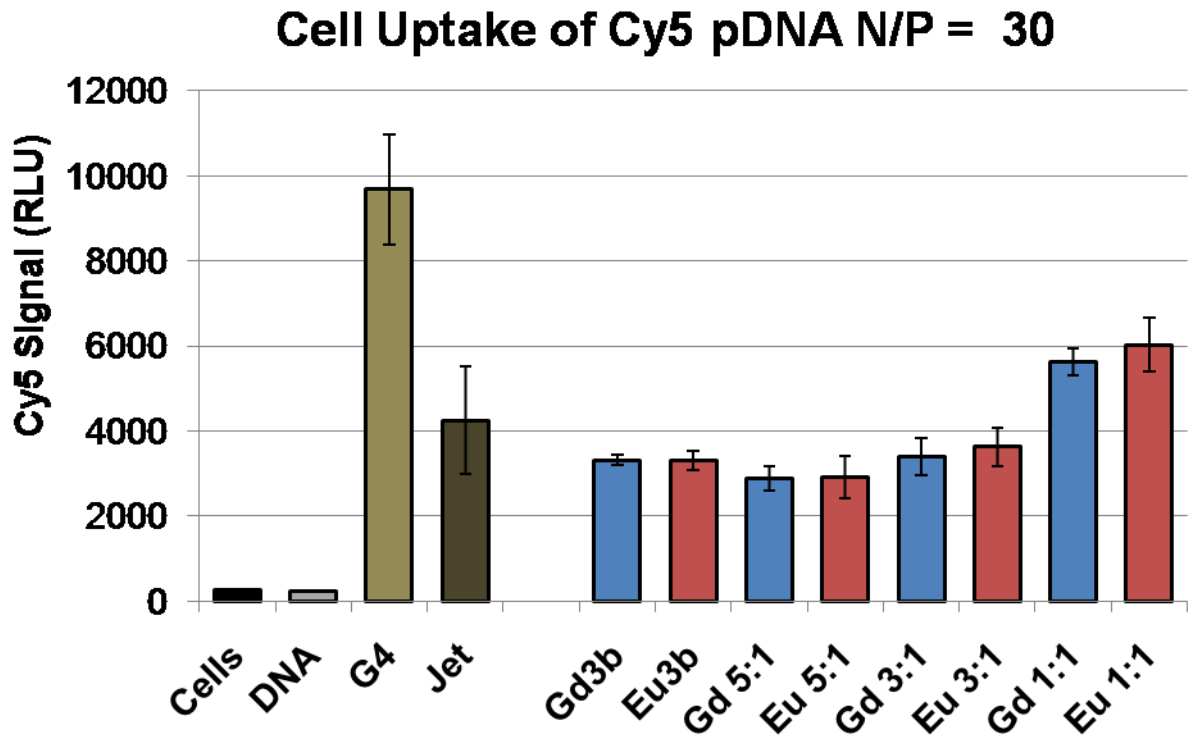

Figure 7-7. Cellular uptake of polyplexes at N/P = 30. Cells were transfected with Cy5 labeled pDNA and analyzed for cellular uptake via flow cytometry after 4h. Controls are pDNA only (DNA), PEI polyplexes (PEI, N/P = 5), and G4 (N/P = 30).

The whole impetus for creating these new *poly*[galacteramide(pentaethylenetetramine)amido(pentaethylenetetraamine)amido (Ln^{3+})diethylenetriaminetriacetate] (PGAALnDTPAA) polymers was to retain the same diagnostic enhancement potential of the generation one series (chapter 6), but to increase their ability to promote transgene expression. To suppoirt if our hypothesis that incorporating carbohydrates in the polymer backbone would improve transfection efficiency by promoting polymer degradation, a luciferase expression assay was performed. HeLa cells were treated with

pDNA encoded for the luciferase gene and allowed to incubate for 48h, after which they were lysed and assayed for luciferase expression. The results followed a very similar trend to the cellular uptake, and indeed supported our hypothesis. G4 is among the better transfection agents currently being used, which makes the similar high expression imparted by **Gd1:1** and **Eu1:1** extremely exciting (Figure 7-8). It is clear that PEI has very high gene expression, but also shows high toxicity. It seems the biocompatibility of G4 also carries over to the PGAALnDTPAA random copolymers, as greater than 80% cell viability is noted for all polymers, based on a protein content assay. Indeed, these results indicate that these random copolymers could show high potential as theranostic agents.

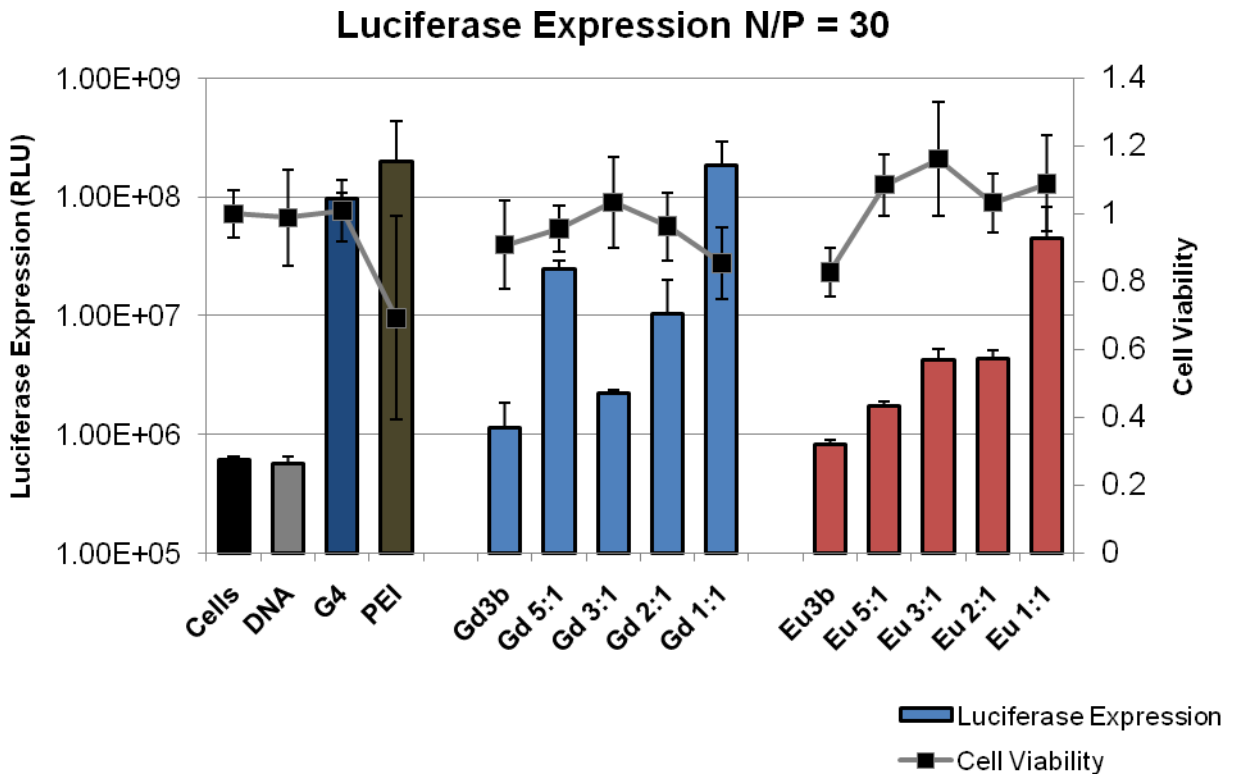

Figure 7-8. Luciferase expression in cells transfected with polyplexes. Cells were transfected with a plasmid encoded with a luciferase gene, lysed after 24h, and assayed for luciferase activity. Controls are pDNA only (DNA), PEI polyplexes (PEI, N/P = 5), and G4 (N/P = 30).

Relaxation enhancement is an important parameter to consider when examining the efficacy of a contrast agent. In attempt to quantify this important attribute, the novel copolymers were dissolved in water and subjected to T_1 analysis at 400 MHz (Figure 7-9). Interestingly, the relaxivity changes significantly, depending on the structure of the random copolymers. **Gd5:1** and **Gd3:1** both show the greatest enhancement. As galactose increases in the polymer backbone, the relaxivity decreases. It is most likely due to the pronounced degradation occurring in the dialysis step following chelation. Significant amounts of Gd-oligomer may be washing out which leads to unreliable calculations when preparing solutions for this experiment. This is attested in the Ln-content analysis where Gd(III) content is low compared to theoretical values, which is likely the reason for its low relaxivity. The relaxivity of these polymers is certainly above the threshold level required for effective contrast enhancement in clinical applications.

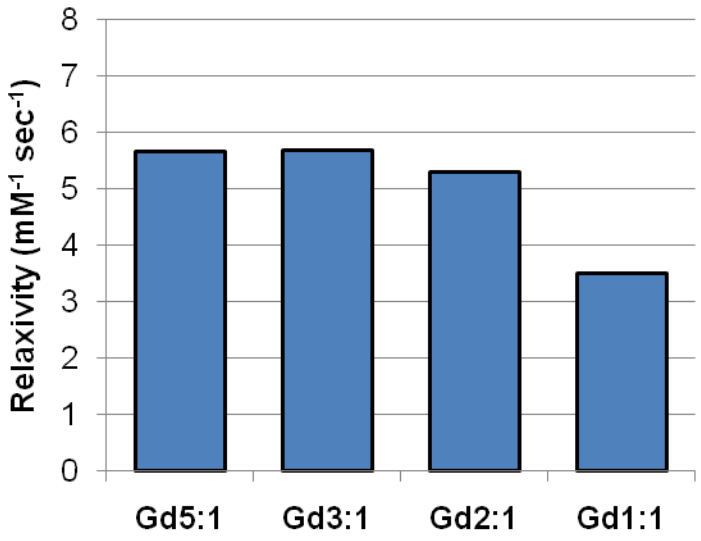

Figure 7-9. Relaxivity of free polymers in solution at 400 MHz.

Extensive studies are being carried out to understand the cellular uptake and trafficking pathways of these random copolymers using two-photon confocal microscopy. This work has been designed and carried out using these polymer systems by Patrick McLendon. The cells in the image below have been labeled with a cell wall stain (green) and the Eu-polymer sample is represented in the red channel. It is clear that **Eu3:1** polymer seems to accumulate in the perinuclear region. This staining is drastically different than that observed from the polymers in Chapter 6, indicating that galactose somehow plays a role in polyplex trafficking to the perinuclear region. There is no label in this case indicating the location of pDNA, so unfortunately, no conclusions can be made as to where theses polyplexes release their cargo. Ongoing microscopy studies across this entire series will help decipher exactly how these random copolymers increase transfection as a function of galactaramide content.

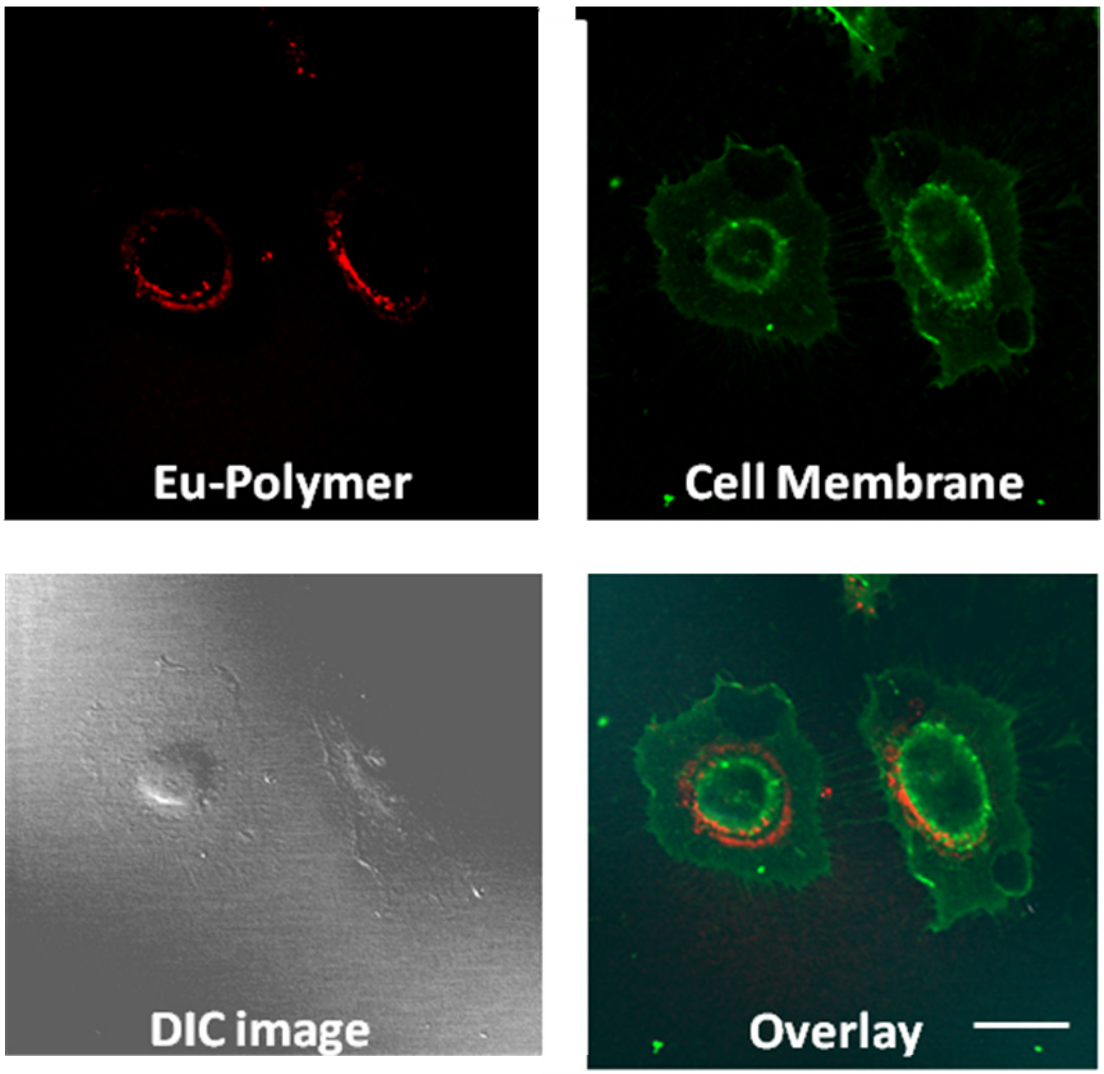

Figure 7-10. Eu(III) two photon excitation λ = 780 nm. Imaged 24 h after transfection. Scale bar equal to 20 mm.

7.5 Conclusions

This work demonstrates the development of an efficacious series of transfection reagents with high diagnostic potential. The polymers are likely degradable by the same route as their PGAA analogs, which could be a reason for the high transgene expression they promote. As well as great transgene expression, these polymers promote high cellular uptake, which is

important when the amount of cell loading is related to diagnostic response. Overall, these new polymers show excellent transgene expression, but are ultimately not well defined and degrade to quickly to consider a well characterized material.

7.6 Acknowledgement

The author would like to thank an excellent co-investigator, Patrick McLendon, for obtaining the cellular uptake data and for his efforts in monitoring these polymers with 2-photon confocal microscopy.

7.7 References

1. Bryson, J. M.; Fichter, K. M.; Chu, W. –J.; Lee, J. -H.; Li, J.; Madsen, L. A.; Reineke, J. M. *Proc. Nat. Acad. Sci. U. S. A.* **2009**, in revision.

2. Chapter 6 of this dissertation.

3. Liu, Y.; Reineke, T. M. *Bioconjugate Chem.* **2006**, *17*, 101-108.

4. Liu, Y.; Wenning, L.; Lynch, M.; Reineke, T. M. *J. Am. Chem. Soc.* **2004**, *126,* 7422 - 7423.

5. Srinivasachari, S; Fichter, K. M.; Reineke, T. M. *J. Am. Chem. Soc.* **2008**, *130*, 4618 - 4627.

6. Srinivasachari, S.; Liu, Y.; Zhang, G; Prevette, L.; Reineke, T. M. *J. Am. Chem. Soc.* **2006**, *128,* 8176 - 8184.

7. MacLaughlin, F. C.; Mumper, R. J.; Wang, J.; Tagliaferri, J. M.; Gill, I.;Hinchcliffe, M.; Rolland, A. P. *J. Controlled Release* **1998**, *56*, 259-272.

8. Erbacher, P.; Zou, S.; Bettinger, T.; Steffan, A. M.; Remy, J. S. *Pharm.Res.* **1998**, *15*, 1332-1339.

9. Prevette, L. E; Kodger, T. E; Reineke, L. M.; Lynch, M. L. *Langmuir*, **2007**, *23*, 9773 – 9784.

10. Prevette, L. E; Lynch, M. L.; Kizjakina, K.; Reineke, L. M. *Langmuir*, **2008**, *24*, 8090 – 8101.

11. Karmali, P. P.; Chaudhuri, A. *Med. Res. Rev.* **2007**, *27*, 696-722.

12. Kodama, K.; Katayama, Y.; Shoji, Y.; Nakashima, H. *Curr. Med. Chem.* **2006**, *13*, 2155-2161.

13. Kulkarni, R. P.; Wu, D. D.; Davis, M. E.; Fraser, S. E. *Proc Natl Acad Sci USA* **2005**, *102*, 7523-7528.

14. Bartlett, D. W.; Su, H.; Hildebrandt, I. J.; Weber, W. A.; Davis, M. E. *Proc. Natl. Acad. Sci. U. S. A.* **2007**, *104*, 15549-15554.

15. Pan, D. *et al. J. Am. Chem. Soc.* **2008**, *130*, 9186-9187.

16. McCarthy JR, Jaffer FA, Weissleder R (2006) A macrophage-targeted theranostic nanoparticle for biomedical applications. *Small* 2:983-987.

17. Resch-Genger, U.; Grabolle, M.; Cavaliere-Jaricot, S.; Nitschke, R.; Nann, T. *Nat Methods* **2008**, *5*, 763-775.

18. Liu, Y.; Reineke, T. M. *Manuscript in preparation*.

19. Prudêncio, M.; *et al. Chem. Eur. J.* **2004**, *10,* 3252 - 3260.

20. Liu, Y.; Reineke, T. M. *J. Am. Chem. Soc.* **2005**, *127*, 304 – 315.

Chapter 8: Suggested Future Work

8.1 Targeted inclusion studies with Gd10

Inclusion possibilities were the original impetus for synthesizing **Gd10** and offer unlimited potential for this easily functionalized contrast agent. Cyclodextrins are well known for their hydrophobic inclusion properties. Several delivery and imaging agents have utilized this property to attain organ targetable systems.[1] Much like the inclusion explored in Chapter 5, targeting agents such as folic acid (Figure 8-1),[2] could be conjugated to adamantane via a PEG connecting group, and included into the cyclodextrin cup of **Gd10**. Folate targeting is interesting because the folate receptor is over expressed in activated macrophage cells which are implicated in a variety of inflammatory diseases such as: arthritis, atherosclerosis, and Crohn's disease. Thus macrophage activity is directly related to inflammation and could be monitored via MRI. An inflammation marker which could serve as a disease predicting label would be a valuable diagnostic tool.

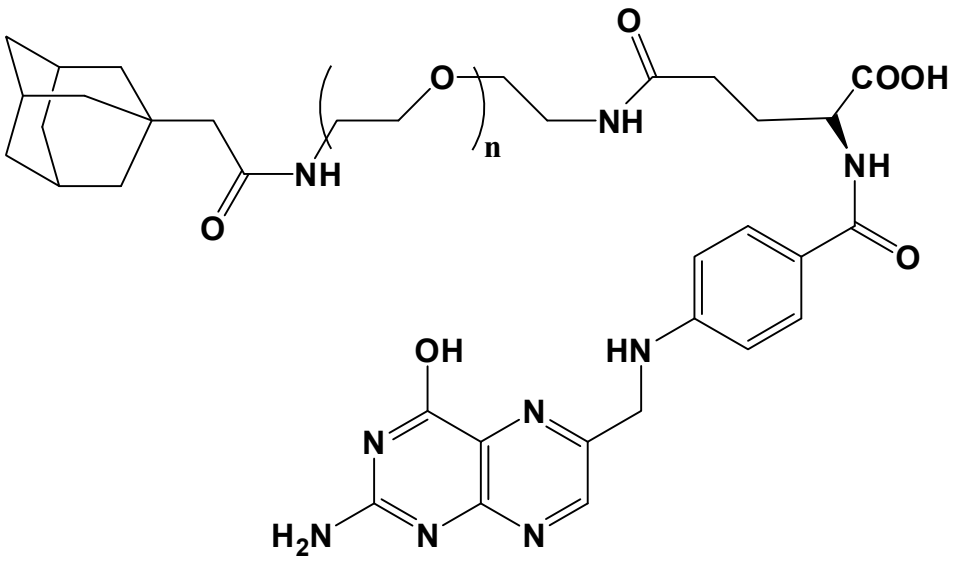

Figure 8-1. Adamantane-PEO-folic acid for conjugation to **Gd10** for selectively targeting active macrophage and endothelial cells.

8.2 New Inclusion Mediated Self-Assembly of Gd10

Only one hydrophobic inclusion moiety was explored with **Gd10** in Chapter 5. It is likely from the size of the aggregates that are formed that multi-lamellar structures could be forming. This type of assembly could occur because the inclusion molecule developed in Chapter 5 is not sterically bulky and can therefore bind several **Gd10** molecules at one time, essentially, non-covalently cross-linking them. Ideally, new hydrophobic tails could be designed that would include with **Gd10** that in only one way, preventing this cross-linking effect. This means the non-including hydrophobic tail of the guest molecule must be sterically bulky. Two suitable options to accomplish this (Figure 8-2) would be hydrophobic adamantane containing polymers, similar to those used by Jiang and coworkers.[3] These polymers contain pendant adamantyl groups conjugated to a hydrophobic backbone. Because the polymer consists

of a long chain with pendant groups, the only appropriate binding location is to the pendant adamantane groups because the backbone has no appropriate way to bind. This could be accomplished by forming a random *poly*-propylene with pentyladamantyl groups randomly incorporate within. To avoid the extra variables encountered by using polymers, adamantane conjugated to bulky rigid hydrophobic molecules such as pyrene or others could be a viable solution for more well characterized inclusion.[4] Pyrene would also add a second imaging modality (fluorescence) which would be interesting for multimodal imaging. Pyrene also shows different fluorescence whether it is in a hydrophilic or hydrophobic environment; a phenomenon that could be used to study ratios of complexed to un-complexed **Gd10**. Perhaps by eliminating multimeric binding of guest to host, new inclusion complexes might have properties similar to traditional surfactants and thus more predictable self-assembly behavior.

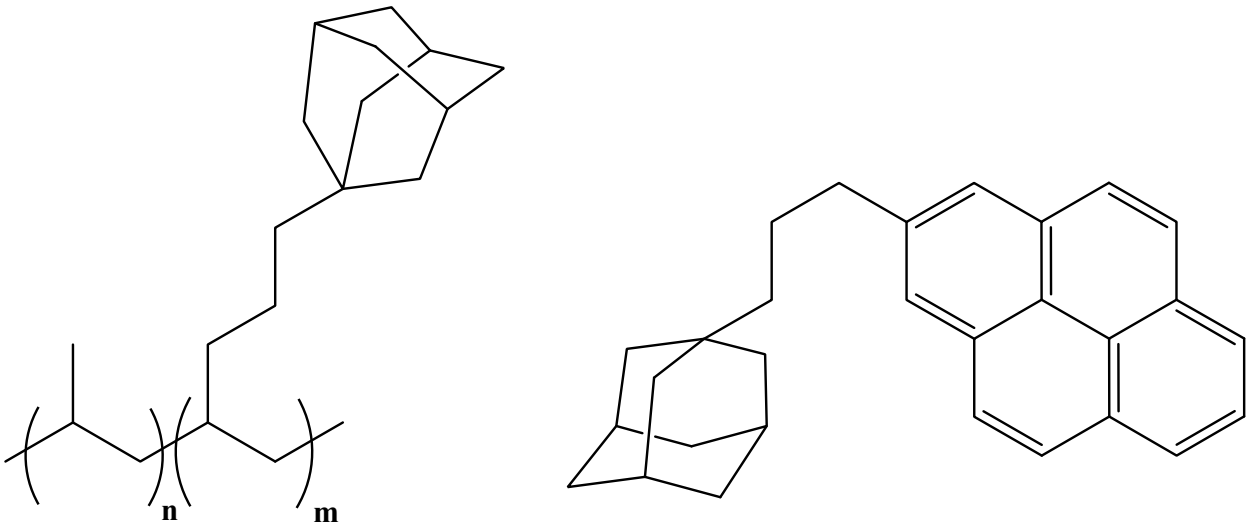

Figure 8-2. Proposed future synthesis: Inclusion molecules that have only one moiety for binding **Gd10.**

8.3 Intercalating Polymers as Sensors for Gene Release

Generation one (Chapter 6) and generation two (Chapter 7) of the Ln-containing nucleic acid delivery polymers were breakthroughs in diagnostic drug delivery, though their signal is related to their location and not an event (such as nucleic acid release). Newer generation polymers could utilize energy transfer from an antenna to sense an event such as gene release. Ideally the antenna would be a group that can not only harvest ultraviolet light and transfer the energy to the Eu(III) center, but also a group that can intercalate double stranded DNA and be deactivated because of the hypochromic effect (see Figure 8-3). Napthyl-amido groups were conjugated to diethylenetriaminetetraacetic acid to incorporate into an oligoamine polymer for this purpose. A napthyl-amido antenna group has a less than desirable emission band for Eu(III) excitation though. An ideal group for this is the coumarin II ligand, which absorbs at 360 nm, emits at 405 nm, intercalates DNA, and efficiently transfers energy to Eu(III). Similar systems have shown promise as double stranded DNA sensors which have been developed by David Parker and coworkers at The University of Durham.[5] A synthetic plan was developed and attempted according to Scheme 8-1.

Scheme 8-1. Proposed, partially completed synthesis of intercalating Eu(III) polymer.

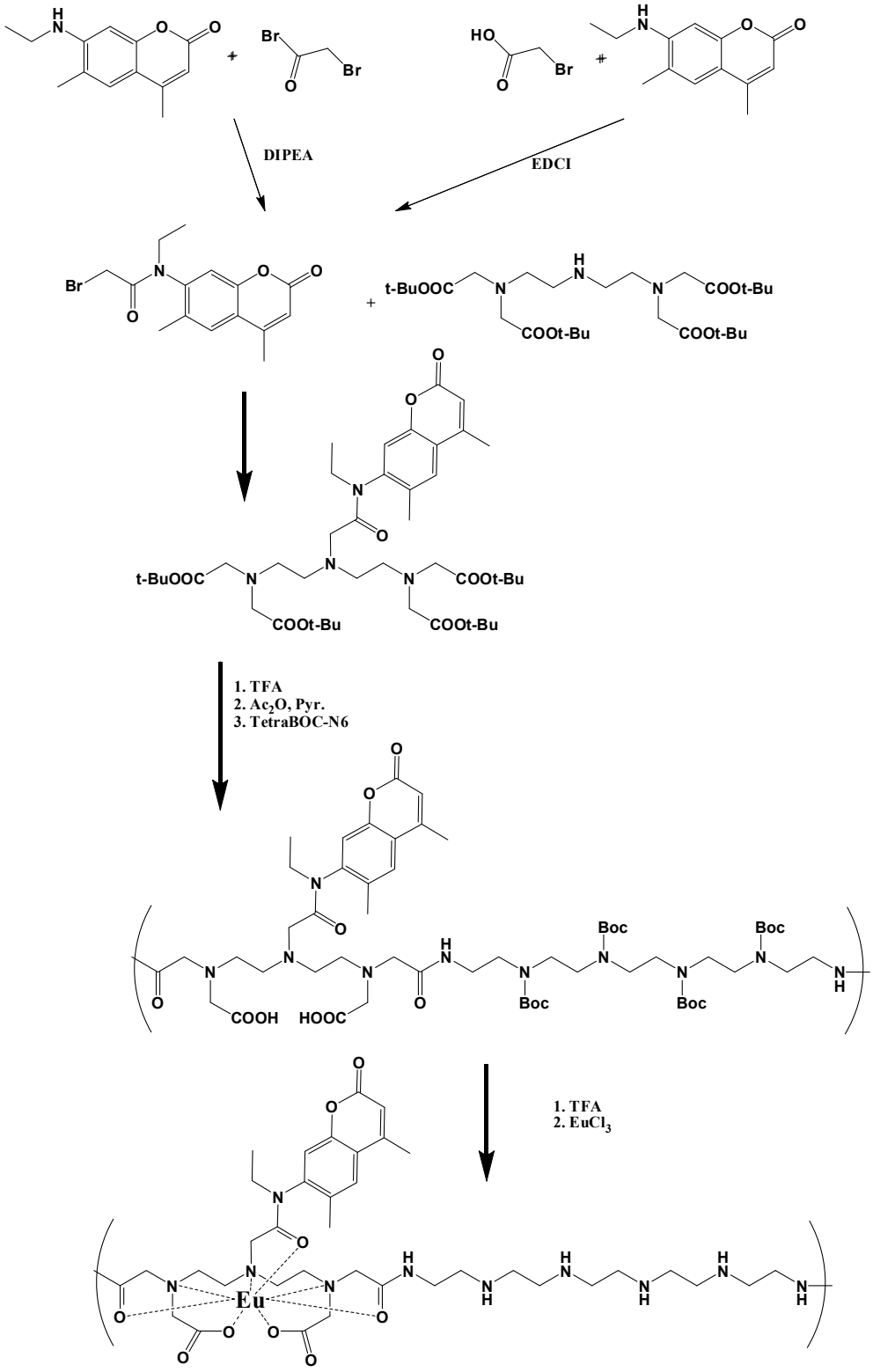

Conjugation of coumarin II to an electrophilic group such as bromoacetate was accomplished via two separate amide bond forming routes (Scheme 8-1): secondary amine reaction with bromoacetyl bromide and secondary mine reaction with EDCl activated bromoacetic acid. The later route here creates fewer byproducts and doesn't require workup on a silica column, making this the preferable route. Conjugation of bromoactetylcoumarin II to DTTA is accomplished at RT in DMF. The NMR shows successful coupling has occurred, but purification is required to remove excess starting material. Unfortunately, it seems, that coumarin II is hydrolyzed off of the DTTA molecule through its amide bond (making DTPA and coumarin II) during this column purification step. Perhaps a better workup or synthetic modification at this step would allow Scheme 8-1 to proceed.

It is not well understood how and when non-viral gene delivery agents release their cargo in cells. Answering this question using a clever system would likely be high impact work. This proposed system could become a very useful tool for visualizing DNA release in cells. Synthesizing these types of systems has been initiated in my research and will hopefully continue to completion in the hands of newer investigators in the Reineke group.

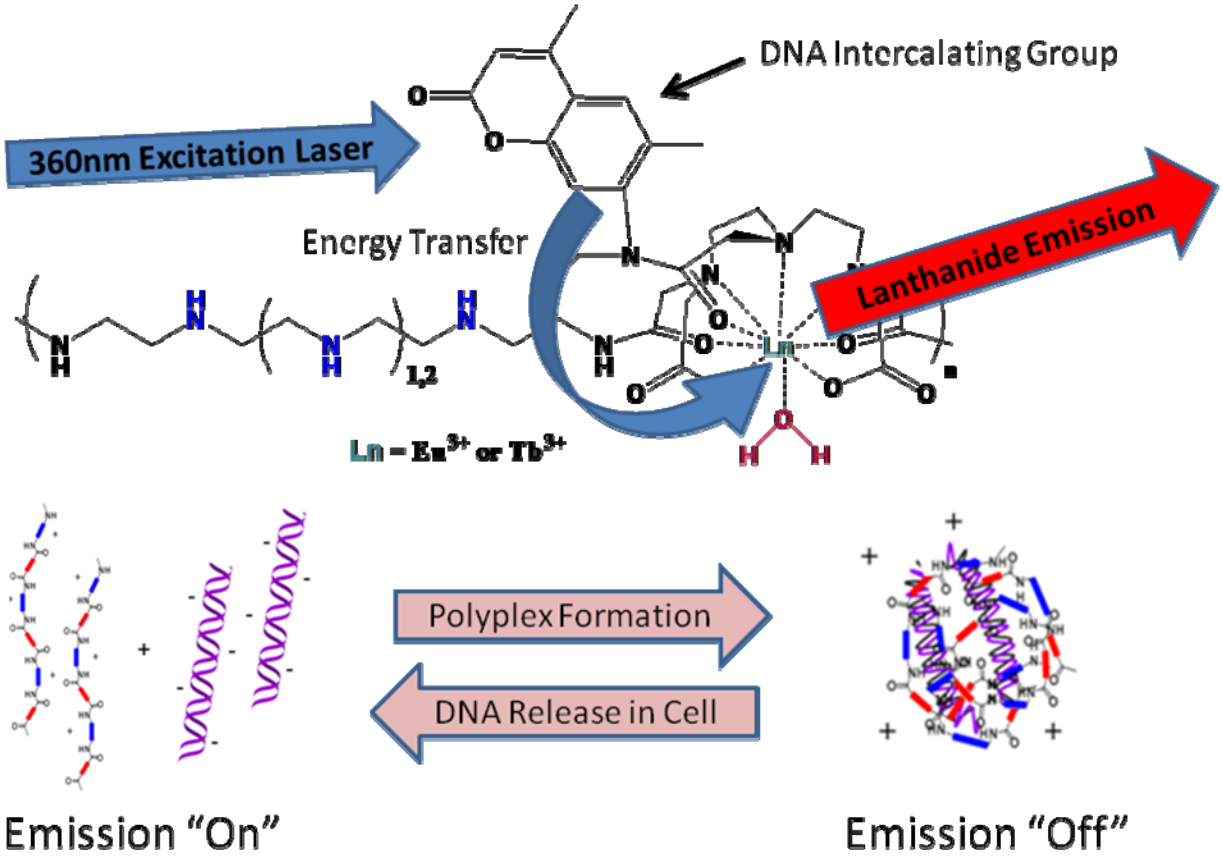

Figure 8-3. Proposed structure of intercalating Eu(III) containing polymers as sensors for gene release. When coumarin 2 "antenna" group is intercalated, no energy transfer can occur and the emission form Eu(III) is essentially turned off. Upon DNA release, this group is no longer intercalated and therefore will facilitate Eu(III) emission.

8.4 Other Ln-Containing *poly*-glycoamidoamines and *in vivo* studies

To this point, only galactaramideoligoamine-containing Ln(III) polymers have been synthesized in four ratios, however the likely hood that our desired structure carries through the final step of synthesis before degrading is unlikely. A new synthetic method is required to arrive at these final desired structures. This new method will require the elimination of aqueous

dialysis steps in favor of less degrading purification steps. One possible solution would be to do the purification of these polymers using a size exclusion gel such as sephadex-25 or a quick purification step such as centrifugal dialysis. Another viable option would be to use carbohydrates with less labile bonds than α-hydroxylamides. Connection methodologies such as thoughs utilized in the synthesis of Trehalose click polymers might be better suited here. [6]

The trend we observed indicated that as more carbohydrate was integrated into the polymer backbone, higher transfection efficiency occurred, however these results are somewhat questionable in light of the errant elemental analysis data. If this trend holds true, it could certainly be extended with even higher galacteramide ratios. Since well defined structures are more likely to have clinical use, it would be of interest to make derivatives of these preliminary structures with more controlled architectures such as AB-copolymers. Other logical future structures would include other carbohydrates, especially carbohydrates that can promote polyplex serum stability such as trehalose. This project offers a preliminary look at what is possible with Ln-containing *poly*-glycoamidoamines and future work will certainly uncover more exciting properties and uses for these vectors.

All of the Ln-containing polymers discussed in this dissertation have shown interesting diagnostic and delivery properties *in vitro*, but to this point have not been evaluated *in vivo*. Nucleic acid delivery has been studied *in vivo* with a multitude of cationic macromolecule systems. Until now, researchers have had little success monitoring these delivery processes with MRI, especially with fine resolution that the Gd(III) polymers of Chapter 6 have attained in *in vitro* demonstrations. One very important question in this field right now is: how do these polymer-DNA nanoparticles diffuse into tissue? This question has been answered to a degree with labeled DNA, but the location of the associated polymer is not clear and cannot be assumed

to be associated with the DNA staining. Another important question is: how, where, and when, are these polymers/polyplexes washed out or metabolized? The Gd(III) chelating polymers might be able to answer these questions based on their spatial MRI profiles over time. One important feature of macromolecular contrast agents is their ability to be retained in tumors. Future work could certainly deliver nucleic acids into tumors and perhaps monitor tumor size fluctuations as a metric for therapeutic efficacy. These type of applications ambody the exact purpose of a theranostic agent. These polymers have the aptitude to address these questions and further diagnostic, pharmokinetic, and excretion, related *in vivo* questions, in the future.

8.5 References

1. Davis, M. E.; Brewster, M. E. *Nature Rev. Drug Discovery* **2004**, *3*, 1023 – 1035.

2. Hilgenbrink, A. R.; Low, P. S. *J. Pharm. Sci.* **2005**, *94*, 2135 – 2146.

3. Wang, J.; Jiang, M. *J. Am. Chem. Soc.* **2006**, *128*, 3703 – 3708.

4. Wu, A.; Shen, X.; He, Y. *J. Colloid and Interface Sci.* **2006**, *302*, 87 – 94.

5. Montgomery, C. P.; Murray, B. S.; New, E. J.; Pal, R.; Parker, D. *Acc. of Chem. Res.* **2009**, *ASAP*.

6. Srinivasachari, S.; Liu, Y.; Zhang, G; Prevette, L.; Reineke, T. M. *J. Am. Chem. Soc.* **2006**, *128,* 8176-8184.

Appendix A. Important NMR and Mass Spectra

Figure A-1: Proton NMR Spectrum of compound 2, Chapter 3.

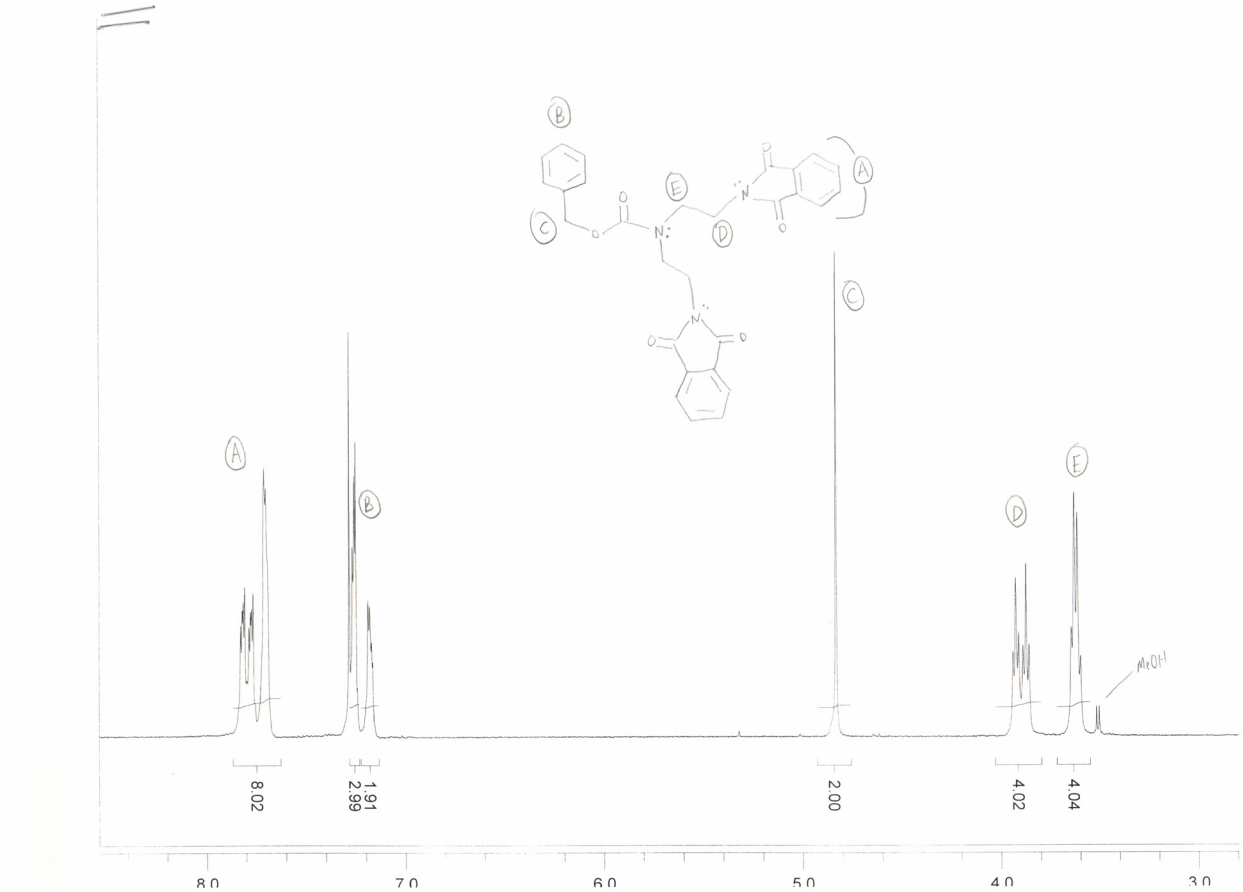

Figure A-2: ESI-MS Spectrum of compound 2, Chapter 3.

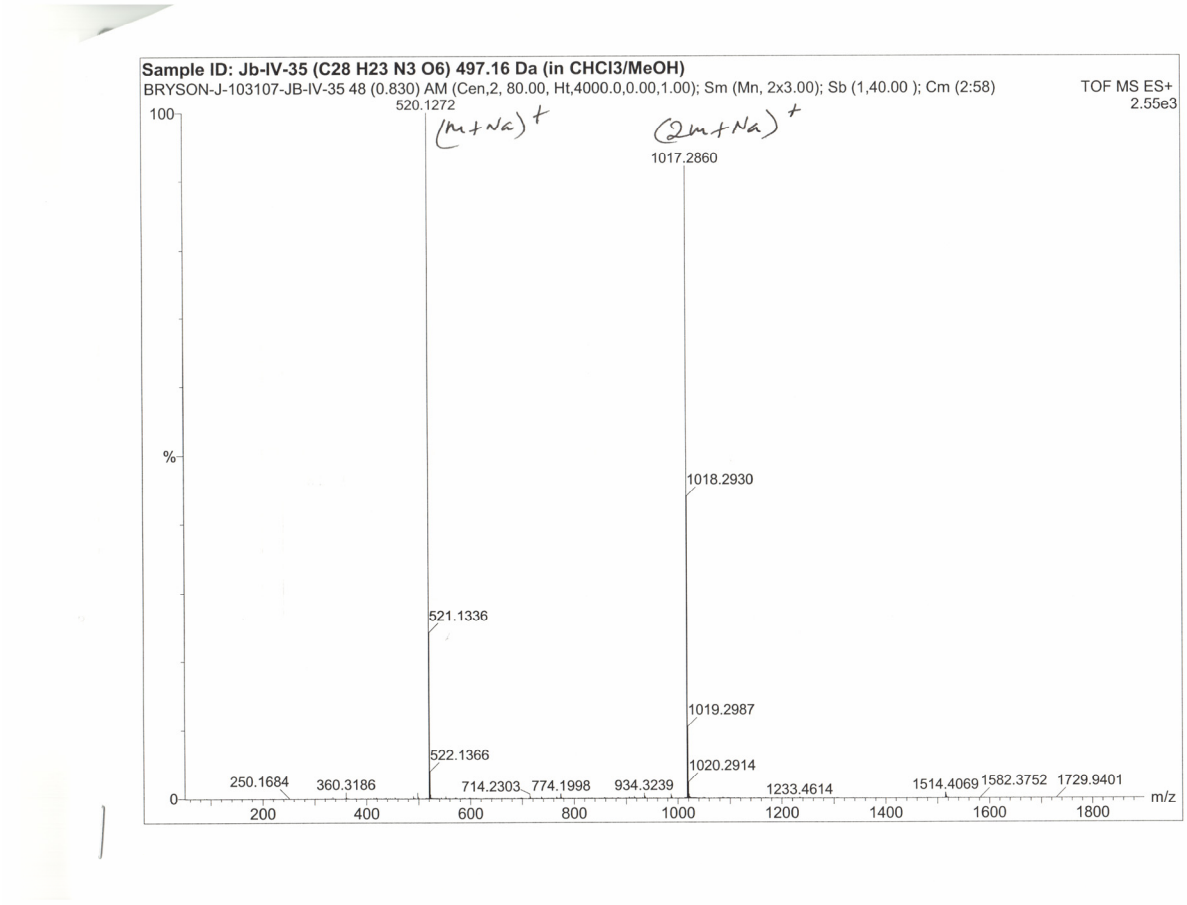

Figure A-3: Proton NMR Spectrum of compound 3, Chapter 3.

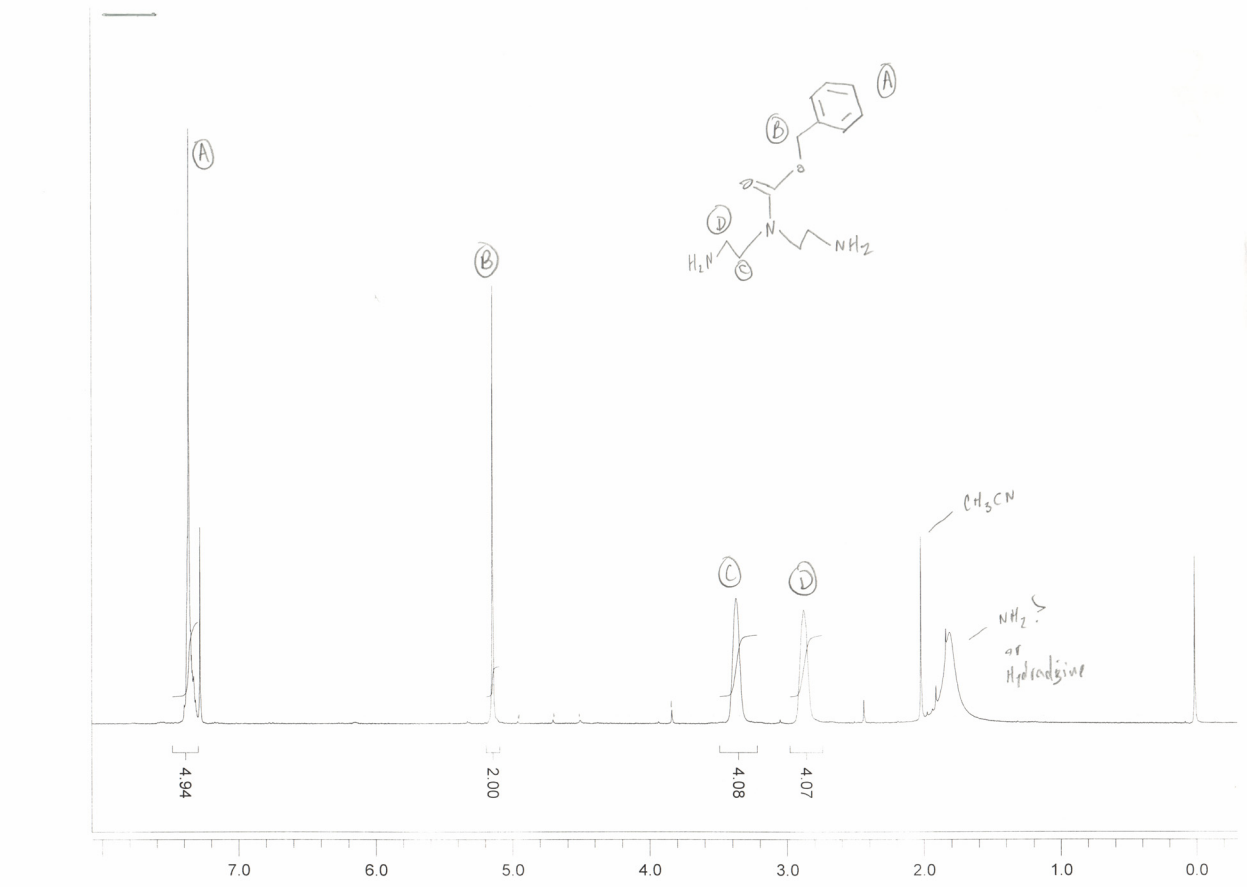

Figure A-4: Proton NMR Spectrum of compound 4, Chapter 3.

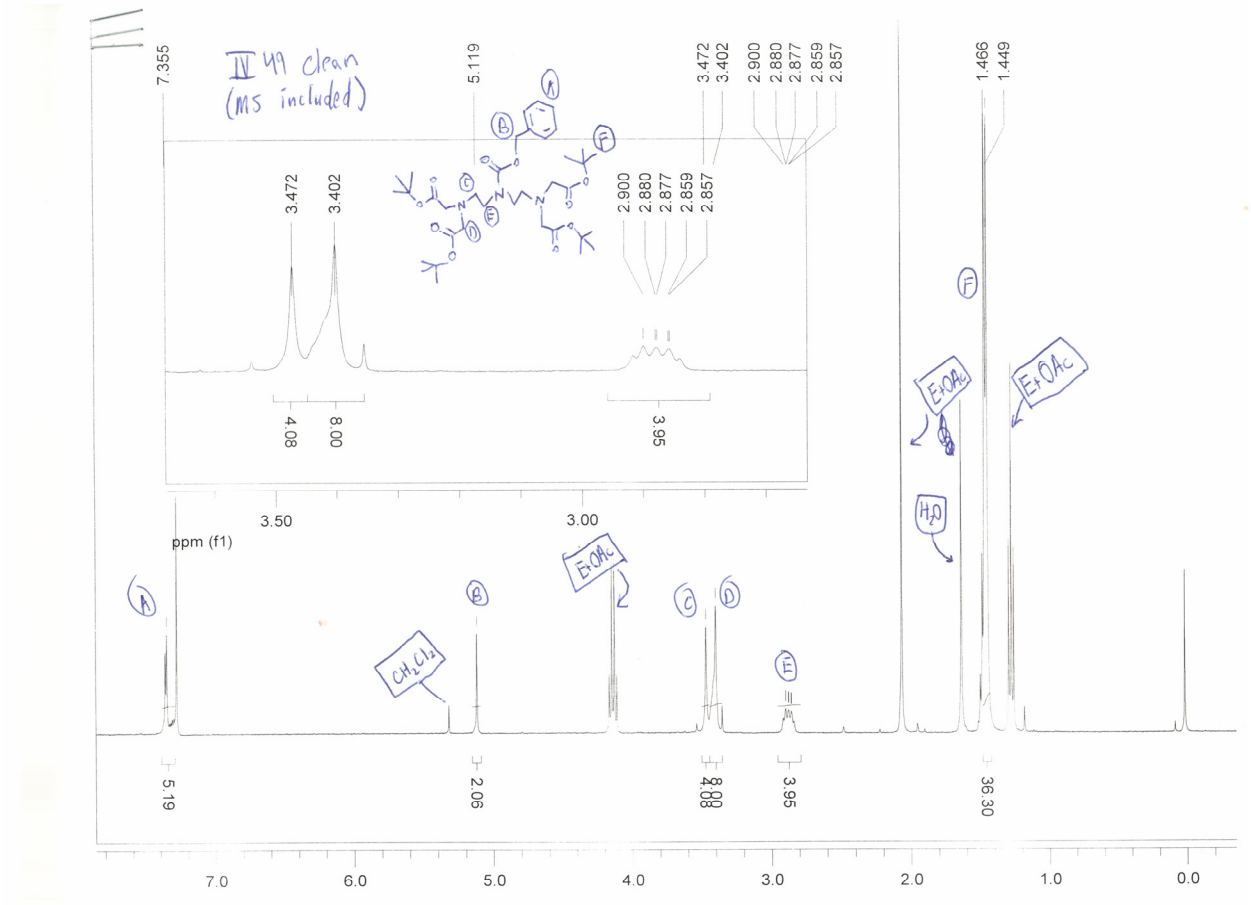

Figure A-5: ESI-MS Spectrum of compound 4, Chapter 3.

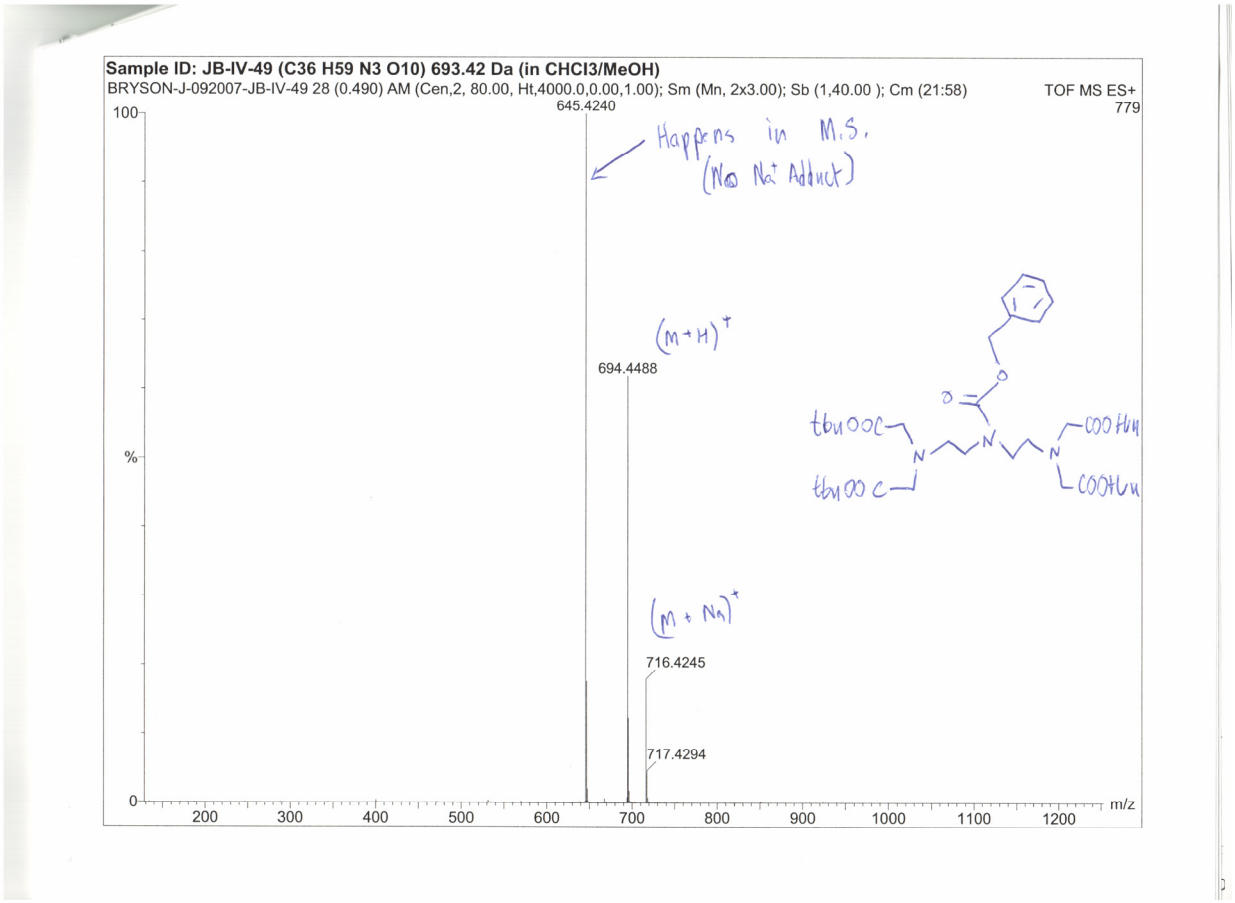

Figure A-6: Proton NMR Spectrum of compound 5, Chapter 3.

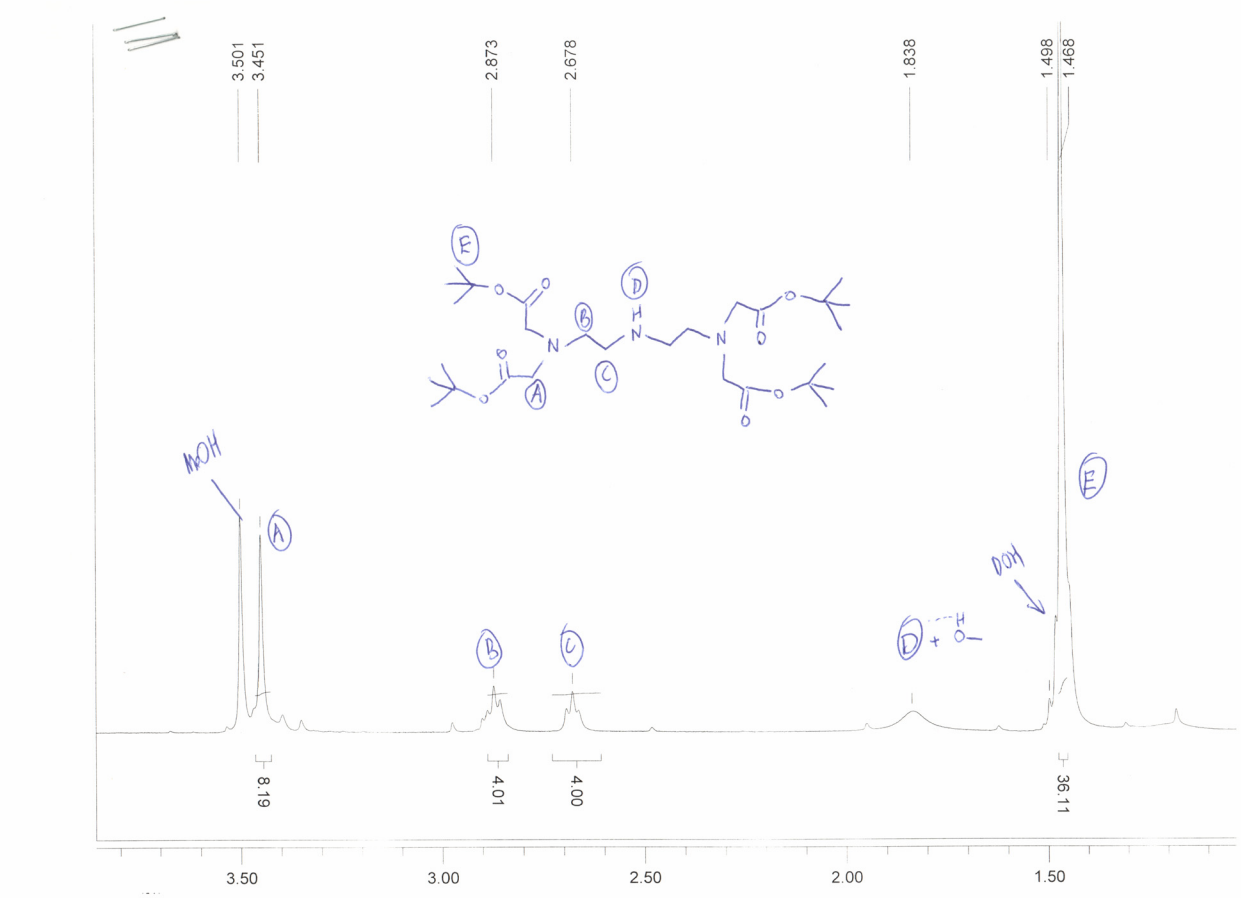

Figure A-7: ESI-MS Spectrum of compound 5, Chapter 3.

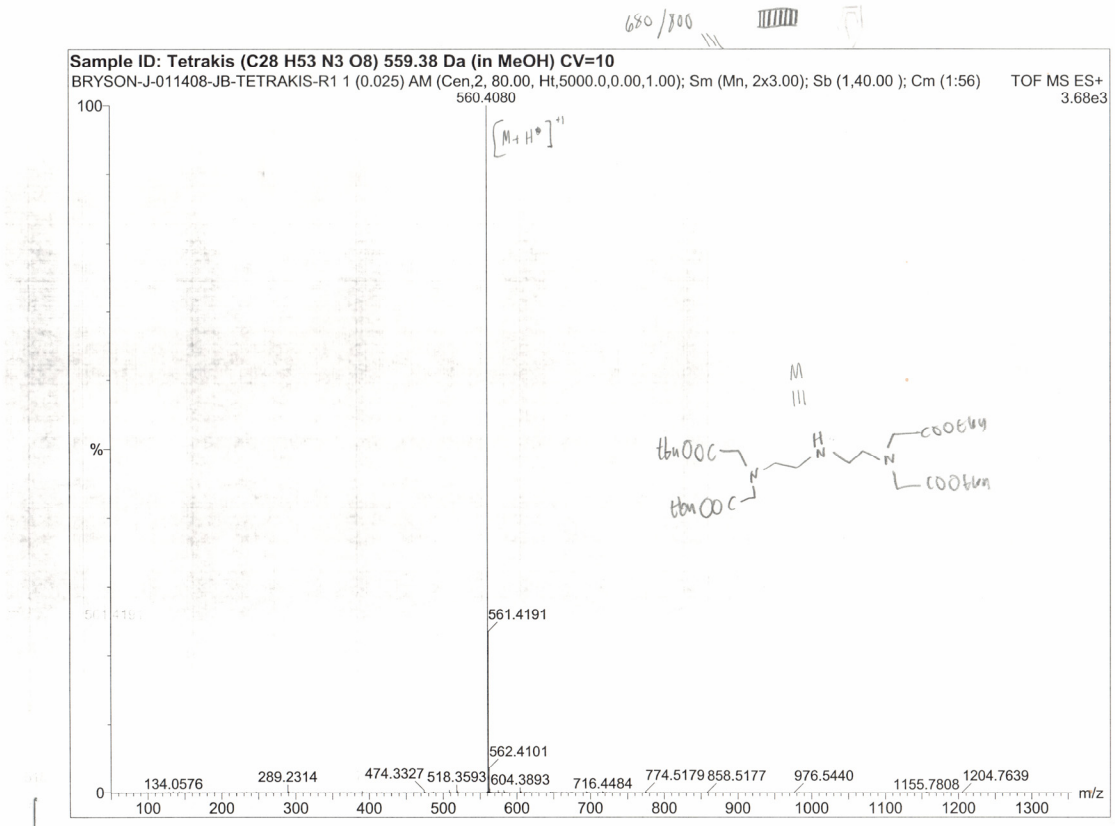

Figure A-8: NMR Spectrum of compound 6, Chapter 3.

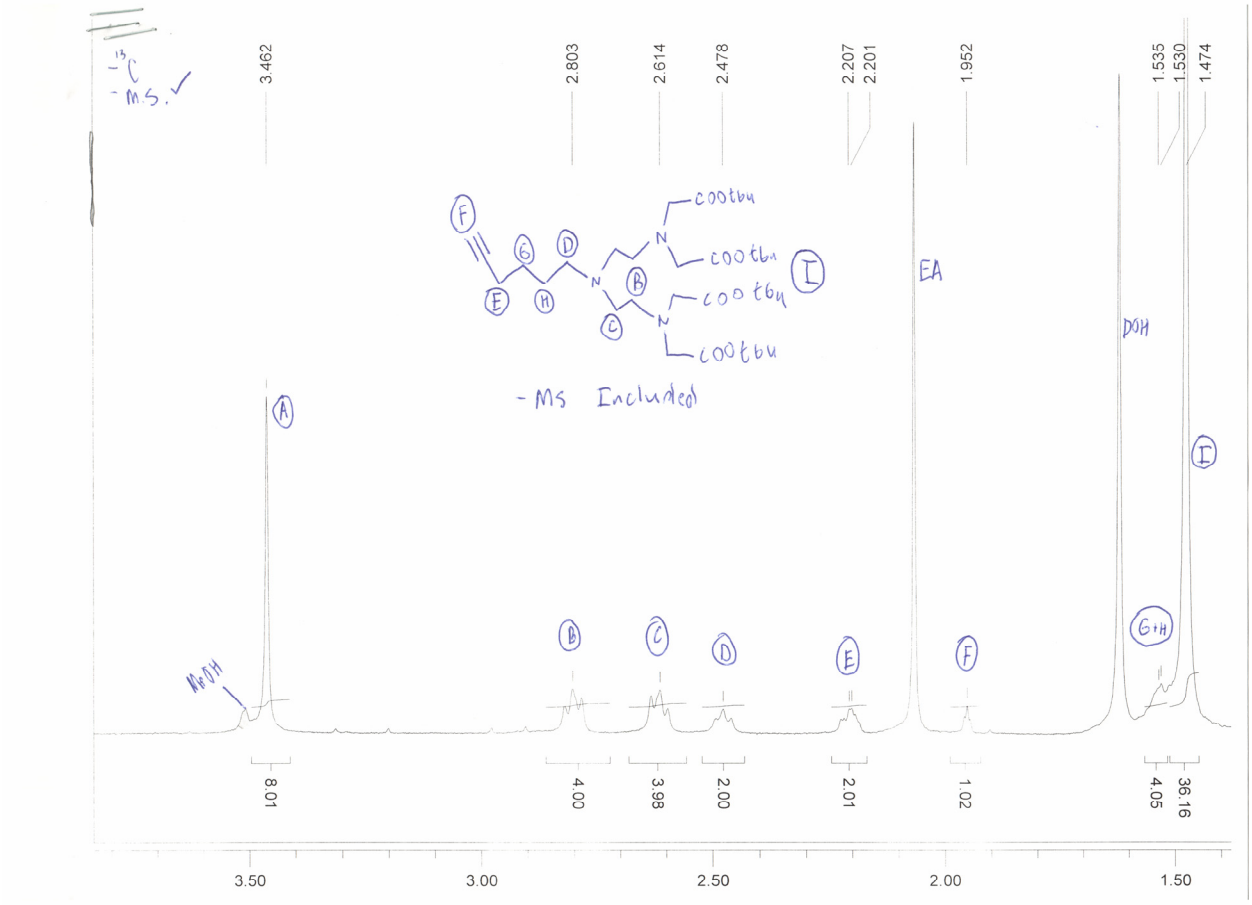

Figure A-9: ESI-MS Spectrum of compound 6, Chapter 3.

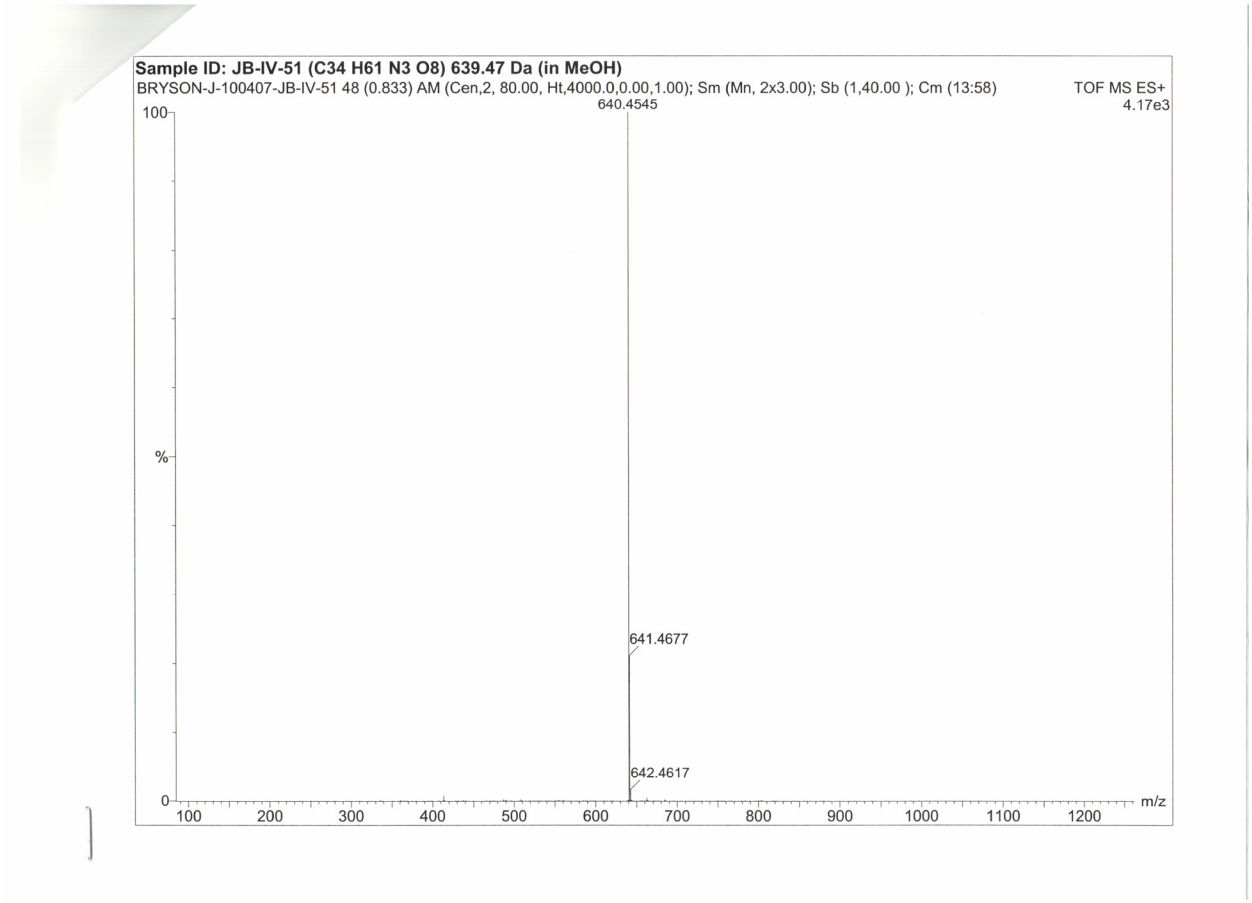

Figure A-10: NMR Spectrum of compound 8, Chapter 3. ESI-MS of this compound is found in Chapter 3.

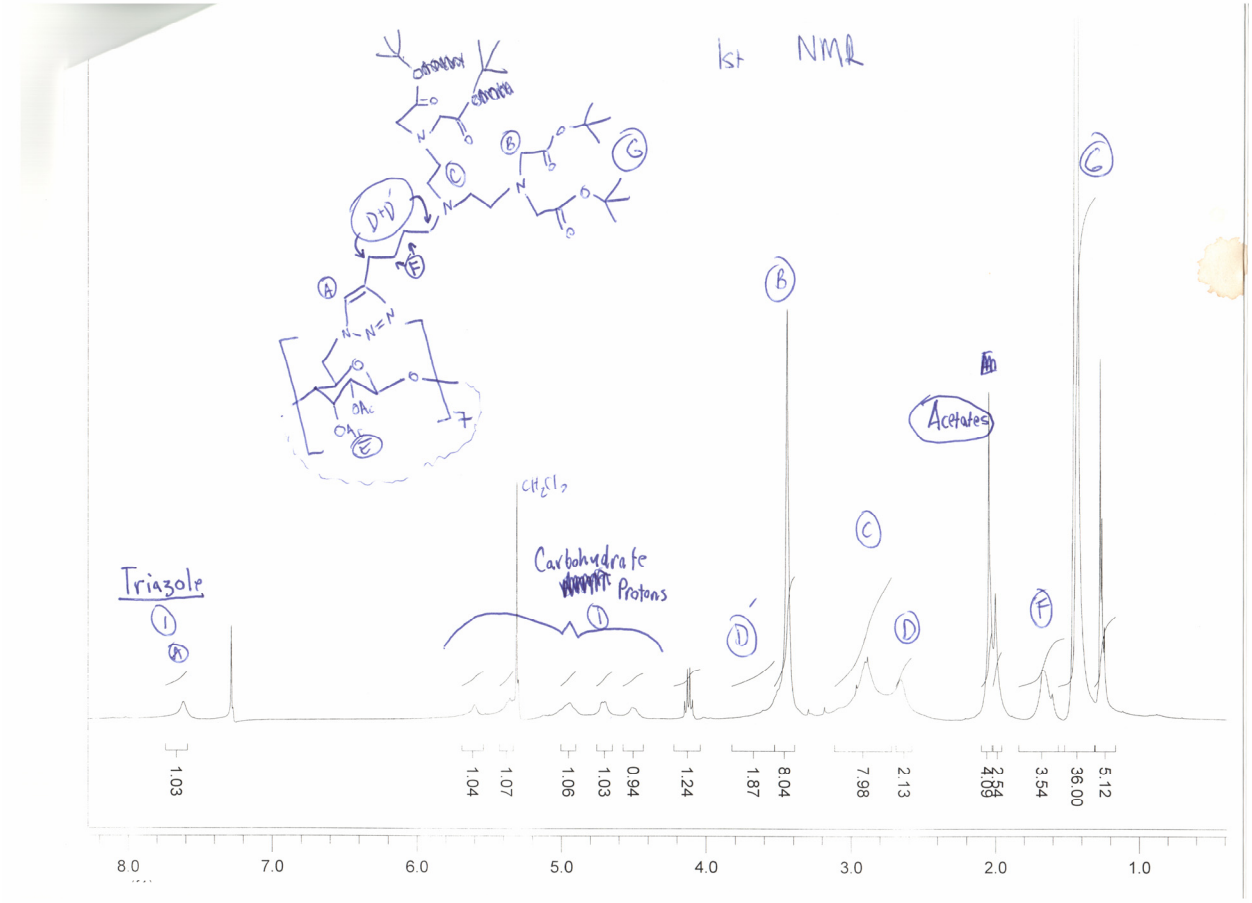

Figure A-11: NMR Spectrum showing the shift between starting material adamantyl acetic acid and adamantyl acetyl chloride, compound 1, Chapter 5.

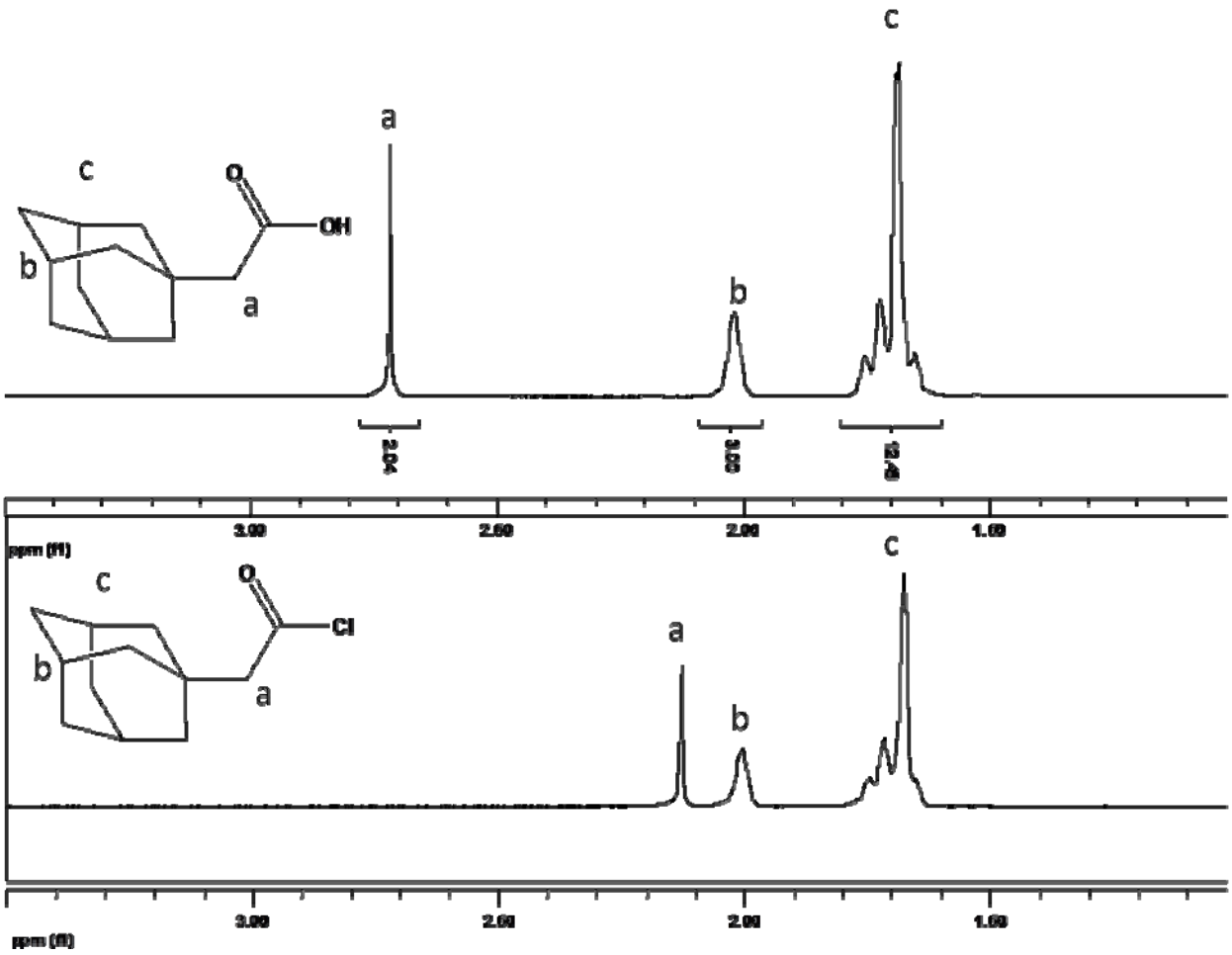

Figure A-12: NMR Spectrum showing compound 2, Chapter 5.

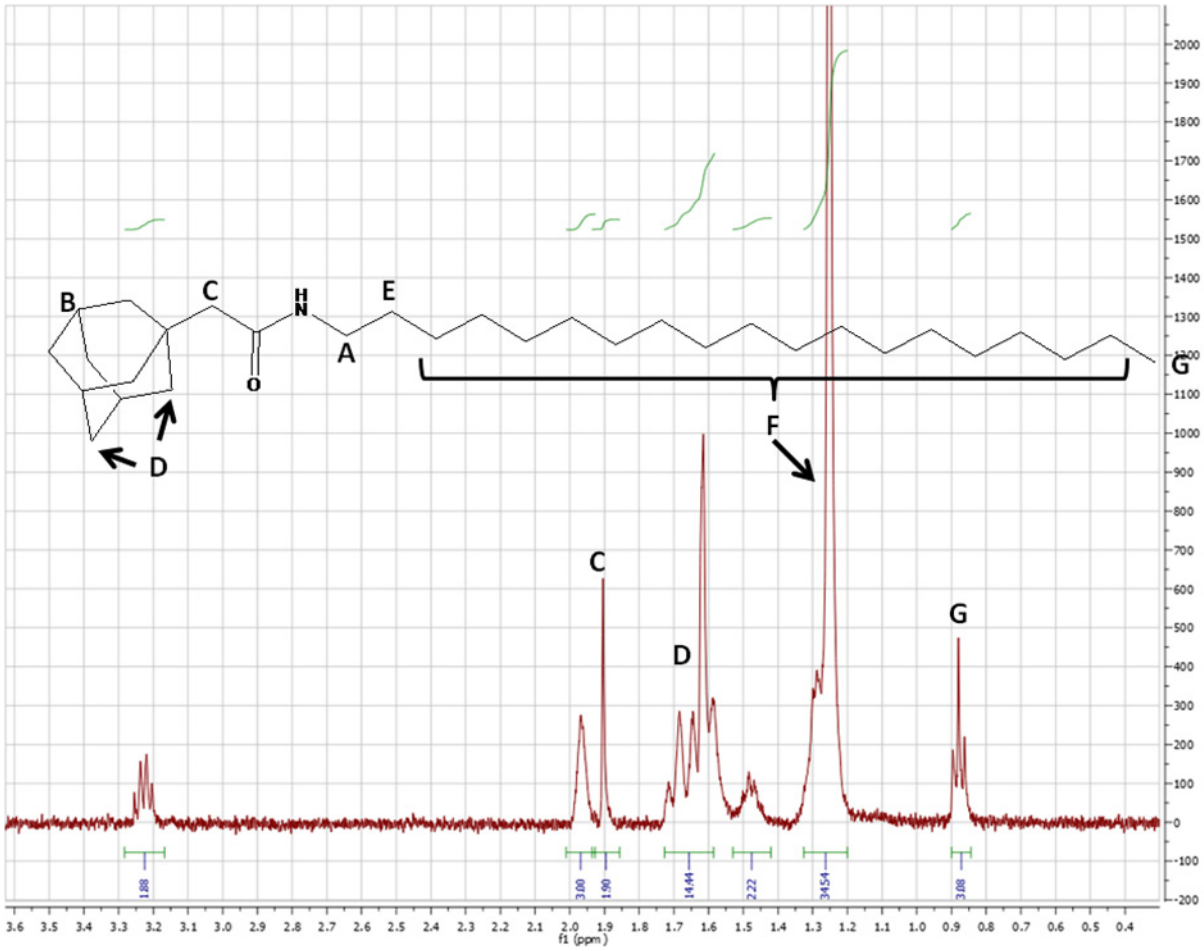

Figure A-12: ESI-MS Spectrum showing compound 2, Chapter 5.

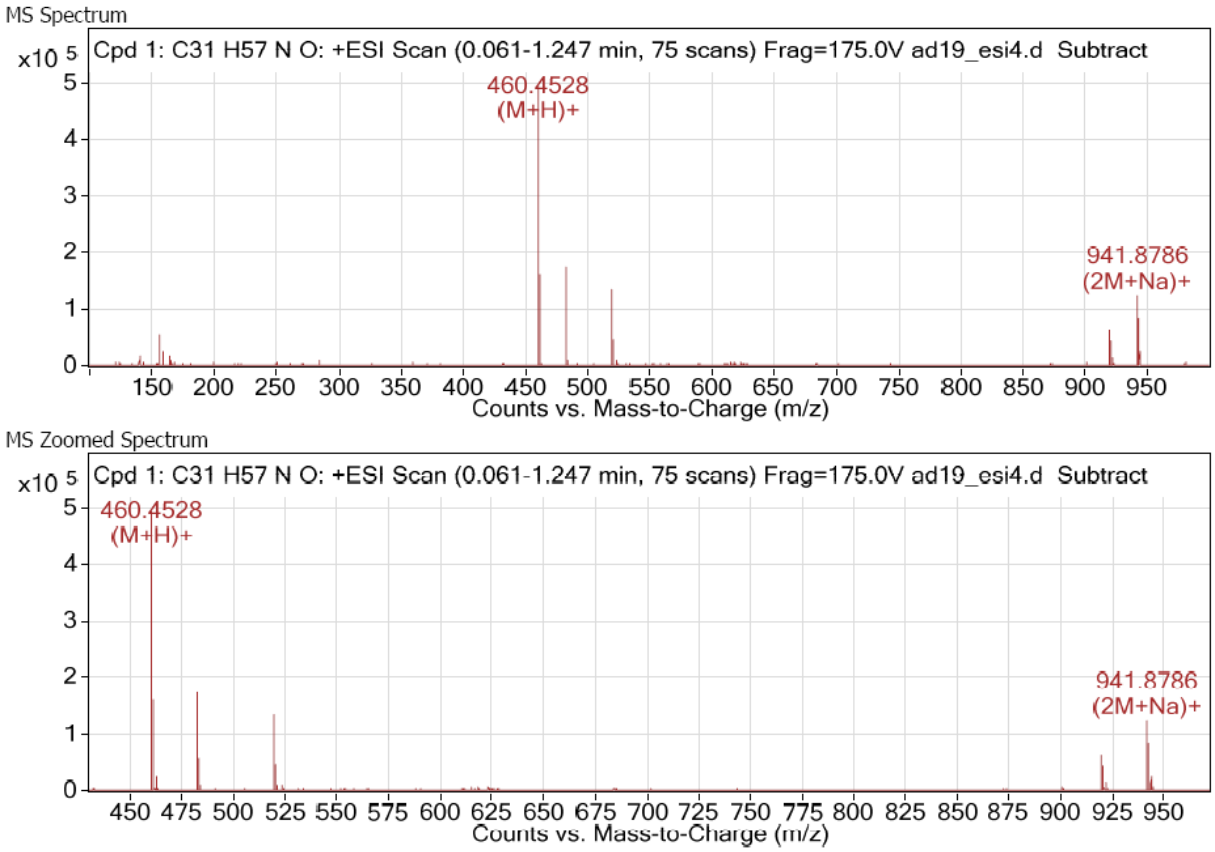

Appendix B: Dynamic Light Scattering Measurements for **Gd10** and pDNA

Figure B-1. Size intensity by volume of **Gd10** reported in Chapters 3 – 5, in phosphate buffered saline. The average hydrodynamic radius of **Gd10** was 5.52 nm.

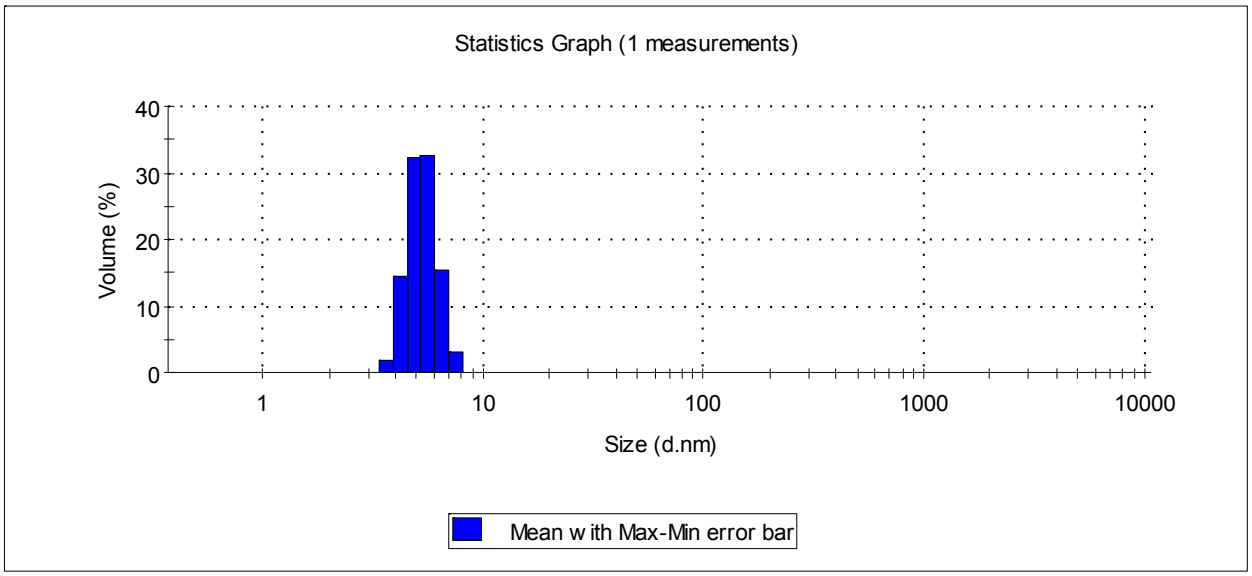

Figure B-2. Size distribution by volume for pDNA used for studies in chapters 6 and 7. Hydrodynamic radius was found to be 102 nm.